University of South Florida
Scholar Commons

Graduate Theses and Dissertations

Graduate School

1-1-2015

RF MEMS Resonators for Mass Sensing Applications

Ivan Fernando Rivera
University of South Florida, ifrivera@mail.usf.edu

Follow this and additional works at: http://scholarcommons.usf.edu/etd

Part of the Electrical and Computer Engineering Commons

Scholar Commons Citation
Rivera, Ivan Fernando, "RF MEMS Resonators for Mass Sensing Applications" (2015). *Graduate Theses and Dissertations.*
http://scholarcommons.usf.edu/etd/5817

This Dissertation is brought to you for free and open access by the Graduate School at Scholar Commons. It has been accepted for inclusion in Graduate Theses and Dissertations by an authorized administrator of Scholar Commons. For more information, please contact scholarcommons@usf.edu.

www.manaraa.com

RF MEMS Resonators for Mass Sensing Applications

by

Ivan Fernando Rivera

A dissertation submitted in partial fulfillment
of the requirements for the degree of
Doctor of Philosophy in Electrical Engineering
Department of Electrical Engineering
College of Engineering
University of South Florida

Major Professor: Jing Wang, Ph.D.
Thomas Weller, Ph.D.
Arash Takshi, Ph.D.
Rasim Guldiken, Ph.D.
Shengqian Ma, Ph.D.

Date of Approval:
February 4, 2015

Keywords: Motional Resistance, ALD,
Capacitive, Piezoelectric, Sensitivity, Gas Detection

Copyright © 2015, Ivan Fernando Rivera

www.manaraa.com

DEDICATION

To my mother Ana Flor Sanchez, my father Ivan Rivera, my brother Sebastian Rivera,

my wife Mian Wei and my son Alejandro Rivera

www.manaraa.com

ACKNOWLEDGMENTS

First and foremost I would like to express my deepest gratitude to my advisor Prof. Jing Wang for believing in me and helping me believe in myself. His guidance and dedication helped me overcome all the difficult choices that I faced through my challenging grad school career. I also would like to extend my appreciation to the rest of my dissertation committee: Prof. Thomas Weller, Prof. Shengqian Ma, Prof. Rasim Guldiken, and Prof. Arash Takshi, for their encouragement, suggestions, and support.

My sincere thanks also goes to all the Nanotechnology Research and Education Center (NREC) staff members: Kevin Scott, Abhishek Day, Michaela Miller, Sclafani Louis-Jeune, Robert Tufts, Dr. Yusuf Emirov, Jay Bieber and Richard Everly for their outstanding work keeping every piece of equipment running in top condition. My special thanks goes to Rich Everly, cleanroom engineer, for all his enormous and countless help while I was micro-fabricating my devices.

I also would like to thank all of my friends including all the past and current RF MEMS Transducers Group members for all their unlimited support, help and guidance. Special thanks go to my close friends: Matthew Chrzanowski, Juan Castro, Di Lan, Denise Lugo, Timothy Palomo, Ramiro Ramirez, Patrick Nesbitt, Abhishek Day, Adrian Avila, Maria Cordoba, Eduardo Rojas, Mohamed Abdin, Surya Cheemalapati, Jose Carballo, Qi Ni, and many more, for their limitless friendship and support when I needed the most.

I'm in eternal debt with my parents because I owe them who I am. They guided through my first steps of life, they held my hand through the rough times, and they provided me something

المنارة للاستشارات

www.manaraa.com

that no one else can, unconditional love no matter what. I'm also in great debt with little brother, Sebastian Rivera, a future tennis star, because he always looked up to me and that gave me the strength to become an exemplary role model.

My deepest appreciation goes to Dr. Mian Wei a.k.a. "my wife", for providing me the greatest gift any one can ever wish for, Alejandro W. Rivera, my son. My wife and my son are the source of motivation that keeps refueling my aspiration every day to be the best that I can possibly be.

المنارة للاستشارات
www.manaraa.com

TABLE OF CONTENTS

LIST OF TABLES iii

LIST OF FIGURES iv

ABSTRACT xi

CHAPTER 1 INTRODUCTION 1
1.1 MEMS Sensor 2
1.2 Resonant MEMS Mass Sensors 4
1.3 CMOS-MEMS Integration 5
1.4 Previous Work on Resonant Mass Sensors 7

CHAPTER 2 BACKGROUND AND THEORY 13
2.1 Thin-film Piezoelectrically Transduced Resonators 13
2.2 Piezoelectricity Effect 14
2.3 Piezoelectric Materials for MEMS Applications 16
2.4 Mathematical Modeling of Piezoelectricity 18
2.5 TPoS Resonators 20
2.6 Capacitively-Transduced Resonators 21
2.7 Capacitance of Parallel Plates 22
2.8 Resonant Mode Shapes 24
2.9 RF MEMS Resonator Equivalent Circuit Model 27
2.10 Sensitivity and Limit of Detection (LOD) of RF MEMS Resonators 31

CHAPTER 3 CAPACITIVE RF MEMS RESONATORS 32
3.1 Resonant Frequency and Mode Shape Selection 33
3.2 Oxidation Air-gap Reduction Fabrication Process 35
3.3 DRIE Characterization 38
3.4 Thin Sacrificial Layer Air-gap Reduction Fabrication Process 44
3.5 RF Test Results 48

CHAPTER 4 PIEZOELECTRIC RF MEMS RESONATORS 51
4.1 Resonant Frequency and Mode Shape Selection 52
4.2 Piezoelectrically-transduced Resonator Fabrication Process 53
4.3 Lift-off Characterization 55
4.4 ZnO Magnetron Deposition Characterization 57
4.5 Release Process for Piezoelectrically-transduced Resonators 58
4.6 On-wafer Probing 2-port Set-up 62

المنارة للاستشارات
www.manaraa.com

4.7 Thin-film ZnO Resonators ... 64
4.8 Thin-film ZnO-on-Si Resonators ... 66
4.9 TSV Thin-film ZnO-on-Si Resonators ... 67
4.10 Pre-released Thin-film ZnO-on-Polysilicon Resonators ... 79
4.11 TPoSCRE Released Thin-film ZnO-on-Si Resonators ... 82

CHAPTER 5 MASS SENSOR DEVELOPMENT ... 84
5.1 Wire-bonding of ZnO-on-Si Resonator for Vacuum Testing ... 84
5.2 Theoretical Sensitivity and LOD Determination ... 86
5.3 FIB Platinum Deposition Characterization ... 88
5.4 Maximal and Minimal Displacement Area Versus Sensitivity Analysis ... 89
5.5 MOF Functionalized Mass Sensors ... 92

CHAPTER 6 CONCLUSION AND FUTURE WORK ... 99
6.1 Contributions of this Work ... 99
6.2 Future Work ... 102
6.2.1 Ultra-Sensitive Gas Sensor Concept ... 102
6.2.2 Ultra-Sensitive Gas Sensor Test-set up Concept ... 103

REFERENCES ... 104

APPENDIX A ... 110
A.1 Key Fabrication Process Steps ... 110

ABOUT THE AUTHOR ... End Page

www.manaraa.com

LIST OF TABLES

Table 1.1 Fundamental Physical Quantities.. 3

Table 1.2 Performance Comparison of Several State-of-the-art Sensing Technologies 12

Table 2.1 Properties of the Most Widely Used Piezoelectric Ceramics [31, 33] 17

Table 2.2 Second Order Material Coefficients [32]... 19

Table 2.3 Electromechanical Analogy between Electrical and Mechanical Parameters 28

Table 3.1 Standard Bosch High-aspect Silicon Dry Etching Recipe used for Alcatel AMS 100 Inductively Couples Plasma (ICP) Systems. 40

Table 4.1 1st Contour Mode 88 µm-radius ZnO-on-Si Disk Design vs. Spurious Responses.. 69

Table 4.2 Frequency Responses of a 96µm-wide Rectangular Plate Resonator Operating in N3 96 Extensional Mode with Different W/L Ratios. 75

Table 4.3 Frequency Responses of a 150 µm-length Extensional Square Plate Resonator Designs.. 78

Table 4.4 Device Structural Layer Comparison Using 150 µm-length Extensional Mode Square Plate Resonators... 82

Table 5.1 Frequency and Electrical Characteristics in Air of GSG and Wire-bonded Measurements. 85

Table 5.2 Electrical Parameters Extracted from the Measured Devices Through GSG on-Wafer Probing and Wire-bonded Approaches. 86

Table 5.3 Theoretical Sensitivity Analysis, and Resonator Performance Parameters in Air and Vacuum. 87

Table 5.4 FIB Settings for Platinum Deposition... 89

Table 5.5 Analytic Results for FIB Platinum Deposition. 89

Table 5.6 150 µm-width Extensional Mode Mass Sensing Parameters 98

المنارة للاستشارات
www.manaraa.com

LIST OF FIGURES

Figure 1.1 Illustration of basic MEMS detection.. 2

Figure 1.2 Three major application that resonant sensors are commonly used for. 4

Figure 1.3 Common MEMS-CMOS integration techniques: (a) hybrid integration and (b) monolithic integration. 5

Figure 2.1 3D illustration of a 2-port thin-film piezoelectric square plate resonator with drive and sense ports. 14

Figure 2.2 Illustration of the direct and converse piezoelectric effects [32]. 15

Figure 2.3 Categories of MEMS device technologies based on both direct and converse piezoelectric effects. 16

Figure 2.4 Illustration of the linear electromechanical equation state for converse and direct piezoelectric effects. 18

Figure 2.5 3D illustration of a ZnO-on-Si resonator showing all of its key components............ 20

Figure 2.6 3D illustration of a capacitive-transduced resonator at resonance. 22

Figure 2.7 Illustration of an isotropic cube with three common resonant modes depicted. 25

Figure 2.8 Illustration of the (a) mechanical and (b) electrical equivalent circuit models; and (c) a complete electromechanical model of the device. 29

Figure 2.9 2D illustration of the dynamic mass of a 2nd contour mode disk resonator. 30

Figure 3.1 FEM nodal analysis using COMSOL Multiphysics® of a circular membrane vibrating at the first 4 contour modes. 33

Figure 3.2 Electrode and anchor design approaches: (a) 1st contour resonant mode characteristics and anchor location used to create a (c) 3D device matching model, (b) 2st contour resonant mode characteristics and anchor location used to create a (d) 3D device matching model. 34

www.manaraa.com

Figure 3.3 Oxidation air-gap reduction fabrication process flow: (a) PECVD and LPCVD deposition of SiN and Polysilicon accordingly, (b) HAR DRIE of polysilicon/SiN hard mask, (c) 1 μm-thick furnace wet oxidation of the hard mask, (d) HAR DRIE of Si and hard mask removal, (d) gold contact pads and release, (d) backside release via HAR DRIE of Si. 35

Figure 3.4 SEM of fabricated devices: 2nd extensional contour and 1st extensional contour designs for (a)(c) square and (b)(d) circular membranes accordingly. 36

Figure 3.5 SEM image of air-gap reduction results after 1 μm wet furnace oxidation 38

Figure 3.6 (a) Fluorine Si isotropic etch; (b) Passivation step where a Teflon-like material conformal deposition for sidewall protection; (c) De-passivation step horizontal surface removal of Teflon-like material after O_2 plasma at low temperatures; (d) Bosch sidewall roughness profile. 39

Figure 3.7 SEM of a sidewall roughness profile after a standard Bosch recipe DRIE silicon etch run in an Alcatel AMS 100 ICP System with an scalloping depth (S.D.) of 271nm. 40

Figure 3.8 2D illustration of the capacitance behavior (a) inside of an air-gap with a known distance and the (b) its equivalent circuit model... 41

Figure 3.9 DRIE Bosch etch profile after the passivation values were altered: (a) Etch rate vs. pulse time graph of altered values and (b) the SEM image of the modified etch profile. 42

Figure 3.10 SF_6 pulse modified profile data: (a) graph of modified SF_6 pulse vs. Si etch rate and (b) graph of modified SF_6 pulse vs. scallop depth....................................... 43

Figure 3.11 SEM images of SF_6 pulse modified sidewall profile at -15°C: (a) overview of the anisotropic sidewall profile, and (b) close-up image of the scalloping depth (S.D.) size.. 43

Figure 3.12 SEM images of SF_6 pulse modified sidewall profile at -20 C°: (a) overview of the sidewall anisotropic profile and (b) close-up image of the scalloping depth (S.D.) size... 44

Figure 3.13 Step-by-step illustration of the thin sacrificial layer air-gap reduction fabrication process flow:(a) a SOI wafer as the starting substrate; (b) HAR DRIE Si resonator etch; (c) 100nm of Al_3O_2 ALD layer; (d) Au/Cr seed layer; (e) Gold electroplated electrodes; (f) front-side B.O.E release; (g) backside HR DRIE release followed by B.O.E; (h) optional solid gap profile by HR DRIE backside etch followed by SiO_2 DRIE release dry etch. 45

Figure 3.14 SEM of front-side released device with 100nm air gap. 47

www.manaraa.com

Figure 3.15 SEM of suspended device after backside release of HAR DRIE Si etch. 47

Figure 3.16 SEM of suspended device after backside release with a 290nm air-gap capacitive gap.. 47

Figure 3.17 SEM of front-side fabricated devices with circular and square design for 1st contour and lateral resonant mode. 48

Figure 3.18 Illustration of RF test set-up for capacitive devices 49

Figure 3.19 Breakdown voltage (B.V.) results for (a) ~100 nm front-side released capacitive gap; (b) a ~250 nm backside released capacitive gap; (c) capacitive gaps with particles due to capillary forces. 50

Figure 3.20 Transmission response of 50 µm-radius disk resonator before and after a DC bias voltage is applied. 50

Figure 3.21 Simulation of resonator response: (a) measured spectrum compared to simulated responses for 5V and 25V and (b) simulated responses of 5V and 25V using measured C_f. 50

Figure 4.1 Electrode and anchor design approaches for a 1st contour resonant mode and anchor location used to create a 3D device matching the FEM COMSOL Multiphysics® modal analysis model.. 52

Figure 4.2 Electrode and anchor design approaches using FEM COMSOL Multiphysics® modal analysis that models a N3 length-extensional resonant mode needed to create a 3D device matching model. 53

Figure 4.3 Step-by-step illustration of the piezoelectrically-transduced resonator fabrication process flow; (a)bottom lift-off process of sputtered platinum; (b) reactive sputter deposition of ZnO thin piezoelectric film; (c) via opening through ZnO wet etching; (a) top electrode lift-off process of sputtered platinum; (d) ZnO dry DRIE etching of the resonator... 53

Figure 4.4 Lift-off profiles using: (a) negative photo resist; (b) positive photoresist; (c) LOR-3B in combination with positive photoresist. 55

Figure 4.5 Optical images of lift-off profiles after using: (a) (NR9-3000PY) negative photoresist; (b) AZ1512 positive photoresist; (c) LOR-3B and AZ1512 57

Figure 4.6 XRD of a 500nm sputtered ZnO layer after annealing treatments: (a) no treatment; (b) 300°C for 1hour; (b) 400°C for 1 hour. 58

www.manaraa.com

Figure 4.7 2D illustration of four different release techniques: (a) device perspective without release, (b) DRIE SF_6 isotropic dry release, (c) TSV HAR DRIE backside dry release, (s) 49% HF pre-release, (c) SRE dry release 59

Figure 4.8 2D illustration of ZnO-on-Si backside release: (a) TSV HAR DRIE Si backside etch followed by (b) a SiO2 DRIE release etch 60

Figure 4.9 2D illustration of oxide pre-releasing: (a) pre-release profile after HAR DRIE and 1 hour of 49% HF, (b) device cross-sectional profile after all fabrication steps are done. 61

Figure 4.10 2D illustration of the TPoSCRE release technique: (a) HAR Si DRIE dry etch of Si; (b) ALD deposition of 30 nm Al_2O_3 layer; (c) SiO2 DRIE etch of horizontal Al_2O_3 layer; (d) Si DRIE isotropic release etch of Si. 62

Figure 4.11 Illustration of RF test set-up for on-wafer probing characterization of piezoelectric actuated resonators. 63

Figure 4.12 SEM photos of 1st contour mode thin-film ZnO resonator after the releasing step. 64

Figure 4.13 Measured forward transmission frequency response of a 38 µm-radius 1st contour mode thin-film ZnO disk resonator. 64

Figure 4.14 SEM images of 150 µm-length extensional ZnO square resonators: (a) n5 and (b) n9. 65

Figure 4.15 Captured forward transmission response demonstrating the effects of ZnO buckling in a N3 150µm-length extensional square resonator.................................. 66

Figure 4.16 SEM images of TSV released ZnO-on-Si 1st contour mode disk resonator. 67

Figure 4.17 Measured forward transmission frequency response of a wide frequency span of 30 kHz to 50 MHz from a 1st contour mode 88 µm-radius disk resonator. 68

Figure 4.18 Measured forward transmission frequency response of a strong 4th order contour mode response from a 1st contour mode 38 µm-radius disk resonator. 69

Figure 4.19 (a) Measured s-parameters from disk resonators diameters ranging from 100 µm to 300µm; (b) Line graph comparing measured data versus theoretical predictions. 70

Figure 4.20 Top electrode design for a N3 length-extensional mode square plate resonator using (a) total displacement; (b) strain field rendering from COMSOL® FEM simulation; and top electrode spacing design with (c) λ/16, (d) λ/8, and (e) λ/4 of electrode-to-electrode spacing. 71

www.manaraa.com

Figure 4.21 Measured transmission responses of a 200 µm square plate resonator in N3 length-extensional mode with top electrode spacing design of (a) λ/16; (b) λ/8; and (c) λ/4. 72

Figure 4.22 3D models of three different electrode design created to match the strain field: (a) Top-electrode matching; (b) bottom electrode matching; and (c) top-and-bottom electrode matching.......... 73

Figure 4.23 Measured S-parameters of a 150 µm square resonators in its N3 length-extensional mode with three different electrode design created to match the strain field: (a) Top-electrode matching; (b) bottom electrode matching; and (c) top-and-bottom electrode matching.......... 73

Figure 4.24 Measured forward transmission frequency responses of a N3 96µm-width extensional mode with five different W/L ratios: (a) W/L=1; (b) W/L=0.8; (c) W/L=0.6; (D) W/L=0.4; and (E) W/L=0.4. 74

Figure 4.25 Measured forward transmission frequency responses for square plate higher order mode 150µm-length extensional resonator designs: (a) N3; (b) N5; (c) N9; and (d) SEM images of electrode configuration for N3, N5, and N9. 76

Figure 4.26 Measured transmission frequency response of a strong 29th 150 µm-width extensional harmonic response from a N9 design. 77

Figure 4.27 (a) Measured forward transmission frequency responses from ZnO-on-Si square plate resonators with lengths ranging from 96 µm to 300 µm; (b) Line graph comparing measured data versus theoretical approximations. 78

Figure 4.28 SEM top-view and cross-sectional views photos of a 1st contour mode thin-film ZnO-on-polysilicon contour mode disk resonator after fabrication. 79

Figure 4.29 (a) XRD and (b) AFM results of the LPCVD polysilicon layer of the home-made poly-SOI substrate. 80

Figure 4.30 Measured forward transmission frequency responses for ZnO-on-PolySi 1st contour mode disk resonators with different radiuses for: (a) 38 µm-radius disk 1st contour mode; (b) frequency response of 1st contour mode disk resonators with different radiuses. 80

Figure 4.31 Measured forward transmission frequency response of a ZnO-on-PolySi 60 µm-width extensional N3 rectangular shaped resonator. 81

Figure 4.32 (a) Measured forward transmission frequency response; and (b) TCF comparison of structural layers fabricated in this work using 150 µm-length extensional mode square plate resonators. 81

www.manaraa.com

Figure 4.33 SEM cross-sectional view photos of released devices using the TPoSCRE technique: (a) 25 μm-radius disk resonator with a (b) device layer of 8 μm and (c) a unreleased rectangle resonator with a device layer of 4 μm using the 2 hours of anisotropic DRIE SF_6 release dry etch. 83

Figure 4.34 Measured forward transmission frequency responses TPoSCRE released 1st contour disk resonators with a radius of (a) 25 μm and (b) 38 μm. 83

Figure 5.1 Measured frequency responses from GSG on-wafer probing and wire-bonded measurements in air. 85

Figure 5.2 Illustration of (a) the vacuum test-set up and the measured forward transmission frequency responses (b) the measured resonant frequency and Q factors in air and vacuum. 86

Figure 5.3 Measured zero span spectrum phase noise at the resonance frequency. 87

Figure 5.4 (a) AFM analysis of FIB deposited micro-pellet and (b) SEM image of multiple Pt depositions on a gold coated substrate. 88

Figure 5.5 (a) SEM photo of Pt FIB deposition on the maximal displacement points; (b) COMSOL® FEM simulation of a 4th contour mode response demonstrating the placement of added mass at the maximal displacement points. 90

Figure 5.6 Measured forward transmission frequency responses demonstrating the frequency shift after four FIB Pt deposition on the maximal displacement points in (a) air; (b) high vacuum (>10^{-5} Torr); (c) vacuum (~10^{-3} Torr); (d) plot of R_m versus added mass in high vacuum. 90

Figure 5.7 (a) SEM photo and (b) modal analysis of Pt FIB deposition micro-pellets at the minimal displacement points; (c) measured forward transmission responses demonstrating the frequency shift after FIB Pt depositions on the minimal displacement points in high vacuum (>10^{-5} Torr); (d) R_m versus added mass in high vacuum. 91

Figure 5.8 3D schematic showing the general characteristics of MOF layers delineating their gas absorption mechanisms. 93

Figure 5.9 SEM images of four different MOF crystals synthetized on top to a silicon substrate with gold patterns: (a) Zn(BDC); (b) Cu-BTC; (c) Fe-MIL-88b; (d) HKUST-1. 94

Figure 5.10 (a) SEM and (b) optical images of HKUST-1 crystals showing a well-defined crystal structure and visible size variation. 95

www.manaraa.com

Figure 5.11 SEM images of (a) wire-bonded device, (b) the same sensor device with FIB micro-pellets for calibration; and (c) zoom view of it. 95

Figure 5.12 Optical images of the localized placement of HKUST-1 MOF crystals on top of a N5 width-extensional mode resonator. 96

Figure 5.13 Measured forward transmission frequency responses of (a) N5 mode and (b) N9 mode demonstrating the mass sensing capabilities of a N5 width-extensional mode square plate resonator. 97

Figure 6.1 Illustration of ultra-sensitive gas sensor concept: (a) ZnO-on-Si device characterization, (b) selective MOF crystal growth on top electrodes and (c) gas absorption test. 102

Figure 6.2 Illustration of ultra-sensitive gas sensor concept and test-set up. 103

www.manaraa.com

ABSTRACT

Sensing devices developed upon resonant microelectromechanical and nanoelectromechanical (M/NEMS) system technology have become one of the most attractive areas of research over the past decade. These devices make exceptional sensing platforms because of their miniscule dimensions and resonant modes of operation, which are found to be extremely sensitive to added mass. Along their unique sensing attributes, they also offer foundry compatible microfabrication processes, low DC power consumption, and CMOS integration compatibility. In this work, electrostatically and piezoelectrically actuated RF MEMS bulk resonators have been investigated for mass sensing applications. The capacitively-transduced resonators employed electrostatic actuation to achieve desired resonance mode shapes. These devices were fabricated on silicon-on-insulator (SOI) substrates with a device layer resistivity ranging from 0.005 Ω cm to 0.020 Ω cm. The electrode-to-resonator capacitive gap was defined by two different techniques: oxidation enabled gap reduction and sacrificial atomic layer deposition (ALD). For oxidation enabled gap reduction, a hard mask composed of silicon nitride and polysilicon is deposited, patterned, and defined using standard MEMS thin-film layer deposition and fabrication techniques. The initial lithographically-defined capacitive gap of 1 µm is further reduced to ~300 nm by a wet furnace oxidation process. Subsequently, the reduced gap is transferred to the device layer using a customized dry high-aspect-ratio dry etching technique. For sacrificial approach, a ~100 nm-thin ALD aluminum oxide sidewall spacer is chemically etched away as the last microfabrication step to define the ~100 nm capacitive gap. Small capacitive gaps developed in this work results in small motional resistance (R_m) values, which relax the need of the read-out circuitry by enhancing the

المنارة للاستشارات
www.manaraa.com

signal transduction. Piezoelectrically-actuated resonators were developed using thin-film bulk acoustic resonant (FBAR or TFBAR) and thin-film piezoelectric-on-substrate (TPoS) technologies with reported Q factors and resonant frequencies as high as 10,638 and 776.54 MHz, respectively, along with measured motional resistance values as low as 169Ω. To the best of our knowledge, this work is the first one that demonstrated TPoS resonators using LPCVD polysilicon as an alternative low loss structural layer to single-crystal silicon with Q factors as high as ~3,000 (in air) and measured motional resistance values as low as 6 kΩ with an equivalent acoustic velocity of 6,912 m s^{-1} for a 7 µm thick layer. Polysilicon based TPoS single devices were measured with the coefficient of resonant frequency of -3.77 ppm/°C, which was the lowest ever reported for this type of devices. Also a novel releasing process, thin-piezo on single crystal reactive etched (TPoSCRE), allows us to develop of TPoS resonators without the need to SOI wafers. The fabricated devices using this technique were reported with Q factor exceeding ~1,000 and measured motional resistance values as low as 9 kΩ.

The sensitivity of a fourth-order contour mode ZnO-on-SOI disk resonator based mass sensor was determined by performing multiple depositions of platinum micro-pallets using a focus ion beam (FIB) equipped with gas injection system on strategically-chosen locations. It was found out that the sensitivity of the resonator on its maximal and minimal displacement points was of 1.17 Hz fg^{-1} and 0.334 Hz fg^{-1}, respectively. Also, the estimated limit of detection of the resonator was found to be a record breaking 367 ag (1 ag = 10^{-18}g) compared to devices with similar modes of resonance. Lastly, a lateral-extensional resonator was used to measure the weight of HKUST-1 MOF crystal cluster. The weight of it was found to be 24.75 pg and 31.19 pg by operating two lateral resonant modes, respectively.

www.manaraa.com

CHAPTER 1 INTRODUCTION

In order to have a better understanding of our world, we have developed technology that can translate the unknown into simple bits of knowledge. Such technology has enable us to make smarter choices and find solutions to problems that were otherwise impossible to solve. One of the milestones of sensing of technology was the oxygen probe by Professor Leland C. Clark in 1956. This device was able to monitor and control of blood and tissue oxygen tensions circulating in heart-lung machines enabling safer and more containable open heart operations[1]. Few years later, he expanded the idea of the oxygen sensor into a more user friendly enzyme-based transducer known as “enzyme electrodes” in 1962 [2], thus allowing millions of diabetics to monitor their own blood-sugar levels. Thereafter, more technological advances in sensing technology, for numerous medical applications, branched out from these concepts helping millions of people to live a better life. Since the early 1970s, many astonishing advances in the field of micro-electro-mechanical-systems (MEMS) have enabled the exploration of transduction mechanisms that take advantage of mechanical energy primarily based on the mechanical phenomena. As a result, an innovative family of chemical and biological sensors has rapidly emerged. One of the most popular sensing methods for chemical/biomedical sensors is the detection through the mass loading effect. The concept of mass sensing using MEMS devices was developed shortly after the evolution of the atomic force microscopy (AFM) in the early 1980’s. By monitoring deflection and resonant frequency of a microfabricated cantilever, the AFM is capable of measuring ultra-small forces exerted towards a micro-cantilever down to a single atom [3]. Due to incredible sensitivity demonstrated by these microfabricated cantilevers, researchers around the world began to exploit

www.manaraa.com

those characteristics especially for mass sensing applications. In many fields, very sensitive transducers are needed to quantify ultra-small amounts of loaded mass for detection purposes. As technology advanced, more MEMS transducers were developed for this purpose with different ranges of sensitivity. Now days, to build a mass sensor, a large number of MEMS transducers are available and they can be selected depending on the weight and size of the targeted physical, chemical, or biological stimuli. MEMS single-clamped or double-clamped suspended beams, and released diaphragms are known to be the most sensitive transducers up to date. When a MEMS device becomes a physical transducer, it can be used directly sense a load in a label-free environment. For targeted detection, a receptor layer is strategically functionalized in a way that measurable output signals can be produced in response to specific stimuli through which ultra-sensitive mass sensors have already been demonstrated [4]. But the wide acceptance of many of them has been hindered by the complexity of their testing schemes and/or fabrication processes.

1.1 MEMS Sensor

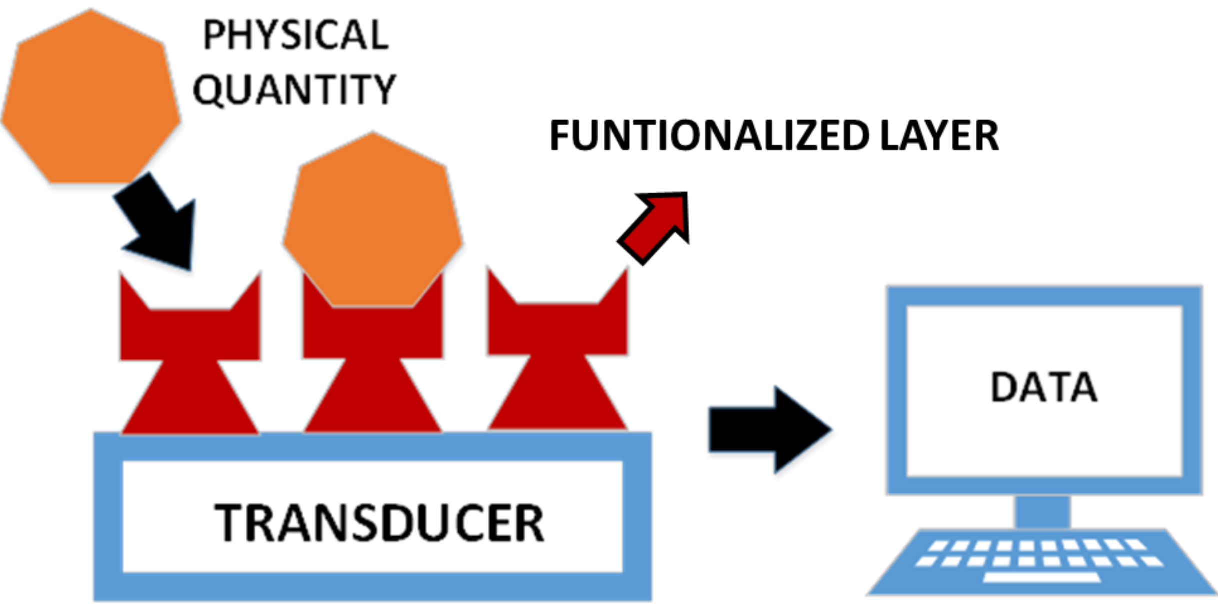

Figure 1.1 Illustration of basic MEMS detection.

www.manaraa.com

A MEMS sensor can be defined as a transducer that converts an unknown physical quantity using known electromechanical mechanisms into quantifiable data. As seen in Figure 1.1, a transducer responds to a stimuli from an unknown physical quantity and produces electrical response that can be interpreted as data using a signal processing unit. For targeted applications, a tailored structure known as the functionalized layer is used.

There are a large number of commercially available MEMS devices such as accelerometers, pressure sensors, gyroscopes, temperature sensors, frequency reference oscillators, and mass sensors, just to name a few. Most of these devices are designed to measure fundamental physical quantities as listed in Table 1.1.

Table 1.1 Fundamental Physical Quantities.

Base quantity	Symbol	Si unit
Mass	m	Kilogram (kg)
Length	l	Meter (m)
Time	t	Second (s)
Electric current	I	Ampere (A)
Temperature	T	Kelvin (K)
Amount of substance	n	Mole (mol)
Luminous Intensity	L	Candela (cd)

MEMS devices are fabricated using microfabrication techniques that are widely used in semiconductor manufacturing. The major techniques for microfabrication are lithography, film deposition, dry and wet etching, doping and polishing. The complexity of the micro-fabrication can be measured by the number of processing steps needed to fabricate the device. Some simple-to-fabricate devices such as chemiresistor gas sensors can be composed of a single

www.manaraa.com

microfabrication step. At the other end, mass resonant sensors are known to be very complex devices that often tend to require multiple microfabrication steps.

1.2 Resonant MEMS Mass Sensors

A resonant MEMS mass sensor is a transducer that produces a frequency response when added mass changes the equilibrium state of the transducer. This data can be obtained and process by electronics, then it can be analyzed and interpreted using analytical techniques. The resulting signal is used to make appropriate determination to the change of mass on the transducer. As shown in Figure 1.2, there are three major applications that resonant mass sensors have been used for.

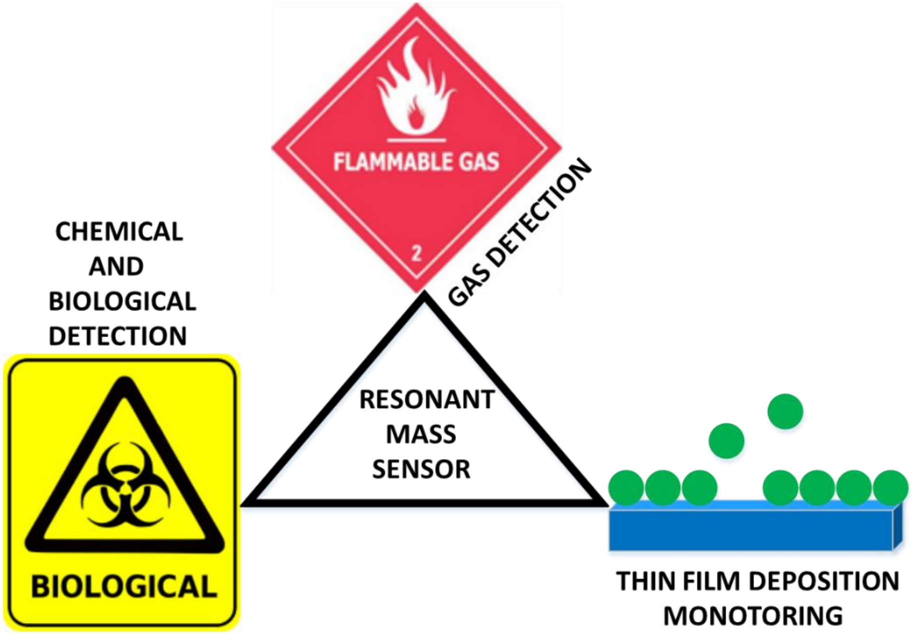

Figure 1.2 Three major application that resonant sensors are commonly used for.

There is a large well-known family of resonant sensors that can be categorized in two major transduction modes: piezoelectric and capacitive. Piezoelectric transduction allows electrical energy to be converted to acoustic energy mechanically via a polarized layer (piezoelectric material), and vice versa. Capacitive transduction enables electrical energy to be converted into

www.manaraa.com

acoustic energy via a variable potential in a dielectric gap, and vice versa (see chapter 2 for more detail analysis of both transduction modes). Both modes have their advantages and disadvantages which can play a very important role while determining the best suited application they can be used for.

1.3 CMOS-MEMS Integration

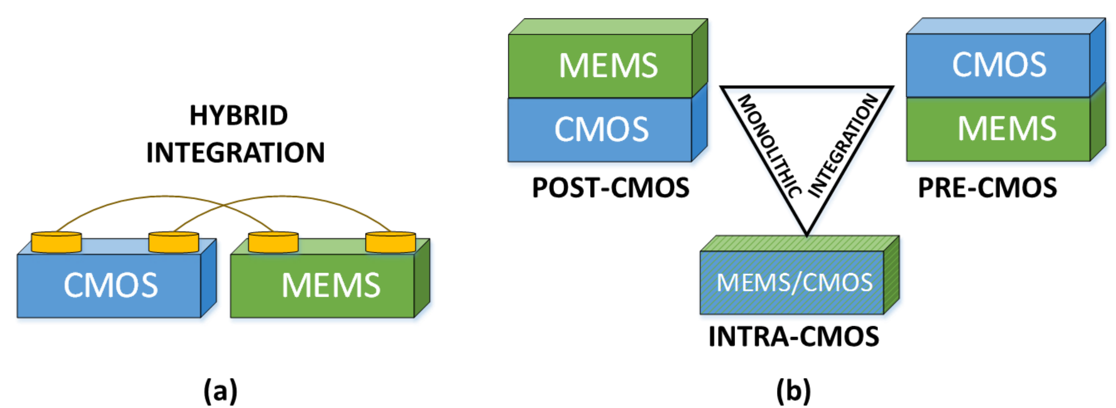

Figure 1.3 Common MEMS-CMOS integration techniques: (a) hybrid integration and (b) monolithic integration.

CMOS compatible technology is widely acclaimed because MEMS devices are manufactured using batch fabrication techniques, and integrated with IC interconnects and read-out circuits. The most common CMOS-MEMS integration technique consists of processing both chips separately followed by wirebonding. This technique is known as hybrid integration. It is not a practical approach because this technique increases the manufacturing cost while demanding special packaging techniques. Such drawbacks delay the commercialization of this type of technology. Therefore, a more compact approach where both a MEMS device and its read-out circuitry that can be integrated in the same chip is preferred. Combining both the MEMS devices and the readout circuit in the same die results in lower packaging cost and increases the circuit performance. This is achieved because less number of off-chip electrical connections are needed.

www.manaraa.com

This technique is also known as monolithic integration. There are three approaches that are widely used to integrate MEMS devices with IC components using monolithic integration: pre-CMOS, intra-CMOS and post-CMOS processing.

For pre-CMOS processing, the MEMS device is completely fabricated before the CMOS. The advantages of this process is that the MEMS device can be fabricated using very complex techniques that might not be otherwise CMOS compatible. In addition, high temperature processes can also be employed. However, integrating CMOS with prefabricated MEMS devices is very challenging. That is because some of standard CMOS processes need to be modified in order to prevent damaging to the prefabricated MEMS structure. Which makes it very challenging and expensive.

On the other hand, intra-CMOS is an approach where both the MEMS and CMOS can be fabricated in parallel. This approach is ideal because the overall fabrication becomes cheaper and it can also be adapted for batch production using same foundry. However, this approach has a lot of design limitations that often requires extensive modifications to existing CMOS fabrication standards. In some cases, material modifications are needed, which limits the best achievable microsystem performance.

Finally, post-CMOS is an approach where the MEMS is fabricated after the CMOS has been created. This approach is widely known to have great advantages such as: the fabrication of the CMOS and the MEMS using different foundries, the integration of MEMS without affecting standard CMOS fabrication techniques, and the MEMS can be fabricated on top of the CMOS reducing the overall size of the device and parasitics. The disadvantages of this approach often occur when the deposition temperature of the structural layer is too high which can alter the performance of CMOS circuitry underneath [5].

www.manaraa.com

1.4 Previous Work on Resonant Mass Sensors

Resonant mass sensors have gained a great deal of interest over the years due to their intrinsic high sensitivity and wide deployment in numerous apparatus and instruments. These devices have been implemented in various disciplines of science and technology for mass-loading applications, especially for biosensors [6]. Some of the most successful resonant mass sensing technologies in the recent years are: quartz crystal microbalance (QCM), bulk acoustic (BAR), surface acoustic wave (SAW) resonators, and MEMS cantilever.

In 1959, Sauerbre derived a series of equations that predicted the changes in the resonant frequency correlated to mass-loading on piezoelectric crystals [7]. Ever since, scientist around the world began to explore the mass loading effects on piezoelectric transducers. QCM shear-mode resonators were among the first devices ever being explored because they are built on a custom cut, thin piezoelectric quartz plates with coated electrodes. When actuated, it generates an acoustic wave that propagates perpendicular to the crystal surface. By monitoring the frequency shift, the loaded mass can be determined by Sauerbre's equation (1.1):

$$\Delta m = -C * \Delta f \tag{1.1}$$

where Δm is the change of mass, C is the mechanical and electrical characteristics of the quartz crystal and Δf is the change of resonance frequency.

QCM is an attractive technology because it can be cheaply fabricated in mass quantities. Even though this technology has been widely used for mass sensing applications, its mass sensitivity is very limited due to the relative large sizes of the piezoelectric quartz which limits its working frequency. Therefore, as observed in equation (1.1), the working frequency is directly correlated to the mass sensitivity. For these devices, it is difficult to achieve resonances higher

www.manaraa.com

than 10 MHz in most cases [8]. Also, relative low Q factors (<200) are achieved due to the losses of its piezoelectric transduction mode, which leads to lower mass sensitivity and resolution.

Bulk acoustic wave (BAW) technology emerged as an alternative solution to address QCM's low resonant frequencies, making it a stronger candidate for mass applications [9]. The structure and working principle of BAW devices are very similar to those of the QCM. The major difference is that BAW devices use a deposited thin piezoelectric layer (ZnO or AlN) with nominal thickness of 100 nm-2 μm sandwiched between two electrodes, which is thinner than the quartz crystals allowing higher working frequencies. This transduction technique allows the resonator to have less acoustic energy losses compared to quartz crystal technology. As a result, a slightly better Q factor is obtained. Due to the similar working principle of BAW and QCM devices, the mass sensitivity can be closely governed by equation (1.1). Aside from their greatly increased resonance frequencies, BAW resonators with frequencies in the GHz range have exhibited sensitivity up to three orders of magnitude higher than that of the best QCM devices. Some of the most commonly used BAW resonators for mass sensing applications are solid mounted resonators (SMR) [10] and film acoustic resonators (FBAR) [11]. However, because BAW resonators require multiple layers, the micro fabrication of these devices tends to be quite cumbersome. Also, similarly to QCM, only moderate Q factors (<500) can be achieved due to the losses of its piezoelectric transduction mode. Additionally, liquid media sensing applications are very limited because film squeeze damping further degrades the Q factor, which leads to lower mass sensitivity and resolution.

Surface Acoustic wave (SAW) sensors emerged as a solution for highly sensitive detection in liquid media biomedical [6]. The mass sensitivity of these devices can be modeled by the following equation derived from perturbation theory for an acoustically thin, perfectly elastic film:

$$\Delta f \cong (k_1 + k_2) f_0^2 m A^{-1} \tag{1.2}$$

www.manaraa.com

where Δf is the frequency shift due to mass loading; k_1 and k_2 are the piezoelectric electrical and mechanical characteristics; f_o is the nominal resonance frequency, m is the added mass, and A is the sensing area of the device.

SAW resonators generate and detect acoustic waves at resonance using two interlocking, comb-shaped, metallic structures known as interdigital transducers (IDT) on the surface of the piezoelectric film or substrate. This allows the acoustic wave energy, when electrically actuated, to be strongly confined on the surface of the device regardless of its thickness, thus minimizing induced damping introduced by liquid media [12]. Therefore, mass sensors have been reported with high working frequencies between 100 MHz to low GHz [13]. However, the SAW technology offers relatively limited operation frequency range, as excessive scaling of interdigital transducer pitch size is required to reach GHz frequencies, which in turn limit the best achievable sensitivity. Also, similarly to other piezoelectric technologies, the Q factor tends to be relatively low (<1000), therefore affecting the mass resolution of these devices.

M/NEMS technology has enabled us to develop mass sensors that rely on the mechanical phenomena [3]. This technology has been extensively studied for the past few years because it has the potential to yield the most sensitive devices up to date. There are two important M/NEMS mass sensor devices: M/NEMS beam and MEMS bulk-mode plate sensors. MEMS beam mass sensors emerged right after the development of micromachined cantilevers in the 1980's [14]. These devices are known as the most sensitive devices up to date with a record setting mass resolution of 1.7 yg (1 yg=10^{-24} g) at 2GHz in vacuum, using a suspended clamped carbon nanotube [15]. There are two common modes of sensing for beam sensors: static and dynamic. In static mode, the target analyte causes the beam to bend due to surface stress, whereas the surface-

www.manaraa.com

attached analytes cause a shift in the beam's resonant frequency due to mass loading for the case of dynamic mode.

For mass sensing applications, dynamic mode is the most widely used sensing technique [16]; mass-loading effect can be detected by monitoring the mechanical resonance frequency change of the beam resonator given by:

$$\Delta f \cong \frac{f_n}{2m_e}\Delta m \tag{1.3}$$

where Δm is the change of mass, Δf is the measurable frequency shift, and m_e is the effective mass of the resonator (also known as the dynamic mass).

As observed in equation 1.3, to be able to achieve the highest possible sensitivity, an extremely tiny beam needs to be considered in the design. This however makes the sensor more susceptible to external perturbations caused by the environment, thus demanding operation under ultra-high vacuum. Therefore, new ideas been proposed to solve this issue such as the implementation of buried micro-channels inside a suspended beam [4]. This technique offers a way to detect bio-molecules in liquid media inside the beam resonator while operating under ultra-high vacuum test environments. There are two main actuation methods to drive beam resonator into resonance, which are piezoelectric and electrostatic. Piezoelectric beam resonators use only signals in the electrical domain for actuating and sensing the changes of frequency in the device. However, just like previously reviewed piezoelectric devices, the response is restricted by the piezoelectric materials' mechanical and electrical material properties. For electrostatic actuation, an AC voltage drives directly the beam into resonance and optical detection methods track the any changes in the mechanical resonant frequency. Optical detection, consisting of a laser diode focused on the suspended beam, tracks any changes in the resonant frequency caused by mass

www.manaraa.com

loading detected by a sensitive photodetector (PSD). However, this technique has a limited cutoff frequency (<1GHz) due to the response time of the optical detector and readout circuit. Also, M/NEMS beam devices with the nano-scale geometry not only demands costly and mass-production incompatible processes, but also require in vacuum operation to mitigate the air damping effect.

MEMS bulk-mode plate sensors have become an alternative to overcome the limitations imposed by M/NEMS beam resonant technology [17]. Similarly to M/NEMS beam sensors, there are two common mode of sensing: static and dynamic. Dynamic mode is the most interesting method, which employs the mass-loading effects. There are also two common transduction methods, which are piezoelectric and electrostatic actuation [18]. Piezoelectric actuation is similar to that of M/NEMS beam sensors where the devices actuation and detection are restricted by the piezoelectric material properties. On the other hand, electrostatic actuation can be monitored by electrical means, which make these sensors fully scalable. Capacitively-transduced resonators also offer high resonant frequencies (>100 MHz) with high factors (>10,000) at atmosphere pressure [19]. Meanwhile, relatively large capturing area due to larger surface area than M/NEMS beam sensors allows quicker detection time [20], and different resonant bulk modes of actuation provide good sensitivity in liquid sensing environments with and without integrated microchannels [21]. Also, newly introduced thin-film piezoelectric-on-substrate resonator (TPoS) devices have a great potential to be utilized in ultrasensitive mass sensing applications. These devices are based on FBAR technology; however, they are strategically coupled with low loss substrates that have higher acoustic velocities [22]. This results in an equivalent acoustic velocity much higher than typical piezoelectric devices. Therefore, this devices have high Q factors and resonant frequencies, and a low motional resistance comparable to capacitive-transduced resonates. To the best of our

www.manaraa.com

knowledge, this dissertation is the first one study the effects of mass loading on TPoS based resonators for mass sensing applications.

In the past few years a great deal of effort has been devoted to study the sensing characteristics of most of the previously mentioned technologies using direct metal write techniques such as the focus ion beam (FIB) platinum nano/micro pellet depositions, and other physical deposition techniques such as e-beam evaporation and sputtering. Using these techniques, research groups have been able to obtain important sensing parameters such as the mass sensitivity and resolution as summarized in Table 1.2.

Table 1.2 Performance Comparison of Several State-of-the-art Sensing Technologies

Device	Resonant Frequency (MHz)	Localized Mass Sensitivity (kHz pg^{-1})	Mass Resolution (fg)
QCM [23, 24]	5		100
FBAR [25]	~2300		9
SAW [26]	200	0.0009	3000
MEMS Microcantilever [27]	~0.350	0.878	
NEMS Nanocantilever [28]	13	5100	0.039
Capacitive Disk [29]	132	31.5	0.130
Capacitive Bar [30]	51	100	0.5
ZnO-on-Si Disk (This work)	85	1.140	0.367
ZnO-on-Si Square (This work)	88.61	0.103	50.8
ZnO-on-Si Square (This work)	150.87	0.191	10.9

المنارة للاستشارات
www.manaraa.com

CHAPTER 2 BACKGROUND AND THEORY

Recent advancement in microfabrication and lab-on-a-chip CMOS integration technology have enable many researchers to develop devices, such as MEMS resonators, to measure very small amounts of mass. These devices have brighten the way for the development of new applications in the fields of science and technology. There three very important parameters used to design an ultrasensitive MEMS resonating mass sensors which are: the resonant frequency of the device, the dynamic mass of the resonant mode, and the Q factor at resonance. There are infinite number resonant frequencies in an elastic material (or resonant modes), this work focuses only in the extensional lateral and contour modes for both disk shape and square plate resonators. The dynamic mass is a very important parameter for determining the sensitivity of the device because it analytically approximates the amount effective mass for the resonant mode of operation. The Q factor determines the limit of detection (LOD) of the device given a measured or theoretical sensitivity value. As previously covered in Chapter 1, there are two strong transduction candidates: thin-film piezoelectric and capacitively transduced resonators, both technologies have been explored in this dissertation.

2.1 Thin-film Piezoelectrically Transduced Resonators

Thin-film piezoelectric MEMS resonators consist of a suspended structure that is composed of a piezoelectric material such as ZnO, AlN, and PZT embedded between two parallel thin film patterned electrodes. The suspended structure is anchored to the body of the device and actuated through a structure known as tethers as illustrated in Figure 2.1. When an AC signal is applied to the driving electrode and it matches the natural resonant frequencies of the piezoelectric

المنارة للاستشارات
www.manaraa.com

layer, a mechanically deformation is induced (also known as indirect piezoelectric effect). The resultant deformation is proportional to the equivalent longitudinal acoustic wave propagation (quazi-longitudinal acoustic velocity or C_{ql}) within the piezo-material crystal layer. The mechanical deformation during resonance directly affects the internal polarization of piezoelectric layer resulting in an electric response (also known as the direct piezoelectric effect) that can be extracted and detected from the sensing electrode.

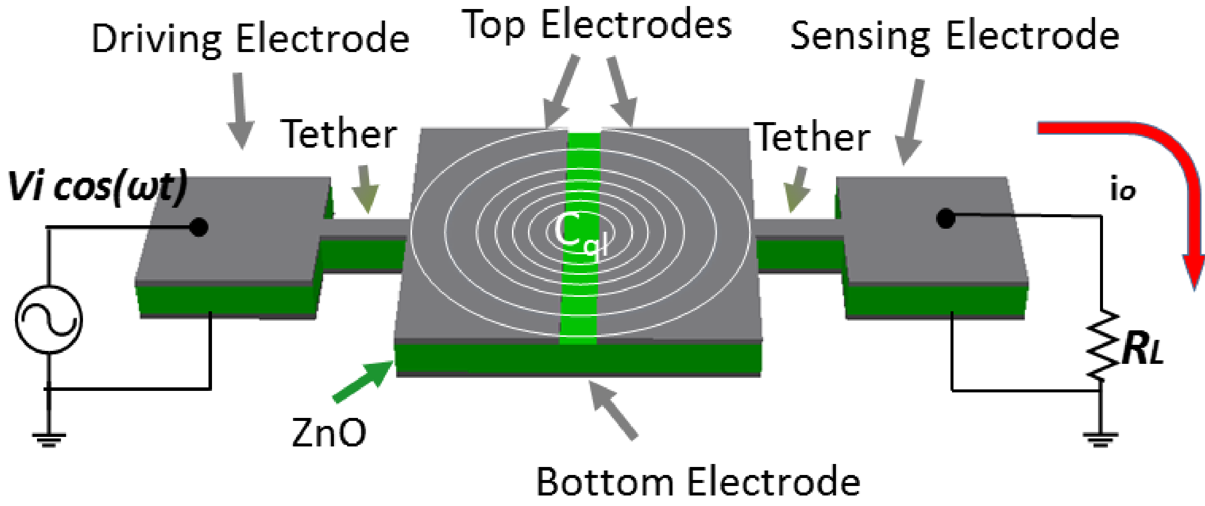

Figure 2.1 3D illustration of a 2-port thin-film piezoelectric square plate resonator with drive and sense ports.

2.2 Piezoelectricity Effect

Piezoelectricity is defined as a linear interaction between mechanical and electrical systems in non-centric crystals or similar structures [31]. A material that expresses piezoelectric characteristics produces an output electrical signal when an external mechanical stress is applied to it. This happens because the internal electric polarization from piezoelectric materials is perturbed by mechanical means and an electrical response is generated because of the induced dielectric displacement. The amount of electric discharge is directly proportional to the strength of the mechanical perturbation on the piezoelectric material. This phenomenon is known as direct

المنارة للاستشارات
www.manaraa.com

piezoelectric effect. Similarly, when an electric field is applied across the piezoelectric material a mechanical deformation is induced. The mechanical deformation is directly proportional of the strength of the electric field. This phenomenon is known as converse (inverse) piezoelectric effect.

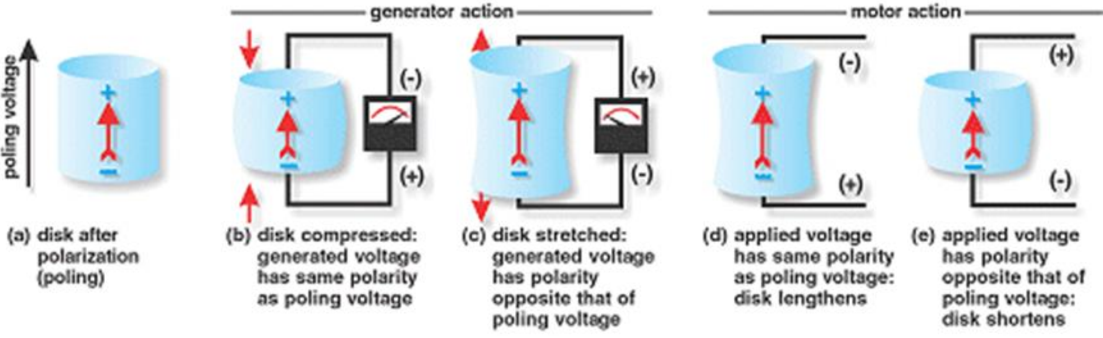

Figure 2.2 Illustration of the direct and converse piezoelectric effects [32].

Ever since the discovery of the piezoelectric properties of quartz by Pierre and Jacques Curie in the 1980's, the study of piezoelectric materials and applications of piezoelectricity have changed the course of technology. Currently, advances in the field of microfabrication technology and a wide choice of piezoelectric materials have enable us to develop sophisticated devices. Most of them have the ability to convert mechanical strain into an electrical signal when they are applied as a stress sensor, similarly they can act as resonant transducer as illustrated in Figure 2.2. There is a vast market that utilizes the unique electrical and mechanical properties of piezoelectricity to create devices that are in huge demand the field of engineering as seen in Figure 2.3. One of the benefits of piezoelectric technology is the ease of fabrication of a great range of device sizes down to few microns. In addition, they can be integrated with today's semiconductor technology. In today market, technologies using the direct piezoelectric effect encompasses the majority commercially available piezoelectric devices. Not far behind, thanks to the advances in field of MEMS microfabrication technology, the converse piezoelectric effect based piezoelectric resonant

www.manaraa.com

technology is advancing fast towards the markets as the strong new comer for numerous applications.

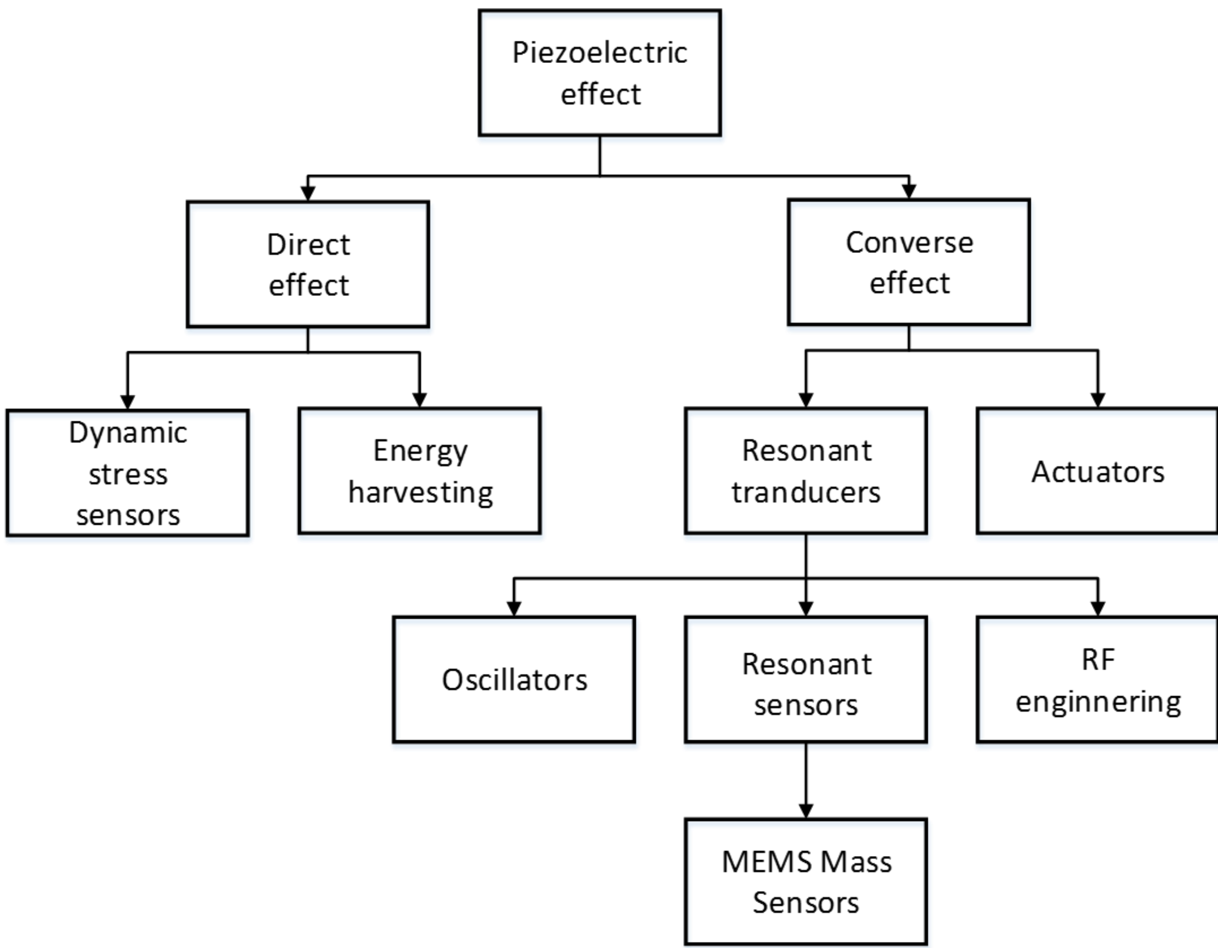

Figure 2.3 Categories of MEMS device technologies based on both direct and converse piezoelectric effects.

2.3 Piezoelectric Materials for MEMS Applications

The discovery of a vast number of piezoelectric materials have enabled us to rapidly advance the field of study for piezoelectric devices. Therefore, a bloom of MEMS devices using the piezoelectric effect as their main mode of actuation has sparked a great number of applications in the fields of science and technology. Piezoelectric materials belong to a crystal group that lacks a center of symmetry. When an applied stress or electric filed yields an asymmetrical ionic

www.manaraa.com

displacement that causes electrical charges or lattice deformation, respectively [32]. There are many natural and synthetic materials that exhibit piezoelectric characteristics that can be branched out in two major categories, piezoelectric ceramics and piezoelectric crystals. Naturally, the piezoelectric effect occurs on monocrystalline structures such as quartz, tourmaline and Rochelle salt. Quartz crystals are in great demand for MEMS applications because of its material properties such as small dielectric loss, thermal stability and great mechanical strength. However, the challenges miniaturization and its relative weak piezoelectric effect compared to piezoelectric ceramics have been a great obstacle preventing it to be fully exploited in the MEMS technology. Piezoelectric ceramics have become the best choice for MEMS piezoelectric devices due to the ease of integrating this technology to current microfabrication methods employed by the semiconductor industry. Also, piezoelectric ceramics' electrical and mechanical properties are compatible or better than quartz crystals. In the recent years, the most popular choices of piezoelectric ceramics are thin films of piezoelectric polymers such as lead-zirconate-titanate (PZT), aluminum nitride (AlN), and zinc oxide (ZnO).

Table 2.1 Properties of the Most Widely Used Piezoelectric Ceramics [31, 33]

Material Properties	Unit	Symbol	ZnO	PZT	AIN
Elastic Modulus	GPA	E	123	53	330
Density	kg m^{-3}	ρ	5676	7600	3260
Acoustic Velocity	m s^{-1}	υ	4655	3300	10400
Poisson Ratio		σ	0.18-0.36	0.25-0.31	~0.24
Piezoelectric Strain Coefficient	pC N^{-1}	d_{31}	-4.7	-130	-1.8
Relative Permittivity		ε_r	9-11	400-1900	8-10
Electrical Resistivity	Ω cm	ρ_e	10^8-10^9	10^7-10^9	10^{10}-10^{14}

www.manaraa.com

2.4 Mathematical Modeling of Piezoelectricity

The mathematical modeling of the piezoelectric effect is essential to understand the behavior of piezoelectric devices. To simplify the mathematical model, the thermodynamic behavior of the piezoelectric layer is going to be held constant. Therefore, the mathematical model can be simplified to represent the relationship between the mechanical and electrical quantities of the system only. To visualize the relationship between variables, a linear electromechanical equation of state can be derived as illustrated in Figure 2.4.

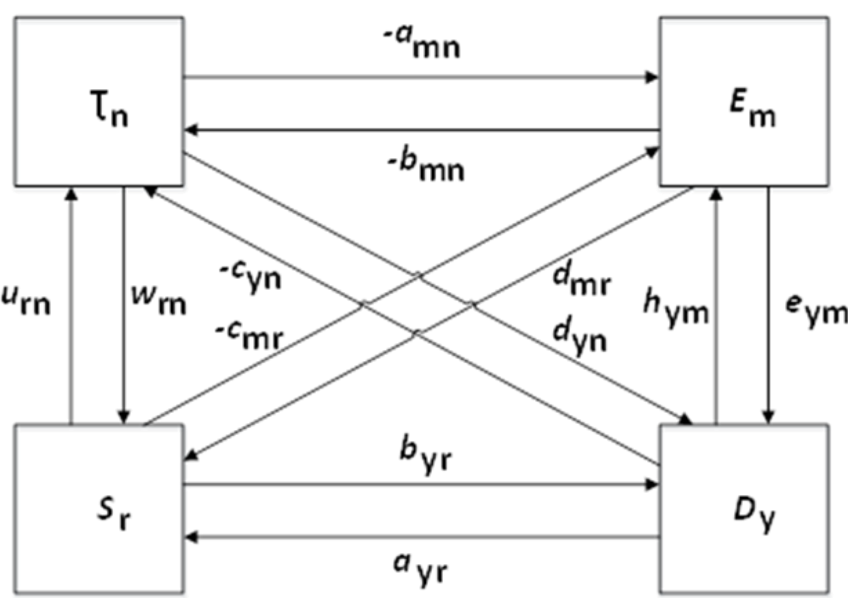

Figure 2.4 Illustration of the linear electromechanical equation state for converse and direct piezoelectric effects.

The arrows represent the relationship between the mechanical quantities T_n or S_r (stress or strain) and electrical quantities E_m or D_y (electric field or electric displacement), which are the first order piezoelectric coefficients. The second order material coefficients connect the relationships between the first order coefficients which can be found in Table 2.2. The relation of each

www.manaraa.com

coefficient depends on the choice of impendent variables and the experimental condition those are obtained with.

Table 2.2 Second Order Material Coefficients [32].

Material properties	Material coefficient	Definition	Si units
Dielectric	Permittivity	$e_{ym} = \frac{\partial D_y}{\partial E_m}$	F m^{-1}
	Impermittivity	$h_{ym} = \frac{\partial E_m}{\partial D_y}$	F^{-1} m
Elastic	Compliance	$w_{rn} = \frac{\partial S_r}{\partial T_n}$	N^{-1} m2
	Stiffness	$u_{rn} = \frac{\partial T_n}{\partial S_r}$	Nm^{-2}
Piezoelectric	Piezoelectric coefficient	$d_{yn,mr} = \frac{\partial D_y}{\partial T_n} = \frac{\partial S_r}{\partial E_m}$	C N^{-1}
	Piezoelectric coefficient	$a_{mn,yr} = -\frac{\partial E_m}{\partial T_n} = \frac{\partial S_r}{\partial D_y}$	C^{-1}m^2
	Piezoelectric modulus	$c_{mr,yn} = -\frac{\partial E_m}{\partial S_r} = -\frac{\partial T_n}{\partial D_y}$	C^{-1} N
	Piezoelectric modulus	$b_{yr,mn} = \frac{\partial D_y}{\partial S_r} = -\frac{\partial T_n}{\partial E_m}$	C m^{-2}

From the linear electromechanical equation of state illustrated in Figure 2.4 and the second order material coefficients found in Table 2.2, the direct and converse piezoelectric equations can be given by:

$$T_n = b_{yr}S_r - c_{yn}D_y \tag{2.1}$$

$$T_n = u_{rn}S_r - b_{mn}E_m \tag{2.2}$$

www.manaraa.com

$$E_m = h_{ym}D_y - a_{mn}T_m \quad (2.3)$$

$$E_m = h_{ym}D_y - C_{mr}S_r \quad (2.4)$$

$$D_y = h_{ym}D_y + C_{mr}S_r \quad (2.5)$$

$$D_y = e_{ym}E_m + d_{yn}T_n \quad (2.6)$$

$$S_r = a_{yr}D_y + w_{rn}T_n \quad (2.7)$$

$$S_r = d_{mr}E_m + w_{rn}T_n \quad (2.8)$$

where equations (2.3)-(2.6) describe the direct piezoelectric effect and equations (2.1), (2.2), (2.7), and (2.8) describe the converse effect.

2.5 TPoS Resonators

Thin-film piezoelectric-on-substrate resonator (TPoS) are a new emerging technology that share the same great advantages as thin-film piezoelectric resonators. The difference between them is that TPoS resonators are fabricated on top of a low mechanical loss substrate like silicon as illustrated in Figure 2.5. TPoS resonators take advantage of the combination of low loss structural layers such as silicon with high electromechanical coupling piezoelectric materials [34]. This combination results in mechanical resonators with moderate to high Q factors and very high to ultra-high resonant frequencies.

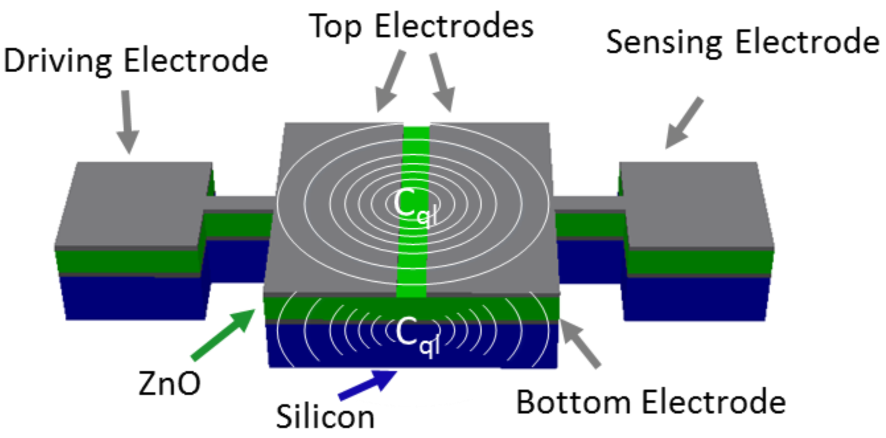

Figure 2.5 3D illustration of a ZnO-on-Si resonator showing all of its key components.

www.manaraa.com

When a piezoelectric resonator is coupled with low loss substrates, the low damping coefficients of the coupling layer tend to dissipate the energy of the device more efficiently. As a result return, higher Q factors can be achieved with minimum effects on the motional resistance. Since the piezoelectric layer can be efficiently coupled with low loss substrate, the equivalent acoustic velocity, C_{ql}, can be found by [35]:

$$C_{ql} = \sqrt{\frac{E_1T_1 + E_2T_2 + \cdots + E_nT_n}{(\rho_1T_1 + \rho_2T_2 + \cdots + \rho_nT_n)(1 - \sigma^2)}} \tag{2.9}$$

where E, T, σ and ρ are the Young's modulus, thickness, Poissons' ratio, and density of the composite layers, accordingly. This equation can also be applied to thin-film piezoelectric resonators since they are composed with more than one layer.

Moreover, the electromechanical coefficient of the fundamental resonant mode, assuming that two or more electrodes are covering the resonator's top surface as seen in Figure 2.5, can be approximated for disk and rectangle resonators by [36]:

$$\eta_{rep,disk} = \frac{Q_T}{U_{max}} \approx E_e d_{31} \pi \frac{1}{2} \tag{2.10}$$

$$\eta_{rep,rectangle} = \frac{Q_T}{U_{max}} \approx N E_e d_{31} l \tag{2.11}$$

where Q_T is the total induced charge on the resonator's surface, U_{max} is the maximum displacement at resonance, E_e is the equivalent Young's modulus, N is the number of electrodes, and l is the length of one of the sides of the top electrodes depending on the resonance mode.

2.6 Capacitively-Transduced Resonators

A capacitively-transduced resonators are electrostatically actuated devices consisting of a suspended geometric membrane (square, circular and rectangular plates are the most commonly used ones) that defines the resonating body of the device. The membrane is held in place by 2 to

www.manaraa.com

4 anchors, which are designed based on the preferred mode of resonance (this will be covered in detail in section 3.1). To operate the device as seen in Figure 2.6, a DC bias is applied to both the input and output electrodes to generate that potential in the capacitive gaps, which are located between the electrodes and the body of the resonator. Then, an AC signal is applied to the input electrode to generate a variable potential which triggers a varying electrostatic force, which once it matches one of the resonant frequencies of the resonant body. This effect is closely related to a time-varying or variable parallel plate capacitor as discussed in section 2.7. The time-varying current (i_0) can be measured to obtain the frequency and electrical characteristics of the devices.

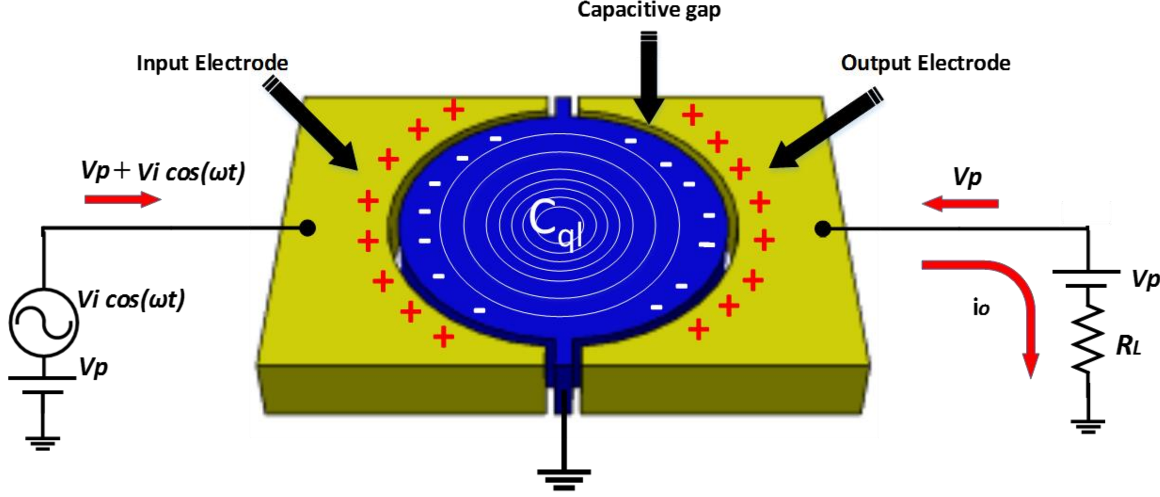

Figure 2.6 3D illustration of a capacitive-transduced resonator at resonance.

2.7 Capacitance of Parallel Plates

In a capacitively-transduced resonator, the capacitance signal transduction can be simplified to the same behavior of a parallel plate capacitor. When a DC, V_p, bias is applied to a capacitively-transduced resonator, an electric field is formed between the electrodes and the body of the resonator. According to Gauss's law, a uniform electric field between two parallel plates separated by a dielectric material with permittivity ε, can be defined by:

www.manaraa.com

$$Ed = \frac{Qd}{\varepsilon A} \tag{2.12}$$

where E is the uniform magnitude of the electric field, d is the electrode-to-resonator gap distance and Q is the storage charge.

For a uniform electric field (ideal capacitor), the voltage between plates and the capacitance can be defined by:

$$Ed = V, \qquad where\ E = \frac{\varepsilon A}{Q} \tag{2.13}$$

$$C = \frac{Q}{V} \tag{2.14}$$

where C is the capacitance

The capacitance between the plates can be found by substituting equation (2.14) into (2.13):

$$C = \frac{\varepsilon A}{d} \tag{2.15}$$

Equation (2.15) defines the ideal capacitance between two parallel plates, this can be solved for if a DC bias is applied to the device. Since the main purpose is to actuate the device into resonance a time-variant electrostatic force needs to be generated. To be able to generate an electrostatic force, a time variant $V_i\, cos(\omega_n t)$ signal is applied to the input electrode which creates a time-variant parallel capacitor behavior that can be modeled by:

$$\frac{\partial C}{\partial x} = \frac{\partial Q}{\partial V} = \frac{\varepsilon A}{d^2} \tag{2.16}$$

Therefore, this generates a change in the kinetic energy of the resonator that can be modeled by:

$$F_{elect} = \frac{\partial \epsilon}{\partial x} = \frac{1}{2}\frac{\partial C}{\partial x}(V_p + V_i\, cos(\omega_n t))^2 \tag{2.17}$$

Assuming the response of the resonator is linear, the electrostatic force can be written as:

www.manaraa.com

$$F_{elect} = \frac{\varepsilon A}{d^2} V_p V_i \cos(\omega_n t) \tag{2.18}$$

Finally, to find the efficiency of the transduced signal at the point where input electrical signal is transformed into mechanical energy, the electromechanical coupling, η_{rec}, is calculated. Assuming minimum losses during the signal transduction from the input to the output electrodes, the electromechanical coupling coefficient between the output and input electrodes can be given by:

$$\frac{F_{elect}}{V_i \cos(\omega_n t)} = \frac{\varepsilon A}{d^2} V_p = \eta_{rec} \qquad where\ rec = 1,2 \tag{2.19}$$

2.8 Resonant Mode Shapes

When the time-varying force is generated on an elastic material that matches its natural resonant frequencies and mode shape, the device is driven into resonance. Depending on the frequency and the geometry of the elastic material, many resonant mode shapes can be achieved. For the purpose of this dissertation, only the in-plane or lateral/contour extensional modes have been explored. There are two fundamental relationships that need to be considered for each element in motion while in resonance: Newton's second law of motion and hook's law. To simplify this approach, a simple harmonic motion where all displacements are proportional to $\sin \omega_n t$ (where $\omega_n t = 2\pi$) in an isotropic cube will be considered [37]. Based on the vector displacements shown in Figure 2.7, the following relations can be derived:

$$A\nabla^2 u + B\frac{\partial \epsilon}{\partial x} = -\rho\omega_n^2 u(x) \tag{2.20}$$

$$A\nabla^2 v + B\frac{\partial \epsilon}{\partial y} = -\rho\omega_n^2 v(y) \tag{2.21}$$

$$A\nabla^2 w + B\frac{\partial \epsilon}{\partial z} = -\rho\omega_n^2 w(z) \tag{2.22}$$

www.manaraa.com

This yields three major equations that can be simplified into a more elegant form known as the wave equation:

$$(\nabla^2 + h^2)\epsilon = 0 \tag{2.23}$$

where,

$$\nabla^2 = \frac{\partial^2}{\partial x^2} + \frac{\partial^2}{\partial y^2} + \frac{\partial^2}{\partial z^2} \tag{2.24}$$

$$\epsilon = \frac{\partial u(x)}{\partial x} + \frac{\partial v(y)}{\partial y} + \frac{\partial w(z)}{\partial z} \tag{2.25}$$

$$h^2 = \frac{\rho \omega_n^2}{A + B} \tag{2.26}$$

where ρ and ω are the density of the structural material and the radial frequency accordingly. Also, A and B are given in terms of the fundamental elastic constants λ and μ with A= μ and B= λ+ μ.

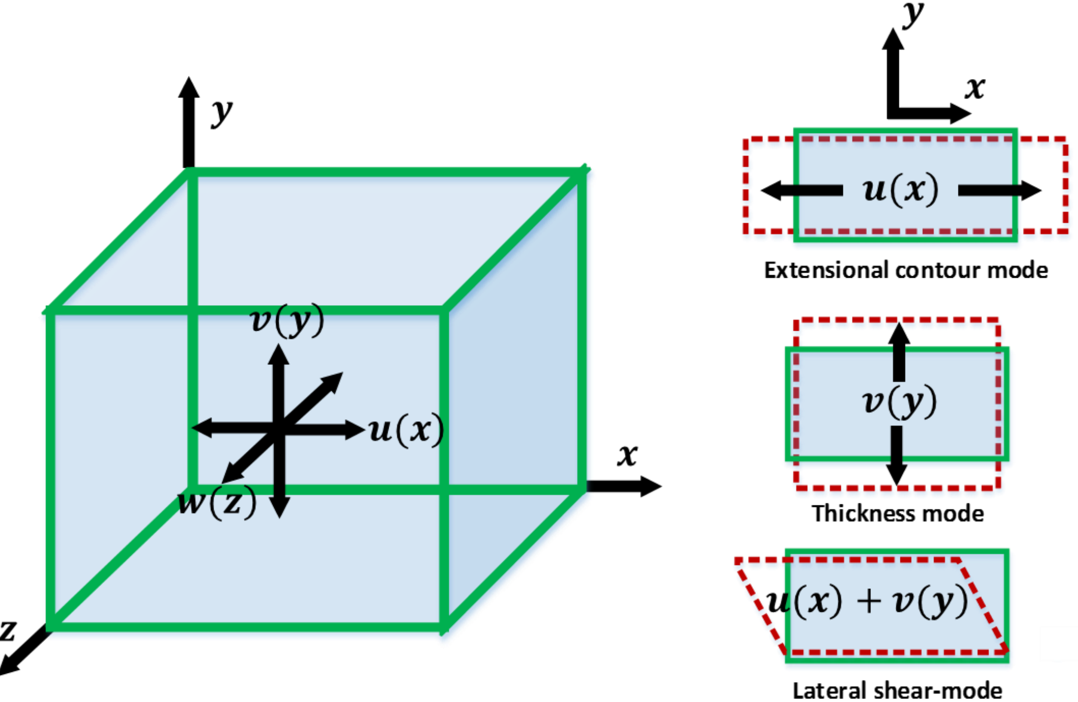

Figure 2.7 Illustration of an isotropic cube with three common resonant modes depicted.

www.manaraa.com

The solutions of these equations cover all possible resonant shapes which are infinite. In Figure 2.7, three fundamental resonant mode shapes are shown. To be able to obtain the lateral extensional (i.e., length or width extensional for square and rectangular membranes) or contour modes (i.e., fundamental extensional modes for disk devices) of vibration only the forces that generate stress is in the $u(x)$ displacement direction are considered, and the other displacements are neglected. Using direct substitution of equations (2.25) and (2.24) into equation (2.20), the x -wave equation can be derived as:

$$\frac{\partial^2 u}{\partial x^2} = -\frac{\rho}{E}\omega_n^2 u(x) \tag{2.27}$$

where E is the Young's modulus of the structural material.

A solution to the linear differential equation (2.27) that satisfies the boundary condition where the stress in the longitudinal direction equals zero at the end of the bar (i.e., x =0, x =l) is

$$u(x) = cosk_n x \tag{2.28}$$

Furthermore, the solution expressed in equation (2.28) shows that if $k = \frac{\pi}{l}$ or any digital number multiple of $\frac{\pi}{l}$, the extensional stress is reduced to zero at x=*l*; therefore,

$$k_n l = n\pi, n = 1,2,3 \ldots \tag{2.29}$$

where the relationship between k and ω can be found by substituting equation (2.29) into (2.27) as:

$$k_n = \omega\sqrt{\frac{\rho}{E}} \tag{2.30}$$

Substituting the values of k_n from equation (2.30) into (2.29) and (2.28) results in the resonance frequency and the displacement $u(x)$ for this system, accordingly:

www.manaraa.com

$$\omega_n = 2\pi f_n = \frac{n\pi}{l}\sqrt{\frac{E}{\rho}} \tag{2.31}$$

$$u(x) = \cos\omega_n\sqrt{\frac{\rho}{E}} \tag{2.32}$$

For circular disk contour modes, a similar approach can be derived to obtain the frequency equation given by:

$$\omega_{n,m} = 2\pi f_{n,m} = \frac{\alpha_{n,m}2\pi}{R_{disk}}\sqrt{\frac{E}{\rho}} \tag{2.33}$$

where R_{disk} is the radius of the disk and $\alpha_{n,m}$ is the frequency constant related to the mode(n, m).

Since circular disks can achieve non-axisymmetric resonant modes, a proper approximation to $\alpha_{n,m}$ is needed as a frequency scaling factor. The subscripts (n, m) denote the frequency modes where n is the circumferential order related to the nodal diameter and m is the radial harmonic of the disk at resonance [38]. The frequency scaling factor $\alpha_{n,m}$ for the first four disk fundamental contour modes assuming a Poisson ratio μ = 0.30 are: $\alpha_{2,1} = 0.272, \alpha_{R,1} = 0.342, \alpha_{3,1} = 0.418$, and $\alpha_{2,2} = 0.493$. This sequence was selected with the aid of COMSOL Multiphysics® modal simulation of a disk resonator as shown in Figure 3.1.

2.9 RF MEMS Resonator Equivalent Circuit Model

Despite of the geometry or resonant mode, vibrating systems can be represented by lumped mechanical and electrical models. As illustrated in Figure 2.8 (a), a point-mass system on a linear damper and a linear elastic spring can be used to model this. By applying an external actuation force, modal resonance can be achieved. Figure 2.8 (b) presents the analog equivalent lumped electrical system composed of an inductor, capacitor and resistor. The mass, elastic compliance and the damping of the mechanical domain is analogous to the inductance, capacitance and

www.manaraa.com

resistance of its electrical domain counterpart as shown in Table 2.3. These are essential system parameters because they're needed for the simulation of electrical resonator models derived from mechanical behavior models. In figure 2.8 (c), the electromechanical model that will be used throughout this dissertation is presented where the two transformers resents the isolation between the input and output electrodes. The capacitors C_{od} and C_{os} represent the driving and sensing metal pad's static capacitance between the electrodes and the device layer, accordingly. The in series LCR represents the behavior of the body of the resonator at resonance derived from Figure 2.8 (a) and (b). The substrate feed-through capacitance (C_f) accounts for the RF signal leakage between the input and output electrode through the substrate. The electromechanical coupling, η_{re}, represents the energy conversion efficiency between the electrical and mechanical domains of the sensor as described in section 2.6.

Table 2.3 Electromechanical Analogy between Electrical and Mechanical Parameters.

Mechanical Variable	⟺	Electrical Analog
Force ($\boldsymbol{F}$)	⟺	Voltage ($\boldsymbol{V}$)
Velocity ($\boldsymbol{v}$)	⟺	Current ($\boldsymbol{I}$)
Mass ($\boldsymbol{M_{re}}$)	⟺	Inductance ($\boldsymbol{L_m}$)
Compliance ($1/\boldsymbol{k_{re}}$)	⟺	Capacitance ($\boldsymbol{C_m}$)
Damping ($\boldsymbol{C_{re}}$)	⟺	Resistance ($\boldsymbol{R_m}$)

When disk or a square plate goes to resonance, not all of its mass is contributing to the kinetic energy equally. As illustrated in In Figure 2.9, a fraction of the total mass (M_{tot}) is

المنارة للاستشارات
www.manaraa.com

considered as the dynamic mass (M_{re}) and the rest is the static mass (M_{static}). This is a very important concept because as illustrated in equation (2.42), an important key parameter to find the sensitivity of a mass sensor is the equivalent mass M_{re}.

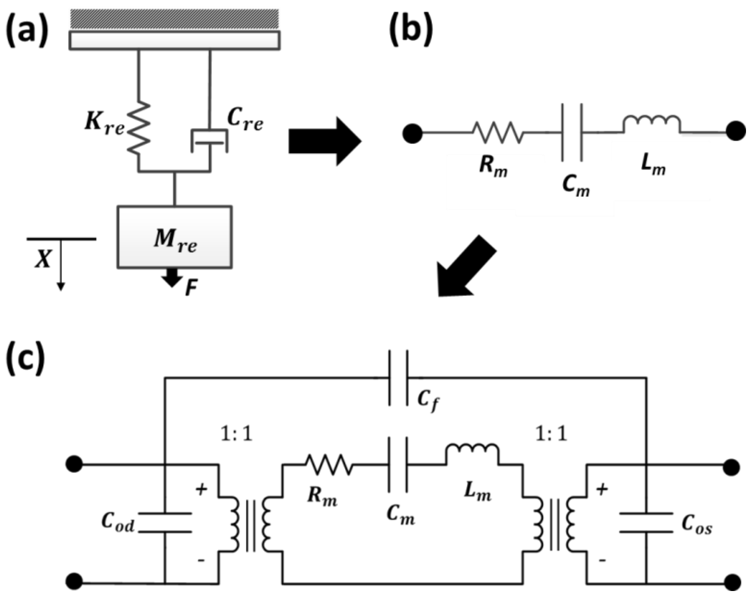

Figure 2.8 Illustration of the (a) mechanical and (b) electrical equivalent circuit models; and (c) a complete electromechanical model of the device.

The equation to find the M_{re} of disk and plate shaped resonators have been extensively derived for different resonant mode shapes for disk resonators using many approaches [39, 40]. However, the following approach was chosen because the resultant dynamic mass give us the best approximated results regardless of resonant mode shape. The M_{re} of a disk resonator at the point (R_{disk} ,θ) can be approximated by dividing the kinetic energy by one-half of the square velocity at a given maximal displacement point. For this device the dynamic mass can be approximated by:

$$M_{re} = \frac{KE_{tot}}{\frac{1}{2}v'(R_{disk}\,,\theta)^2} = \frac{2\pi\rho_n t_n \int_0^{R_{disk}} rJ_1^2\left(\frac{\omega_n}{C_{ql}}r\right)dr}{J_1^2\left(\frac{\omega_n}{C_{ql}}R_{disk}\right)} \tag{2.34}$$

where $J_1$is the Bessel function of the first kind [41].

www.manaraa.com

For plate resonators, a similar approach as the one taken for disk resonator can be performed to obtain the M_{re}, which yields the following [38]:

$$M_{re} = \frac{\rho_n t_n A}{2} = \frac{M_{tot}}{2} \tag{2.35}$$

where A is the area of the plate.

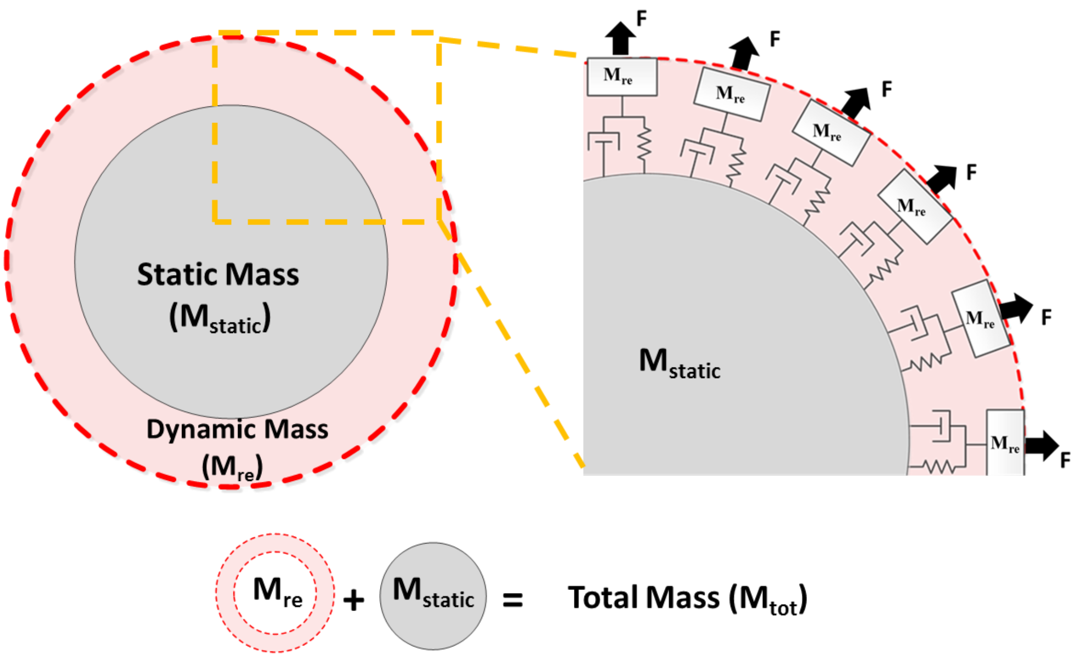

Figure 2.9 2D illustration of the dynamic mass of a 2nd contour mode disk resonator.

The equivalent stiffness, K_{re}, and damping, C_{re}, of the system at resonance can be then obtained by:

$$K_{re} = M_{re}\omega_o^2 \tag{2.36}$$

$$C_{re} = \frac{\omega_n M_{re}}{Q} \tag{2.37}$$

From Figure 2.7(C), the equivalent lumped-element circuit parameters can then be derived as follows:

www.manaraa.com

$$L_m = \frac{M_{re}}{\eta_{rec,p}^2} \tag{2.38}$$

$$C_m = \frac{\eta_{rec,p}^2}{K_r} \tag{2.39}$$

$$R_m = \frac{C_{re}}{\eta_{rec,p}^2} \tag{2.40}$$

To calculate the platform rigid dynamic of a plate resonator equations (2.38) to (2.40) can be used because the resonant dynamics are the same, with exception of M_{re}.

2.10 Sensitivity and Limit of Detection (LOD) of RF MEMS Resonators

The limit of detection of a resonant sensor can be found by the device signal to noise ratio:

$$LOD = \frac{S}{\Delta f_{noise}} \tag{2.41}$$

where S and Δf_{noise} are the sensitivity and the short-term noise of the sensor.

When an added mass is much smaller than the M_{re}, the sensitivity and resolution of a MEMS resonator can be approximated by:

$$S = \frac{\Delta f}{\Delta m} \approx \frac{f_{n,m}}{2M_{re}} \tag{2.42}$$

where Δf is the measurable frequency shift, Δm is the change of mass, $f_{n,m}$ is the resonance at the contour or length extensional resonant mode, and M_{re} is the dynamic mass of the resonator.

The mass resolution of the device can be obtained by measuring the short-term resolution and the slope of the phase at resonance

$$\Delta f_{noise} = \left(\frac{\partial \varphi}{\partial f}|_{f_0}\right)^{-1} \Delta\varphi \tag{2.43}$$

where $\frac{\partial \phi}{\partial f}|_{f_0}$ is the slope of the phase at resonance and $\Delta\varphi$ is the zero span phase noise.

www.manaraa.com

CHAPTER 3 CAPACITIVE RF MEMS RESONATORS

Capacitively-transduced MEMS resonators are one of the most attracting mass sensing technologies available because it has many great advantages. Minimum air damping losses is the greatest advantage of these devices, therefore they can detect diminutive mass changes in both vacuum and air. It has been reported that these devices can achieve resonant frequencies from MHz to GHz with Q factors exceeding 5,000 [42-44].In order to achieve high resonant frequencies, the resonant body needs to be scaled down to very sizes (usually in the micron range) as described in equations (2.31) and (2.33). This process can be achieved using standard MEMS fabrication techniques. One more benefit of scaling down the resonant body is that a smaller M_{re} can be achieved as demonstrated in equation (2.34). These parameters are very important while determining the sensitivity and resolution of the device. However, the trade-off of scaling down the resonant body is the reduction of the electrode overlapping area which increases the motional impedance R_m of the device. This effect can be observed by substituting equation (2.19) into (2.40):

$$R_m = \frac{K_{re}}{\omega_o Q {V_p}^2} \cdot \frac{{d_o}^4}{{\varepsilon_r}^2 {\varepsilon_o}^2 {A_o}^2} \tag{3.1}$$

where d_o is the electrode-to-resonator air-gap distance; ε_r is the relative permittivity of air; ε_o is the permittivity in vacuum; A_o is the electrode-to-resonator overlap area.

Commonly reported motional impedance values of MEMS capacitively-transduced resonators range from hundreds of kΩ to few MΩ. This values are very large compared to the RF industry standard of 50-377Ω. Therefore, they cannot be easily integrated with commercially

www.manaraa.com

available technology without an amplification step. To amplify the signal additional components such as trans-impedance amplifiers are needed. Usually, it is not a good practice to integrate too many off-chip components into one device because that introduces additional noise. In addition, the overall device assembly becomes more expensive. Therefore, this chapter covers a few practical approaches that can be applied to reduce the motional resistance.

3.1 Resonant Frequency and Mode Shape Selection

For resonant frequency and mode shape selection, electrodes and anchors needs to be strategically designed. As previously mentioned in section 2.8, an elastic body has infinite number of resonant modes. In this dissertation, only the extensional lateral and contour modes have been studied. To be able to discriminately select these modes, a FEM modal analysis using COMSOL Multiphysics® is performed as shown in Figure 3.1. The FEM model consists of a suspended membrane composed of the intended structural material.

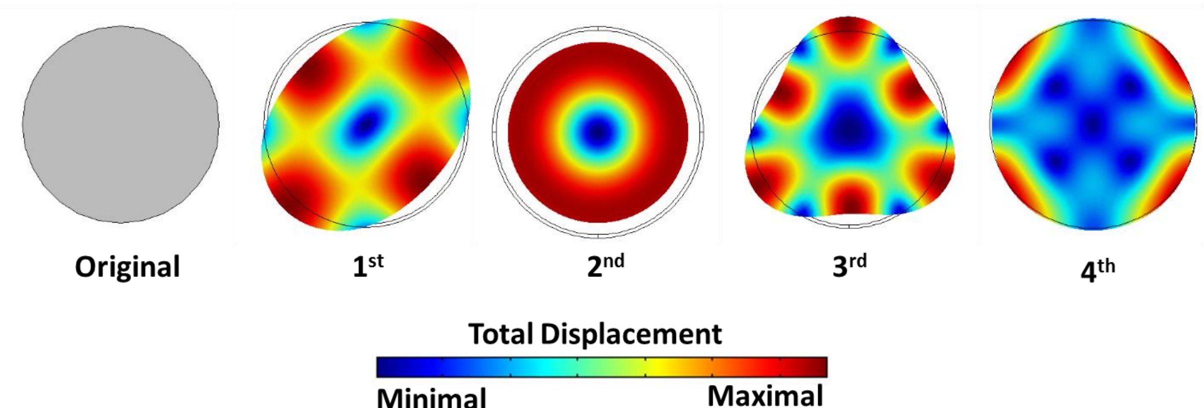

Figure 3.1 FEM nodal analysis using COMSOL Multiphysics® of a circular membrane vibrating at the first 4 contour modes.

To be able to achieve the intended electrode design the maximal displacement area needs to be identified. As seen is Figure 3.1 the maximal displacement (red colored) area occurs on

www.manaraa.com

specific areas of the resonant body. This red colored area is also where the maximum mechanical deformation occurs.

As discussed in section 2.7, the maximal displacement determines where the maximum variations of the gap distance is more variable at the time of resonance, thus generating the maximum energy transfer. A strategic electrode design that matches the maximal displacement areas can drive and detect the energy of the intended resonant mode more efficiently. Figure 3.2 shows two design approaches to best match the 1st and 2nd disk contour resonant modes.

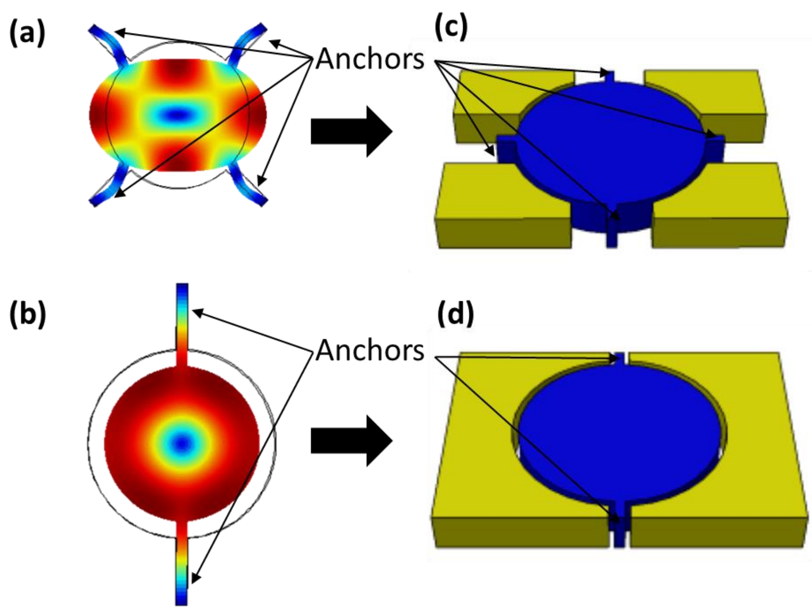

Figure 3.2 Electrode and anchor design approaches: (a) 1st contour resonant mode characteristics and anchor location used to create a (c) 3D device matching model, (b) 2st contour resonant mode characteristics and anchor location used to create a (d) 3D device matching model.

One more important parameter is the placement of a set of structures known as the anchors. These structures connect the free-standing membrane to the device layer. The placement and size are very crucial for device performance and frequency discrimination. It is ideal to make these structures as small as possible because they introduce a large amount of damping into the system [45]. Also, they can be strategically design to damp unwanted spurious resonant frequencies. As

www.manaraa.com

opposite to the electrode design, anchors should be placed at the minimal displacement areas of the targeted resonant mode shape. As shown in Figure 3.2 (a), the anchors are placed in a way that only the 1st contour mode can be obtained, while damping out most of the other resonant modes in Figure 3.1 except the 4th contour mode. The anchor design shown in Figure 3.2 (b) is not ideal, because the anchors interfere with the targeted 2nd contour resonant mode. However, its large electrode overlapping area makes it as an ideal design that can excite most contour resonant modes as shown in Figure 3.1. It is important to note that the crystal orientation also plays a very important role the anchor design. In-depth analysis of electrode and anchor design for targeted resonant modes using capacitive devices have been well investigated [39].

3.2 Oxidation Air-gap Reduction Fabrication Process

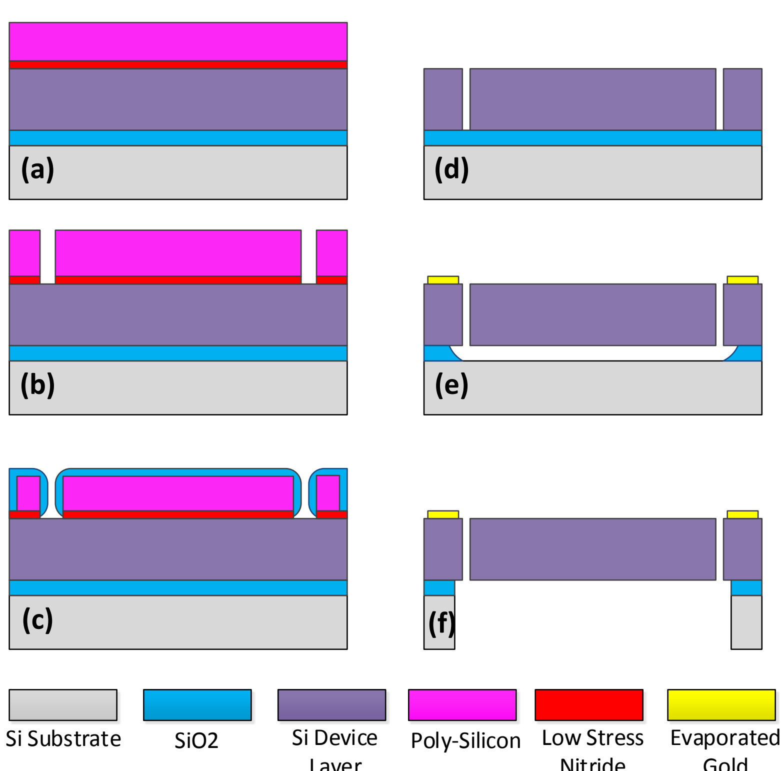

Figure 3.3 Oxidation air-gap reduction fabrication process flow: (a) PECVD and LPCVD deposition of SiN and Polysilicon accordingly, (b) HAR DRIE of polysilicon/SiN hard mask, (c) 1 μm-thick furnace wet oxidation of the hard mask, (d) HAR DRIE of Si and hard mask removal, (d) gold contact pads and release, (d) backside release via HAR DRIE of Si.

www.manaraa.com

According to Equation (3.1), one practical way to reduce the motional resistance of the device is by reducing the electrode-to-resonator air-gap distance. The fabrication of a capacitive-transduced resonator with a novel oxidation defined air-gap technique is illustrated in this section. The MEMS resonating sensing platforms have been microfabricated using silicon-on-insulator (SOI) substrates with highly doped 5 μm-thick device layer with resistivity ranging from 0.005 Ω cm to 0.020 Ω cm and a 1 μm-thick buried oxide (BOX) layer.

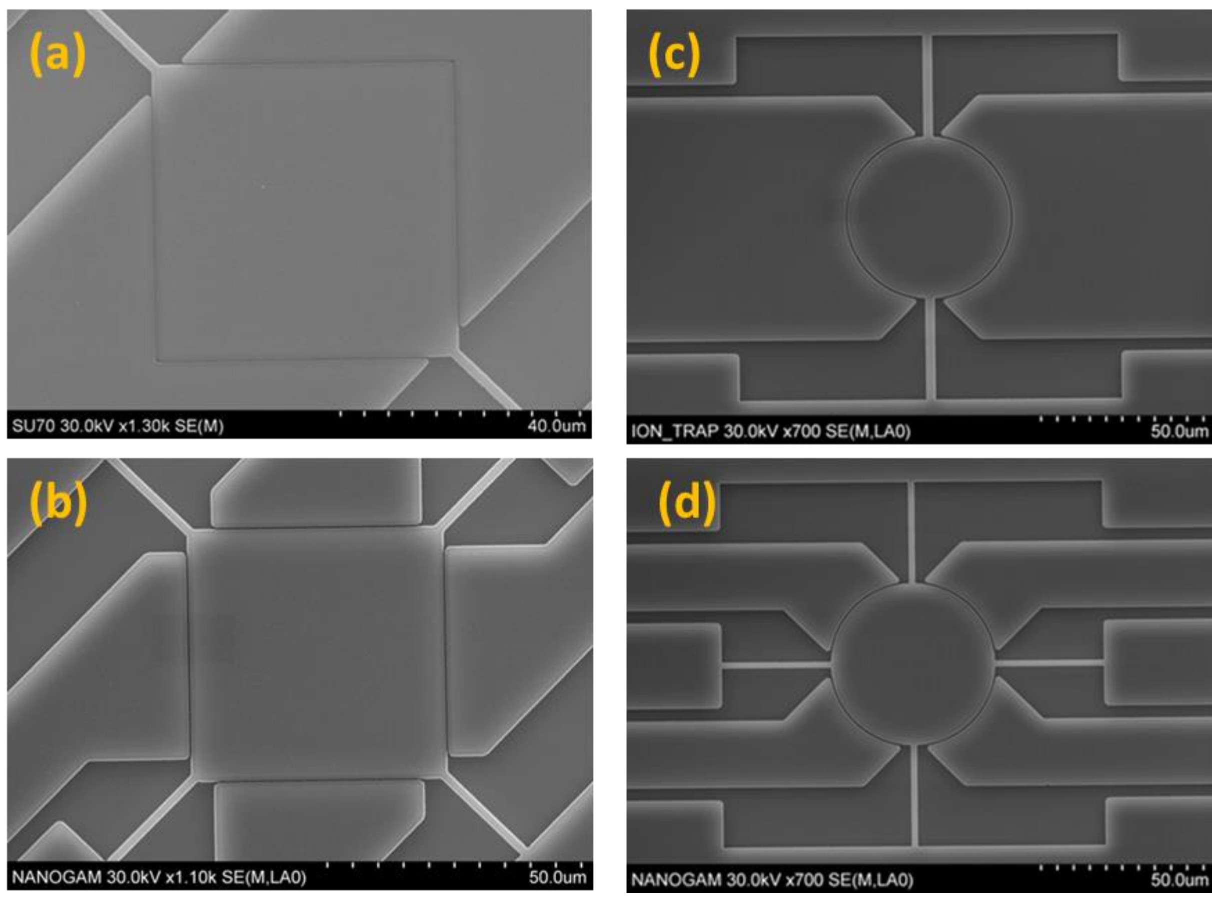

Figure 3.4 SEM of fabricated devices: 2st extensional contour and 1st extensional contour designs for (a)(c) square and (b)(d) circular membranes accordingly.

Figure 3.3 summarizes the fabrication process flow that consists of three photolithography steps. The fabrication process starts with a deposition of a 100 nm-thick plasma-enhanced chemical vapor deposition (PECVD) stoichiometric silicon nitride that serves as an oxygen

www.manaraa.com

diffusion barrier layer. This is followed by a 2µm-thick polysilicon low pressure chemical vapor deposition (LPCVD) as the material of choice for the hard mask as seen in Figure 3.3 (a). Thereafter, a lithography step using a 1 µm- thin AZ1512 photoresist layer is performed, followed by a short high-aspect-ratio deep reactive ion etching (HAR DRIE) of the silicon device layer using a modified Bosch process (see section 3.3) as seen in Figure 3.3 (b). This process yields an electrode-to-resonator gap spacing of 1 µm. Next, a 1 µm-thick SiO_2 layer is grown to decrease the gap spacing down to ~300 nm as seen in Figure 3.3 (c), which is followed by a short modified Bosch silicon HAR DRIE etch to transfer the nano-gap to the device layer in the SOI wafer device layer as seen in Figure 3.3 (d). A lithography step using AZ12XT, followed by 50 nm Cr / 200 nm Au using an ebeam evaporator defines the gold contact pads. Finally, a 5.5 µm- thick AZ12XT is used to define the etch window through which the resonator body can be released by etching the buried oxide layer using a 6:1 buffer-oxide-etch (BOE) as seen in Figure 3.3 (e). As an alternative approach, backside release can be carried out to further improve the processing yield and reduce the device cross-talk. This can be achieved by a photolithography step using a 10 µm-thick AZ12XT photoresist which is patterned on the backside of the wafer. Then a HAR DRIE dry etch of Si defined the release holes. To suspend the devices, the BOX layer can be readily etched away as shown in Figure 3.3 (f) by dipping the processed wafer into a 6:1 BOE solution for a few minutes. For the oxidation air-gap reduction process, four designs were fabricated as shown in Figure 3.4 following the design analysis in section 3.1. The initial air-gap of 1 µm was reduced to ~300 nm. In Figure 3.5, a 1st contour square mode design electrode-to-resonator air-gap was reduced from 1 µm to 251nm. This is anticipated to lead to a significant reduction of R_m, which varies inversely proportional to d_0^4 according to equation (3.1).

www.manaraa.com

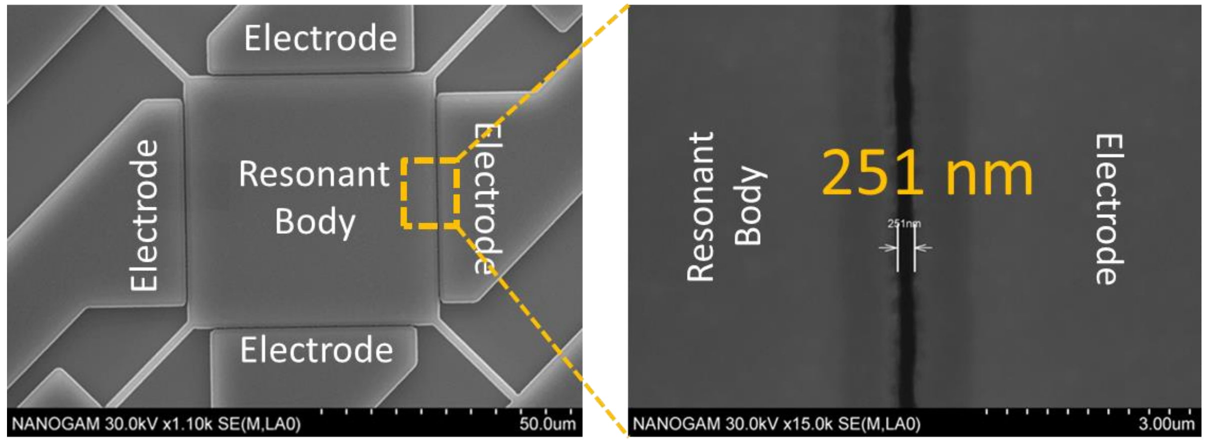

Figure 3.5 SEM image of air-gap reduction results after 1 μm wet furnace oxidation.

3.3 DRIE Characterization

One of the biggest challenges of fabricating small capacitive gaps is to transfer the nano-meter electrode-to-resonator gap spacing patterned precisely into the device layer. The DRIE is a great tool that was designed for straight sidewall transfer especially for the formation of high-aspect ratio structures (HARS) in silicon. The most common method of forming straight sidewalls using the DRIE is a time multiplex deep etching technique (TMDE) known as the Bosch process. It is widely used because it has good material selectivity, CMOS compatibility, high etch rate, and it is also a highly anisotropic process. SF_6 and CF_4 are the two common etch chemistries in silicon HAR DRIE process. For both of them, a fluorine free radical is released after either gas has been dissociated in plasma:

$$SF_6 \rightarrow SF_5^* + F \quad or \quad CF_4 \rightarrow CF_3^* + F$$

Silicon etch rate depends on both the number of free F radicals and the area of exposed silicon. Fluorine silicon etch at temperatures higher than -15°C is known be isotropic; therefore, there is a need of extra steps that requires a specialized chemistry to protect the sidewalls. In most cases, C_4H_8 is used to protect the sidewalls because its product, -(CF2)-, reacts with silicon to form a Teflon-like protection layer that can be removed with oxygen plasma. The cycling of SF_6 and

www.manaraa.com

C_4F_8 is what makes the HAR DRIE Bosch dry etch an anisotropic process as illustrated in Figure 3.6.

As observed in Figure 3.6 (d), the sidewall roughness generated after a Bosch etch run is called scalloping. There are two types of scalloping profiles: scallop depth and length. Scallop length is generated by free fluorine radicals that remove Si atoms vertically; therefore, it can be minimized by either reducing the source power, SF_6 gas flow and/or pulse time. The effect of scallop length is rather positive because the larger it is the faster is the etch rate. On the other hand, scallop depth is generated by the isotropic nature of fluorine radicals at temperatures higher than -20°C. To be able to minimize scalloping, there are two commercially available solutions: cryogenic and fast gas switching Si etching systems.

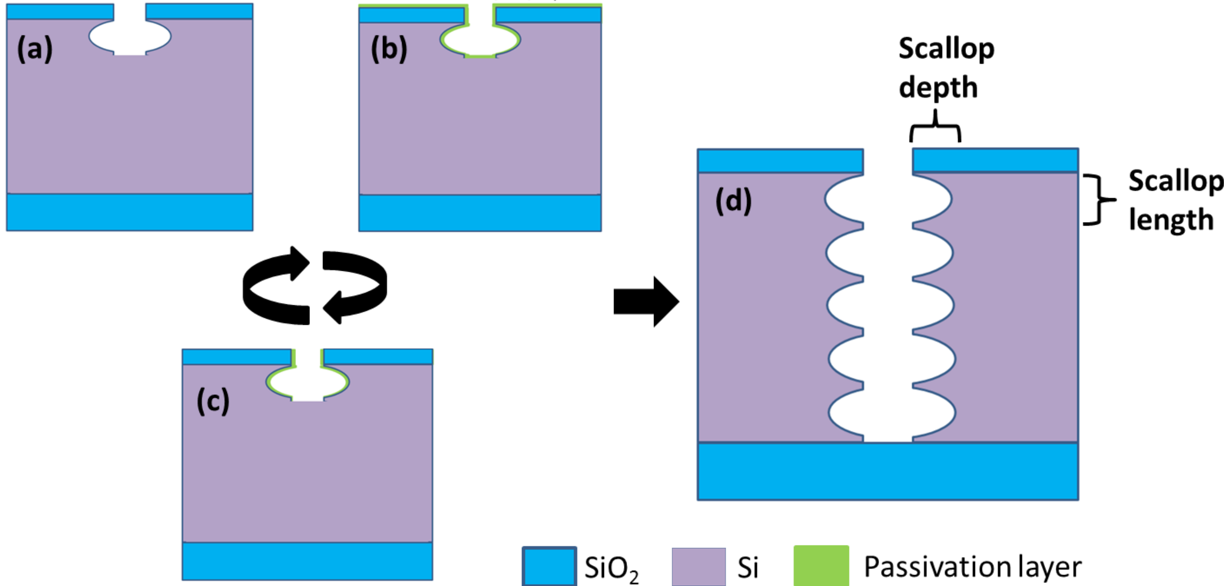

Figure 3.6 (a) Fluorine Si isotropic etch; (b) Passivation step where a Teflon-like material conformal deposition for sidewall protection; (c) De-passivation step horizontal surface removal of Teflon-like material after O_2 plasma at low temperatures; (d) Bosch sidewall roughness profile.

Cryogenic Si etching systems uses a continuous gas flow at very low temperatures (less than -100°C) where plasma reacts with SF_6 generating fluorine free radicals. The highlight of this

www.manaraa.com

system is that it doesn't rely on gas pulsing cycles to obtain an anisotropic profile but rather is the anisotropic nature that fluorine at low temperatures; therefore, no sidewall roughness is left. In the other hand, fast gas switching systems uses special fabricated valves that allows a rapid (typically milliseconds) pulsating flow of SF_6 or CH_4 and C_4H_8/O_2 generating minimum sidewall roughness with scallop depth of 10-30 nm.

Table 3.1 Standard Bosch High-aspect Silicon Dry Etching Recipe used for Alcatel AMS 100 Inductively Couples Plasma (ICP) Systems.

Temperature (° C)	Cycle				Source power (w)
	Etching		Passivation		
	SF_6 flow rate (sccm)	SF_6 pulse time (s)	C_4F_4/O_2 flow rate (sccm)	C_4F_4/O_2 pulse time (s)	
-15	300	3	200/20	1.4	2400

The system used for the fabrication of these devices is an Alcatel AMS 100 DRIE, which is conventional SF_6 inductively coupled plasma (ICP) system that generates the following roughness profile: scallop length of 830 nm and scallop depth of 274 nm. This values are very insignificant while dealing with larger structures and passive devices. But it significantly affects the devices whose performance is largely based upon the size of the electrical gap as capacitive transduced resonators.

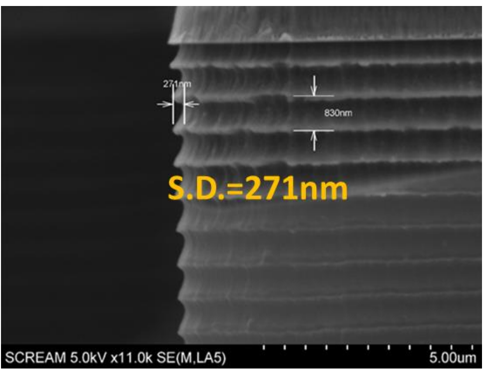

Figure 3.7 SEM of a sidewall roughness profile after a standard Bosch recipe DRIE silicon etch run in an Alcatel AMS 100 ICP System with a scalloping depth (S.D.) of 271nm.

www.manaraa.com

As illustrated in Figure 3.8, it can be observed that using a profile similar to the one shown in Figure 3.7, significantly changes are anticipated in the device electrical characteristics. As previously covered, the aim of the first generation devices is to have capacitive gap of ~300 nm.

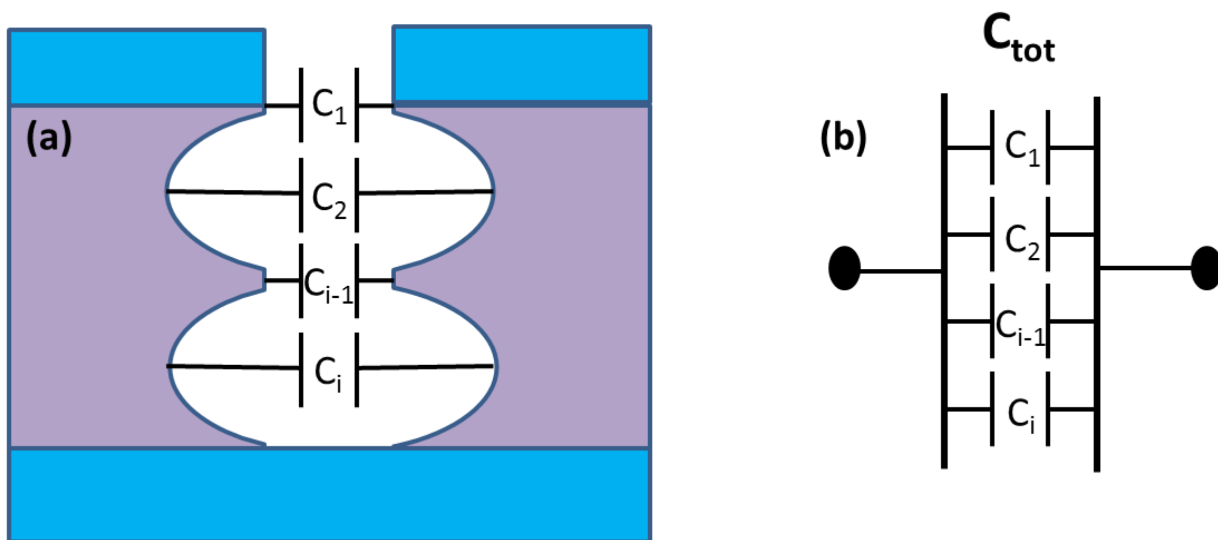

Figure 3.8 2D illustration of the capacitance behavior (a) inside of an air-gap with a known distance and the (b) its equivalent circuit model.

From the achieved roughness profile as shown in Figure 3.7 and using equation (3.2), the final sidewall roughness will be about 600 nm or larger. For this case, a 300 nm intended profile will ultimately behave as a 900 nm capacitive gap. In electrical means, the R_m will increase as ${d_o}^4$ according to Equation (3.1).

$$C_{tot} = \frac{C_1 + C_2 + C_{i-1} + C_i}{n} = \frac{1}{n}\sum_{i=1}^{n} C_i \qquad (3.2)$$

In order to reduce the side wall roughness of the Si Bosch etching profile generated by the Alcatel AMS 100 ICP system, the process parameters need to be modified. The thickness of the deposited polymer (passivation layer) was the first parameter to be studied. After modifying the C_4H_8 pulse time while maintaining the SF_6 pulse time constant at -15°C, very little improvement to sidewall roughness can be observed. However, increasing the pulse time does have a negative

www.manaraa.com

effect because the excess of polymer deposition cannot be fully etched away by oxygen plasma for a successfully de-passivation step. Therefore, grassy looking profiles are achieved as the one seen in Figure 3.9.

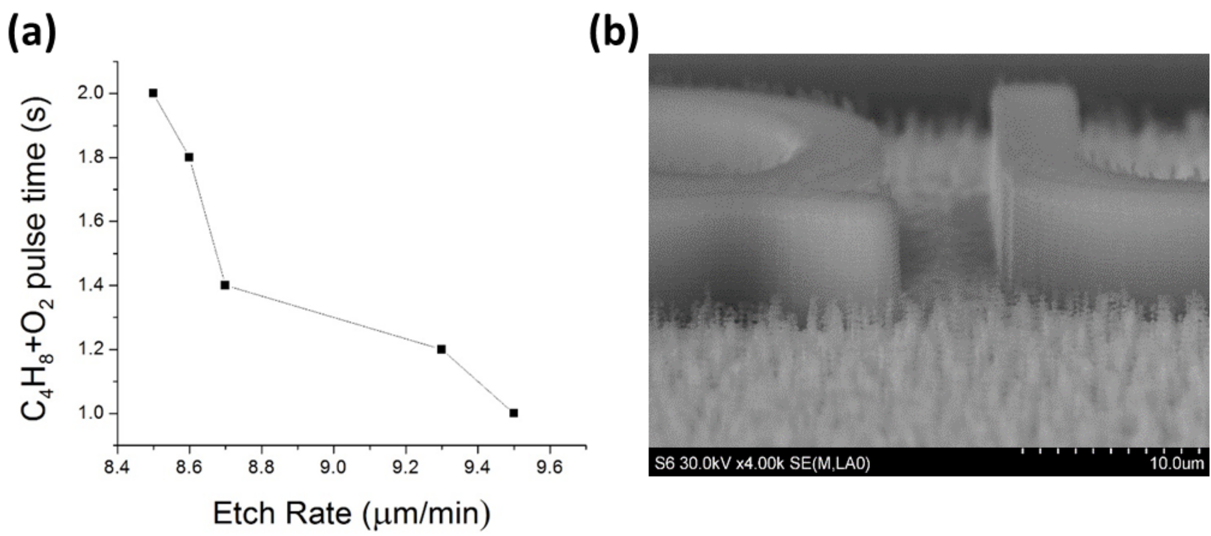

Figure 3.9 DRIE Bosch etch profile after the passivation values were altered: (a) Etch rate vs. pulse time graph of altered values and (b) the SEM image of the modified etch profile.

The next parameter to study is the SF_6 pulse time. As previously mentioned, there are commercial available ICP systems that use lower pulse times to reduce the sidewall roughness of the Si Bosch dry etch process. However, it is understood that all ICP dry etching systems are designed with different limitations and it is imperative not to change too many of the working parameters such as source power, gas pressures, and substrate holder position to prevent damage to the system.

It was found that by changing the SF_6 pulse time and keeping all the other parameters the same as seen in Table 3.1 both the scallop length and depth are affected. For this study, SF_6 pulsating values ranging from 3s to 2s were considered because values greater than 3s result in a significant increase in sidewall roughness. Also, values lower than 2s result in a significant decrease of the Bosch etching anisotropic profile. As shown in Figure 3.10, when the SF_6 pulse

www.manaraa.com

time is reduced to 2s while maintaining the substrate holder temperature constant at -15°C, a significant decrease of the Si isotropic etching profile is observed. This results in a substantial drop in the scallop depth size from 280 nm down to 84 nm as observed in Figure 3.11 (b) and Figure 3.10 (b) while maintaining its intended anisotropic profile as seen in Figure 3.11 (a). Reducing the SF_6 also reduces the etch rate as presented in Figure 3.10 (a), but not in an alarming rate that could compromise the etch profile.

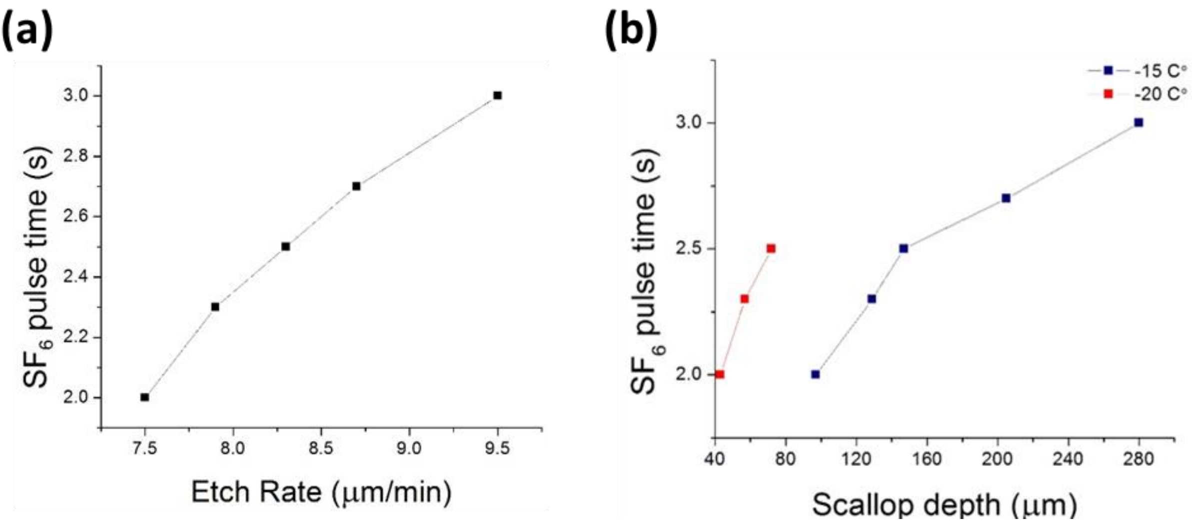

Figure 3.10 SF_6 pulse modified profile data: (a) graph of modified SF_6 pulse vs. Si etch rate and (b) graph of modified SF_6 pulse vs. scallop depth.

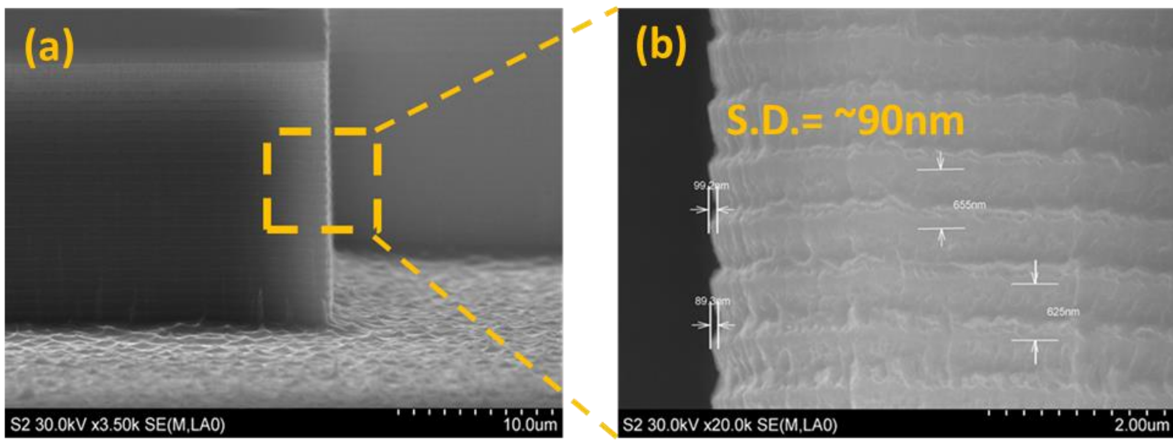

Figure 3.11 SEM images of SF_6 pulse modified sidewall profile at -15°C: (a) overview of the anisotropic sidewall profile, and (b) close-up image of the scalloping depth (S.D.) size.

www.manaraa.com

The substrate holder temperature was lowered to -20°C (the lowest a standard Alcatel AMS 100 DRIE system can achieve) to study the effects of Bosch SF_6 Si dry etching at lower temperatures. It has been well documented that at lower temperatures fluorine radicals are more directional for etching Si [46]. As shown in Figure 3.12(b) and Figure 3.10(b), it can be observed that decreasing the temperature from -15 C° down to -20 C° reduces the scallop depth from ~84nm down to ~42nm. Also, the overall sidewall roughness is smoother and yet very vertical at lower temperature as shown in Figure 3.12(a).

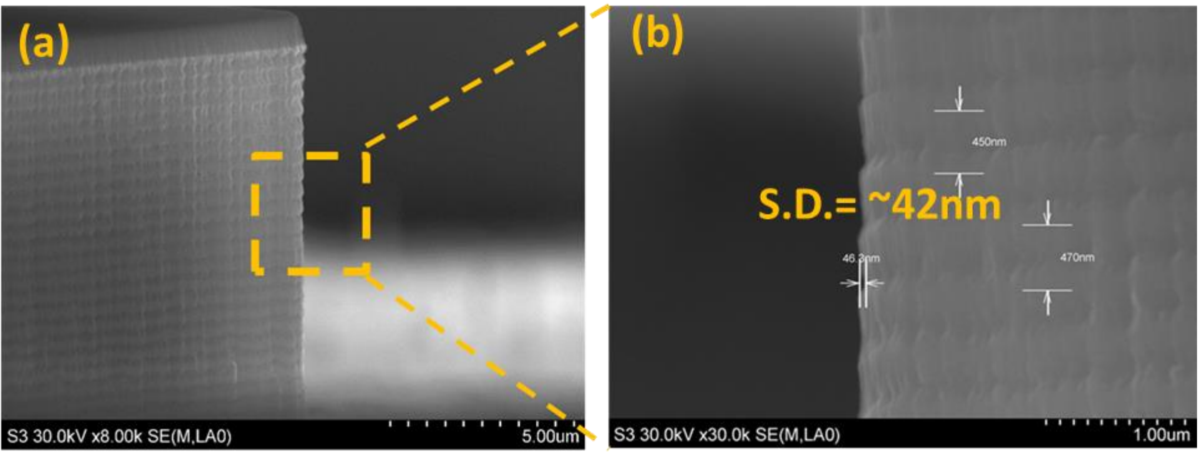

Figure 3.12 SEM images of SF_6 pulse modified sidewall profile at -20 C°: (a) overview of the sidewall anisotropic profile and (b) close-up image of the scalloping depth (S.D.) size.

From this study it can be concluded that smooth sidewalls can be achieved even with standard DRIE systems by modifying both SF_6 pulse time and lowering the substrate holder temperature. By revisiting equation (3.2), it can be seen that now the intended 300 nm will behave more like a ~385 nm capacitive gap after the customized Si Bosch recipe is applied compared to ~900nm from the original default recipe.

3.4 Thin Sacrificial Layer Air-gap Reduction Fabrication Process

The fabrication approach for this devices was developed to reduce electrode-to-resonator air-gap distance, d_o, through the employment of a sacrificial 100nm ALD deposited layer. Also,

www.manaraa.com

backside release was also implemented to minimize the device the feed-through capacitance, C_f. The devices were microfabricated using silicon-on-insulator (SOI) substrates with highly doped 5 μm thick device layer resistivity ranging from 0.005 Ω cm to 0.020 Ω cm and a 1 μm-thick buried oxide (BOX) layer as seen in Figure 3.11(a).

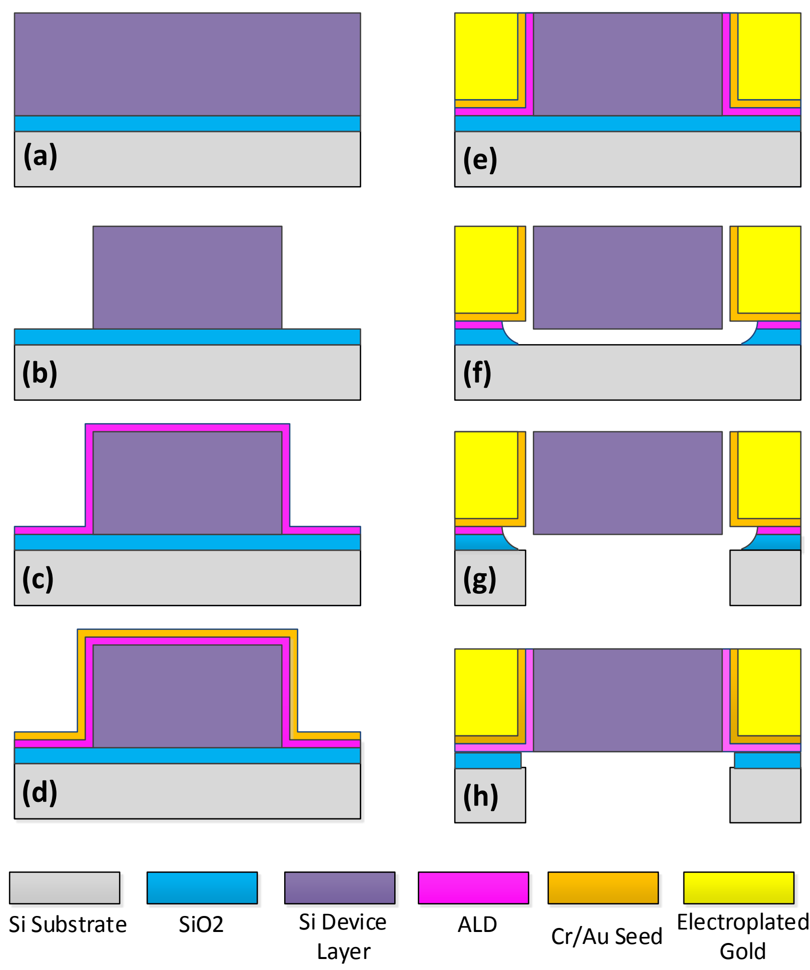

Figure 3.13 Step-by-step illustration of the thin sacrificial layer air-gap reduction fabrication process flow:(a) a SOI wafer as the starting substrate; (b) HAR DRIE Si resonator etch; (c) 100nm of Al_3O_2 ALD layer; (d) Au/Cr seed layer; (e) Gold electroplated electrodes; (f) front-side B.O.E release; (g) backside HR DRIE release followed by B.O.E; (h) optional solid gap profile by HR DRIE backside etch followed by SiO_2 DRIE release dry etch.

Figure 3.13 summarizes the microfabrication process flow that consists of four photolithography steps. The fabrication process begins with a photolithography step using a 1 μm AZ1512, followed by 6 μm modified HAR DRIE Bosch etching recipe (as described in section

المنارة للاستشارات
www.manaraa.com

3.3) to define the body of the resonator. Next, a 100nm gap spacing layer was deposited using an atomic layer deposition (ALD) process to define the capacitive gap as seen in Figure 3.13 (c). Then, a thin evaporated 20nm Cr/100nm Au seed layer was deposited with an e-beam evaporator as the conductive electroplating layer as seen in Figure 3.13 (d). Next, a 30 µm-thick layer of AZ12XT is spun on the wafer, followed by a time-controlled oxygen ashing step using ICP etcher to selectively remove the conductive seed layer on top of the resonators. This process is known as etchback. Then, the exposed Cr/Au seed is removed via wet chemistry to prevent electroplating on top of the devices that could lead to device electrode-to-electrode shortage. Next, a photolithography step consisting of a 5.5 µm-thick AZ4620 is performed to form the electroplating mold that defines the shape of the electrodes, followed by a 4.5 µm gold electroplating step. Then, the photoresist electroplating mold is removed via AZ400T resist stripper and oxygen descum as seen in Figure 3.13 (e). This is followed by a wet chemistry removal of the Cr/Au seeding layer.

There are three different techniques to release this device. As illustrated in Figure 3.13 (f), the first technique consists of a photolithography step to pattern the release opening using AZ4620 followed by a 4 hours of BOE wet release. As illustrated in Figure 3.13 (g), the second technique consist of a photolithography step to pattern the backside release openings with AZ4620 followed by a HAR DRIE Si etch. Then the devices are dip in to BOE for 10 minutes to remove the BOX and ALD layer. As illustrated in Figure 3.13(f), an optional step of creating solid gaps can be achieved by through HAR DRIE Si followed by DRIE SiO_2 dry release etch. As shown in Figure 3.17, front-released devices yielded ~100 nm gaps as seen in Figure 3.14. Also, backside released devices were successfully released as shown in Figure 3.15 with measured capacitive gaps of ~290 nm. The intended gaps for both processes were 100 nm; however, backside release structures, especially the gold electrodes suffer from stress effects occurring during the BOE wet release.

www.manaraa.com

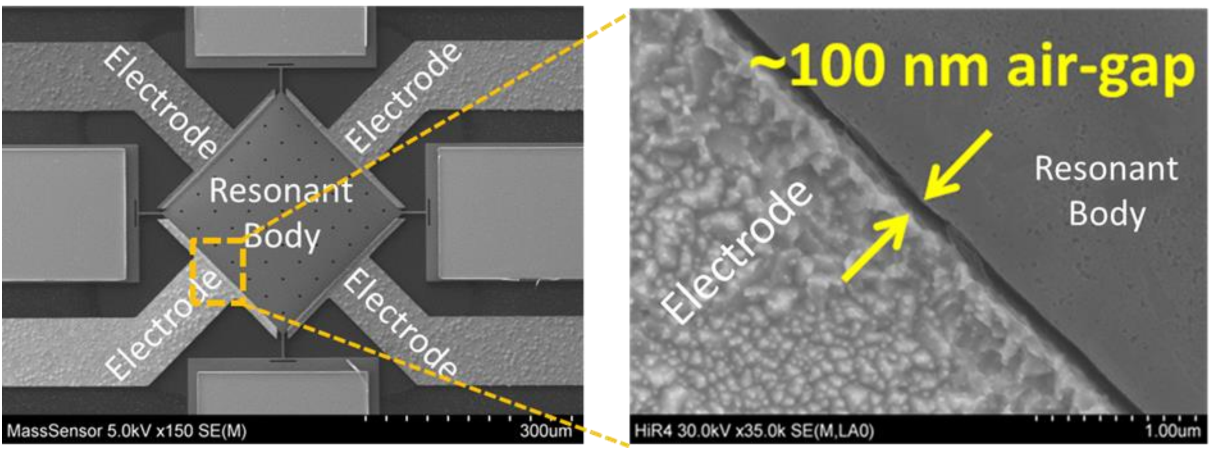

Figure 3.14 SEM of front-side released device with 100nm air gap.

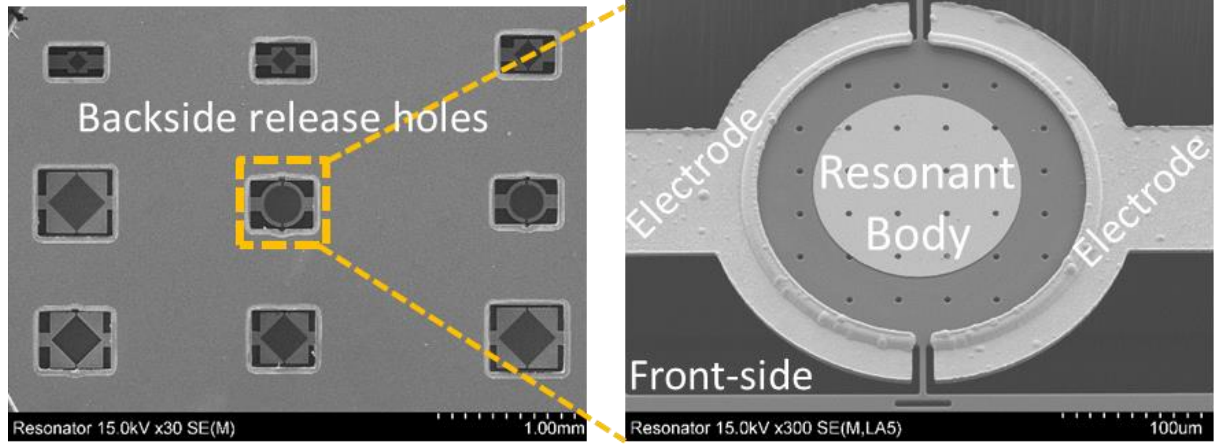

Figure 3.15 SEM of suspended device after backside release of HAR DRIE Si etch.

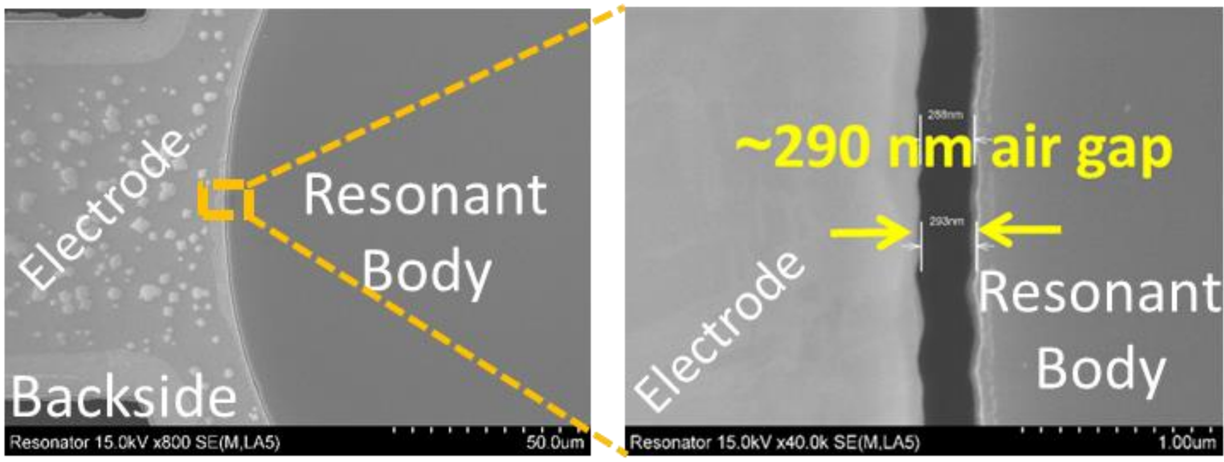

Figure 3.16 SEM of suspended device after backside release with a 290nm air-gap capacitive gap.

www.manaraa.com

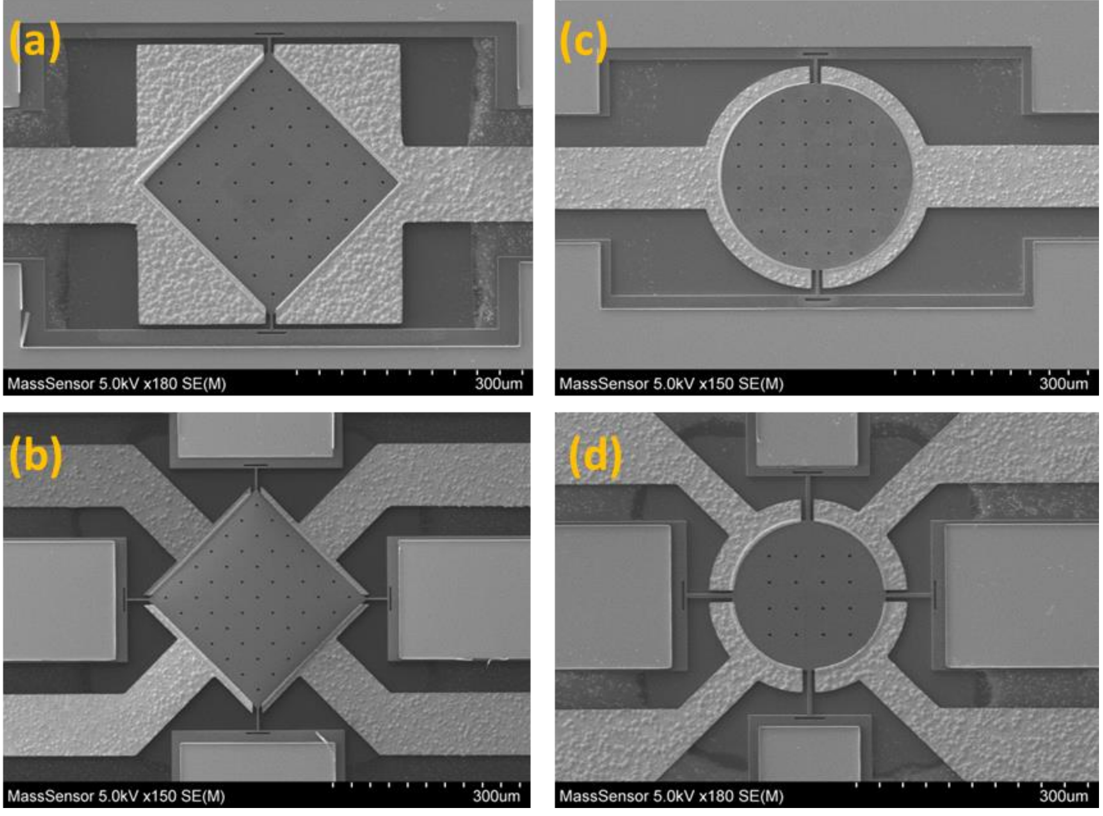

Figure 3.17 SEM of front-side fabricated devices with circular and square design for 1st contour and lateral resonant mode.

3.5 RF Test Results

Capacitive devices were tested using the test set-up illustrated in Figure 3.18. It was found that the devices were shorting out after a biasing voltage of 5 DC was applied as shown in Figure 3.20. This implies that the capacitive gaps were not fully released or/and that particles are finding their way in to the air gap. A pull-in voltage test that consisted of a voltage sweep generator confirms that the fabricated devices were shorting out after 5V as shown in Figure 3.19 (c). a few fully release air-gaps were measured using this method, the ~100 nm and ~250 nm air-gaps were shorting at 38.7V and 73.9V, respectively, as shown in Figure 3.19 (a) and (b) . This implies that the nano-meter capacitive gaps have unwanted particles shorting them at lower voltages. This often

www.manaraa.com

happens when the devices are dried using solvent under atmosphere pressures. The particles in the solvent tend to be drawn into the air gaps by the capillary forces [47].

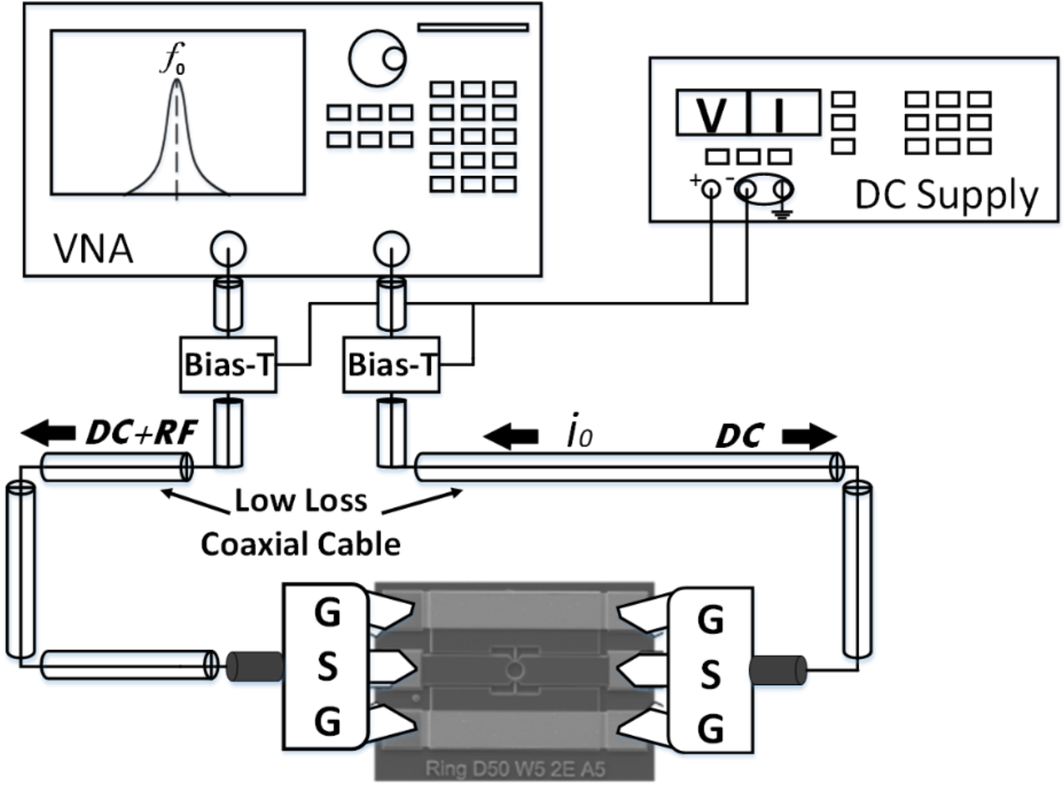

Figure 3.18 Illustration of RF test set-up for capacitive devices.

The only solution to this problem is to use a critical CO_2 drying system right after BOE wet oxide release. Testing the devices with such low breakdown voltages limits the maximum applied DC bias to ~5V. This effect can be observed in Figure 3.21(a), where a 50 μm-radius disk resonator was tested using a bias voltage of 5V and the signal was too weak to be detected. If the gaps were fully clean, then a bias voltage of 25V or higher can be applied. As shown in Figure 3.21(b), applying a 25v biasing voltage will reduce the motional resistance from 0.565 MΩ to 26.6 kΩ. Thus, taking into account taking an estimated C_f of 30 *f*F from the measure spectrum, a DC bias of 25v is sufficient to observe the resonance signal. The simulated values were obtained as described in section 2.9 for a Si 50 μm-radius disk resonating at 45 MHz with a Q factor of 10,000.

www.manaraa.com

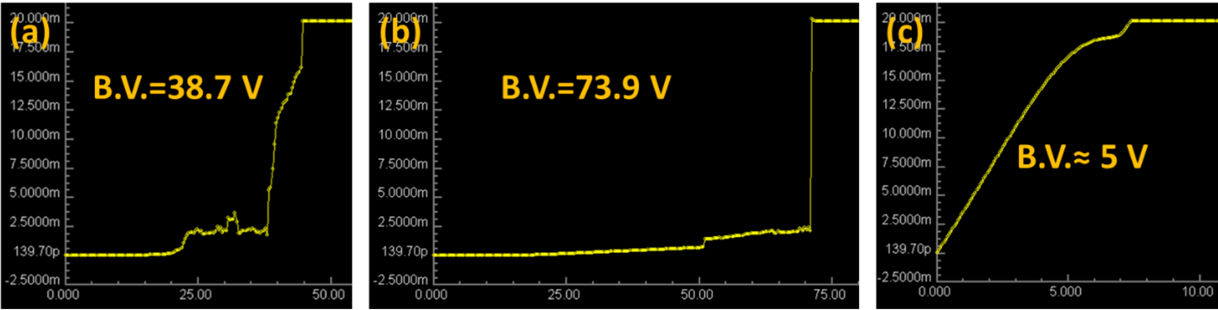

Figure 3.19 Breakdown voltage (B.V.) results for (a) ~100 nm front-side released capacitive gap; (b) a ~250 nm backside released capacitive gap; (c) capacitive gaps with particles due to capillary forces.

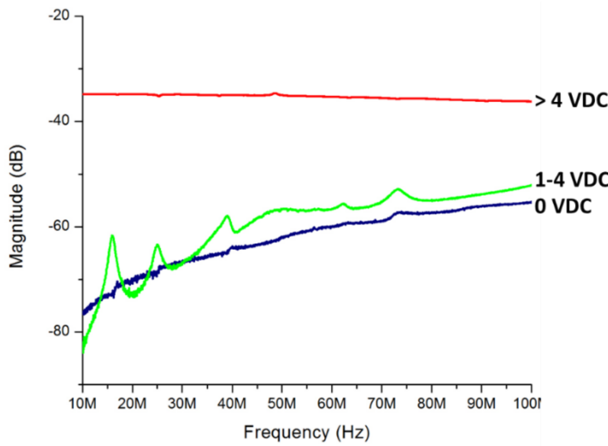

Figure 3.20 Transmission response of 50 μm-radius disk resonator before and after a DC bias voltage is applied.

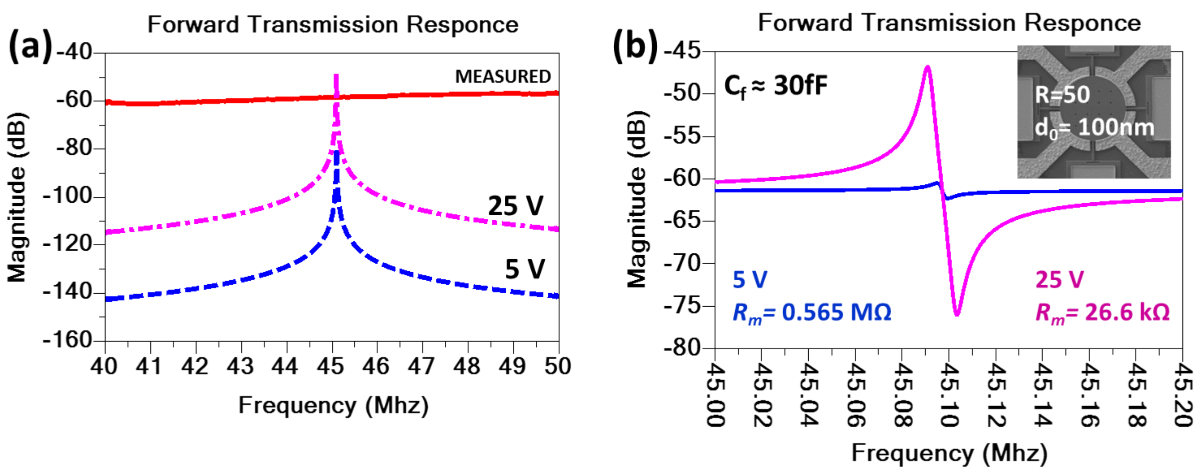

Figure 3.21 Simulation of resonator response: (a) measured spectrum compared to simulated responses for 5V and 25V and (b) simulated responses of 5V and 25V using measured C_f.

www.manaraa.com

CHAPTER 4 PIEZOELECTRIC RF MEMS RESONATORS

Piezoelectrically-transduced resonators have very similar characteristics to capacitive driven resonators such as the ability of having high Q factors, high resonant frequencies, and low equivalent mass (M_{re}) values. What really set them apart is their modes of actuation as described in chapter 2. Piezoelectrically-transduced resonators rely on a polarized crystal layer, which in most cases tend to be lossy compare to the pristine capacitive actuation of a single-crystal silicon. However, capacitive devices heavily rely upon a dielectric capacitive gap that needs to be scaled down to nanometer ranges to obtain a sufficiently strong transduction. This is very challenging, as described in chapter 3, because it requires special capacitive gap reduction and delicate release techniques. On the other hand, piezoelectrically-transduced resonators don't rely on a capacitive gap; thus, the electrodes can be directly coupled with the piezoelectric layer. This allows the transduction at resonance to be much stronger than capacitive devices resulting in smaller motional resistance (R_m) values than capacitive devices [48]. To decreases the R_m of piezoelectric devices, the electrode coupling efficiency needs to be maximize by electrode design. For a width-extensional rectangular mode, this can be observed by substituting equation (2.11) into (2.40):

$$R_m \approx \frac{\omega_0 \rho_n t_n}{Q E_n^2} \cdot \frac{W}{N^2 d_{31}^2 L} \tag{4.1}$$

where L, W, and N are the length, width, and number of the top electrodes, respectively.

As shown in equation (4.1), the motional resistance can be minimized by four electrode design dependent parameters W, L, d_{31}^2, and N that will be detailed in section 4.9. Also, the microfabrication can be fully optimized by using standard CMOS processes. In recent advances, a

www.manaraa.com

newly emerging technology known as TPoS has enabled the fabrication of piezoelectric devices with comparable Q factor and resonant frequency values as the ones obtained by capacitive devices. In this chapter, the design, fabrication and test results of different types of piezoelectrically-transduced resonators will be covered.

4.1 Resonant Frequency and Mode Shape Selection

In order to discriminately select a specific resonant frequency and mode shape of choice, few design parameters can be used. Similarly to capacitive resonators, both the electrodes and tethers (anchors) can be designed in ways to achieve this goal. As shown in Figure 3.2, a 3D model is derived from a 1st contour resonant mode of a disk shaped resonator using FEM COMSOL Multiphysics®. Like the capacitive resonators, the maximal displacement is used for electrode design and placement of tethers.

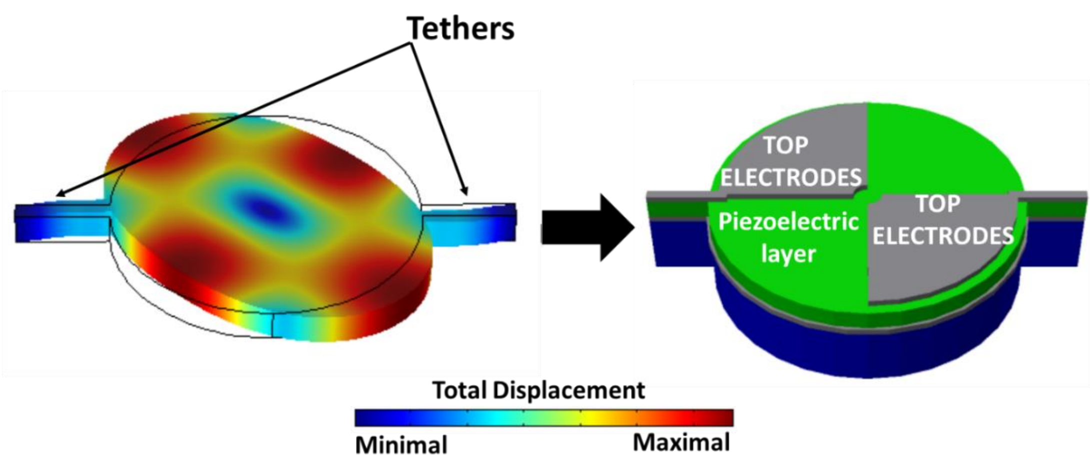

Figure 4.1 Electrode and anchor design approaches for a 1st contour resonant mode and anchor location used to create a 3D device matching the FEM COMSOL Multiphysics® modal analysis model.

For more complex geometries and higher resonant frequencies, the strain field of the resonant mode is preferred to match the electrode design as demonstrated in Figure 4.2.

www.manaraa.com

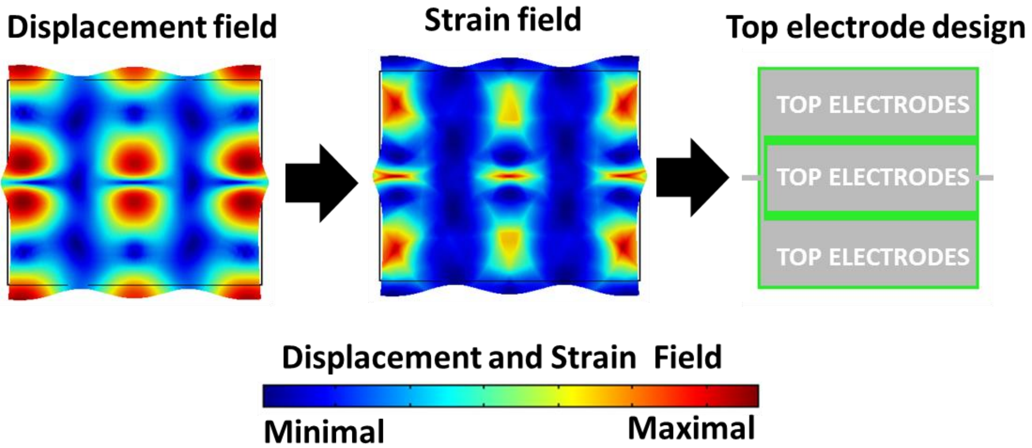

Figure 4.2 Electrode and anchor design approaches using FEM COMSOL Multiphysics® modal analysis that models a N3 length-extensional resonant mode needed to create a 3D device matching model.

4.2 Piezoelectrically-transduced Resonator Fabrication Process

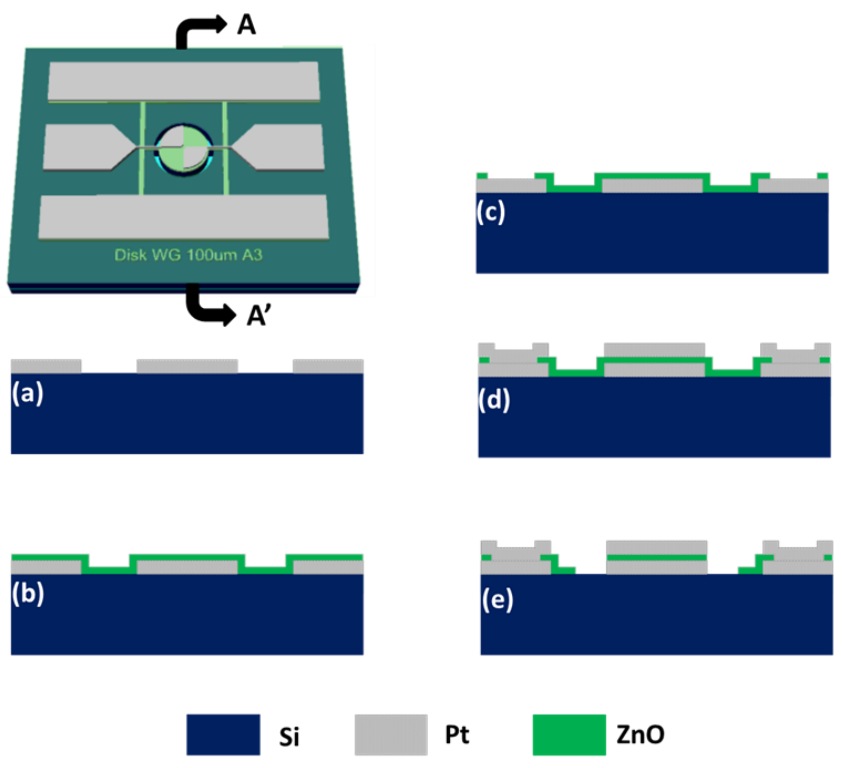

Figure 4.3 Step-by-step illustration of the piezoelectrically-transduced resonator fabrication process flow; (a)bottom lift-off process of sputtered platinum; (b) reactive sputter deposition of ZnO thin piezoelectric film; (c) via opening through ZnO wet etching; (a) top electrode lift-off process of sputtered platinum; (d) ZnO dry DRIE etching of the resonator.

www.manaraa.com

Piezoelectric devices were developed to achieve a lower motional resistance through the employment of a well characterized ZnO piezoelectric layer and top electrode design that matches the strain field. These devices have been microfabricated using a high resistivity single crystal silicon (for ZnO thin-film resonators), SOI (for ZnO-on-silicon resonators), and Poly-SOI (ZnO-on-Polysilicon resonators) substrates. The ZnO thickness ranges from 500 nm to 750 nm and the device layers for the ZnO-on-substrate devices have a thickness range from 5 μm to 20 μm. Figure 4.3 summarizes the fabrication process flow (without the release which will be covered in section 4.4) that consists of four photolithography steps. The fabrication process begins with a photolithography step using 300nm of LOR-3B and 1 μm AZ1512 to generate a clean lift-off profile (see section 4.2). This is a critical step because the overall performance of the device depends on cleanness of its geometry. Then, a sputter deposition of 40nm Cr/ 200nm Pt is followed. It is worthwhile to mentioning that sputter metal deposition, especially for Pt, achieves better overall quality and adhesion in comparison with evaporated Pt. Next, the sample is placed inside a glass petri dish with AZ400T photoresist stripper overnight for lift-off. The final bottom electrodes lift-off profile is shown Figure 4.3(a). Then, a reactive sputtering deposition of 500 nm to 750 nm of ZnO is performed as seen in Figure 4.3(b) with optimized parameters to achieve a (002) c-axis aligned crystal orientation (see section 4.3). A photolithography step follows using a 1 μm AZ1512, and then the vias are created using ZnO wet etch solution of 1 HCL:100 H_2O to generate a direct connection to the ground electrode as seen in Figure 4.3(c). A photolithography step using a 300 nm of LOR-3B and 1 μm AZ1512 followed by a metal sputtering of 40 nm Cr/ 200 nm Pt is performed. The sample is placed the inside a glass petri dish with AZ400T photoresist stripper overnight for lift-off. The final bottom electrodes lift-off profile is shown in Figure 4.3(d). Next, a photolithography step using a 5 μm AZ12XT follows, then a customized reactive ion

www.manaraa.com

etching ZnO etch recipe using CH_4 at room temperature is performed to define the body of the resonator as seen in Figure 4.3(e).

4.3 Lift-off Characterization

The lift-off profile and the quality of Pt are very important because the geometry and (002) c-axis orientation of the sputtered ZnO can be affected. It is widely known that the lift-off process of sputtered metals is far from easy, even when common negative photoresists are used such as the case of NR9-3000PY. However, a specially designed resist known as LOR-3B by MICROCHEM© performs exceptionally well with I-line TMAH based photoresist developers as an undercut layer.

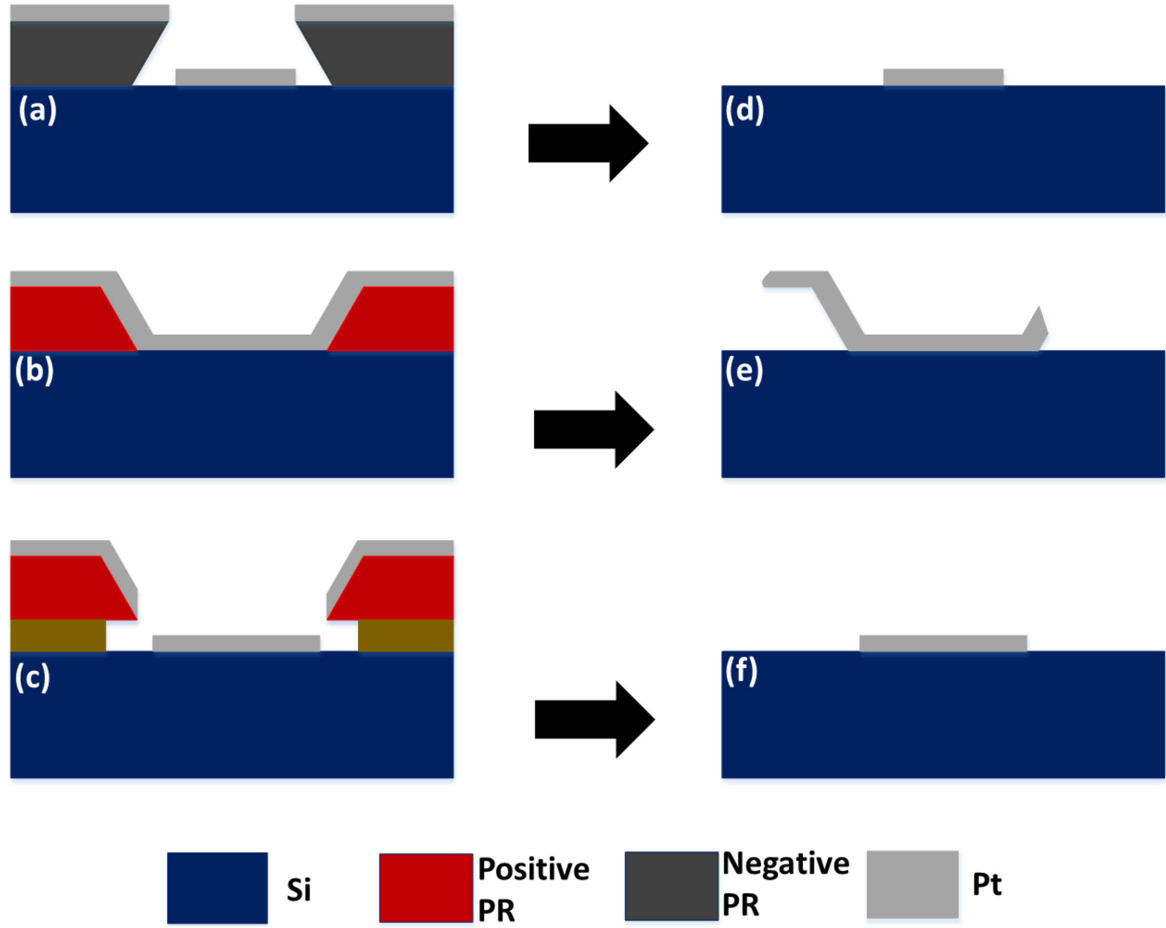

Figure 4.4 Lift-off profiles using: (a) negative photo resist; (b) positive photoresist; (c) LOR-3B in combination with positive photoresist.

www.manaraa.com

It is well documented that negative photoresist is by far the most widely used photoresist for metal lift-off processes. However, negative photoresist is one of the hardest photoresist to characterize. This drawback is due to the fact that when a negative profile is needed, such as the one illustrated in Figure 4.4(a), a great deal of effort to characterize the recipe is needed. Characterization of negative photoresist is very hard especially when dealing with features smaller than 5 µm, because to achieve a negative profile the photoresist has to be overexpose in a time-controlled manner. Since most UV bulb based exposure systems don't have a consistent uniformity, it is common to find features in some areas of the wafer to be overexposed while others are still underexposed. This inconsistency affects greatly the geometry and topology of the intended pattern. When the wafer is overexposed, most of the smaller features don't develop fully or not at all. In the case of underexposed, a similar profile to the positive photoresist is achieved as seen in Figure 4.4(b), making a clean lift-off process hard to achieve. This effect is commonly seen after the wafer has gone through multiple fabrication steps and the topography is not completely flat. A typical negative profile can be observed in Figure 4.5(a) where the features are slimmer due to the negative nature of the profile. I-line positive photoresists such AZ -line are known for their large tolerance to either over and under exposure, this allows a higher yield for devices with smaller features. Positive photoresist is also used for lift-off processes but its overall profile quality is worse than negative photoresist and it is difficult to achieve small features via metal lift-off. As shown in Figure 4.4(b), positive photoresist achieves the opposite exposure profile thus making it very difficult to achieve a clean lift-off because deposited layers coated over the sidewalls conformably. In most of the cases, an ultrasonic bath is needed to be able to tear apart the metal to define the edge of the intended pattern. The results are rough edges and in some cases features smaller than 3 µm are torn away with this physical removal process as shown in Figure 4.5(b). A great solution

www.manaraa.com

that allows both a high yield of features smaller than 3 μm and a clean lift-off is achieved when LOR-3B is integrated into the process. As seen in Figure 4.4(c) and Figure 4.5(c), LOR-3B is a resist that is deposited before a positive photoresist layer to generate a controllable undercut profile for the lift-off processes.

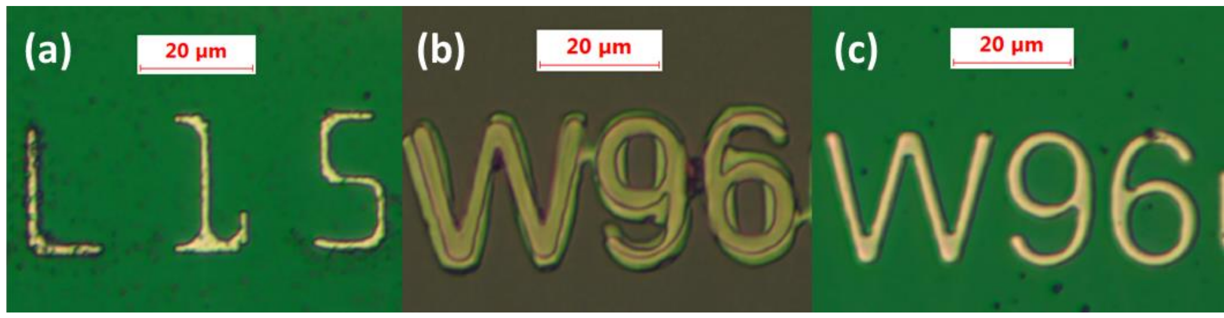

Figure 4.5 Optical images of lift-off profiles after using: (a) (NR9-3000PY) negative photoresist; (b) AZ1512 positive photoresist; (c) LOR-3B and AZ1512.

4.4 ZnO Magnetron Deposition Characterization

In order to have a strong transverse piezoelectric coefficient, d_{31}, a good quality (002) c-axis oriented ZnO thin-films are needed. It is well known that there is a correlation between c-axis crystal orientation and d_{31}. For piezoelectric contour resonant modes, highly c-axis oriented ZnO thin-films are needed to minimize the transduction losses to achieve a lower motional resistance. After a few trials, good quality films were achieved by customizing the following three key parameters: oxygen concentration, substrate temperature, and post-deposition annealing. It has been well documented that ZnO dissociates into zinc and oxygen atoms in a reactive sputtering deposition [49]. Independently, some of free zinc atoms don't tend to recombine with oxygen causing an excess of Zn on the deposited film. Therefore, an oxygen environment is needed as a reactive gas to ensure a O_2 rich ZnO film. For this case, it was found that ZnO films grown in a 1:1 ratio of O_2:Ar environment exhibit the strongest (002) crystalline orientation. Substrate temperature also plays an important role because it helps the deposited ZnO achieve its

www.manaraa.com

piezoelectric crystal characteristic. For this work, 300°C in-situ annealing give us the best results. Finally, post-deposition annealing treatment helps enhance the crystal orientation as seen in Figure 4.6.

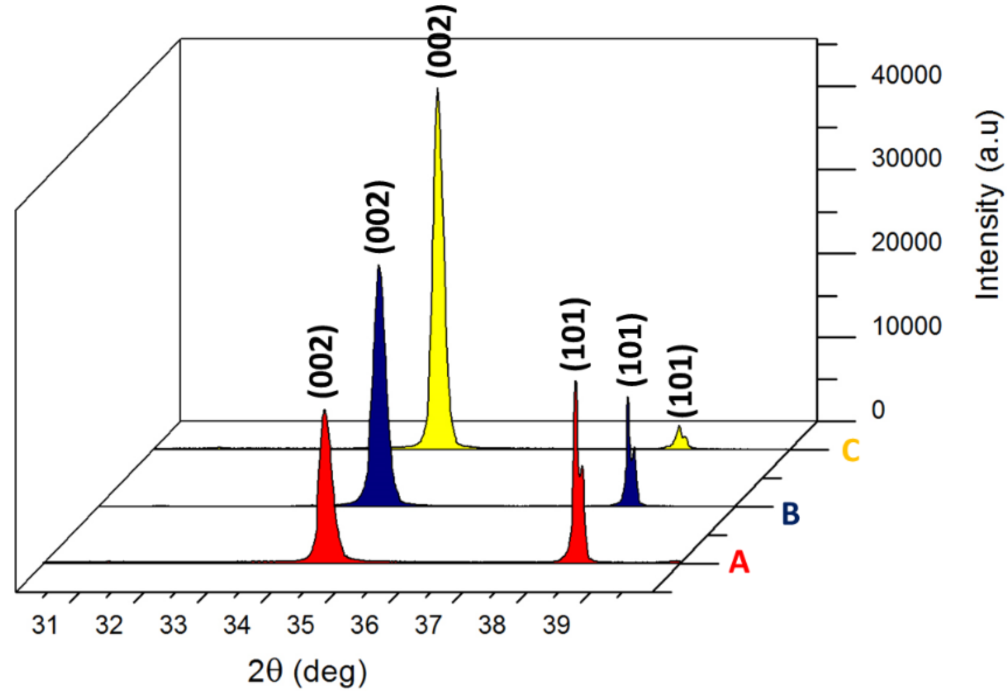

Figure 4.6 XRD of a 500nm sputtered ZnO layer after annealing treatments: (a) no treatment; (b) 300°C for 1hour; (b) 400°C for 1 hour.

4.5 Release Process for Piezoelectrically-transduced Resonators

In section 4.1, the microfabrication process to fabricate a piezoelectric resonator was covered with the exception of the final release step. In fact, the release process of ZnO thin-film resonators is the most challenging fabrication step and it can be done in several ways. For this work, four different approaches that yields four different results as shown in Figure 4.7 were demonstrated.

Figure 4.7 (a) shows the first release that was tried, it consisted of releasing the resonator by undercutting the Si substrate. This approach yields a suspended membrane consisting of just the top and the bottom electrodes with a sandwiched ZnO layer sandwiched in between.

www.manaraa.com

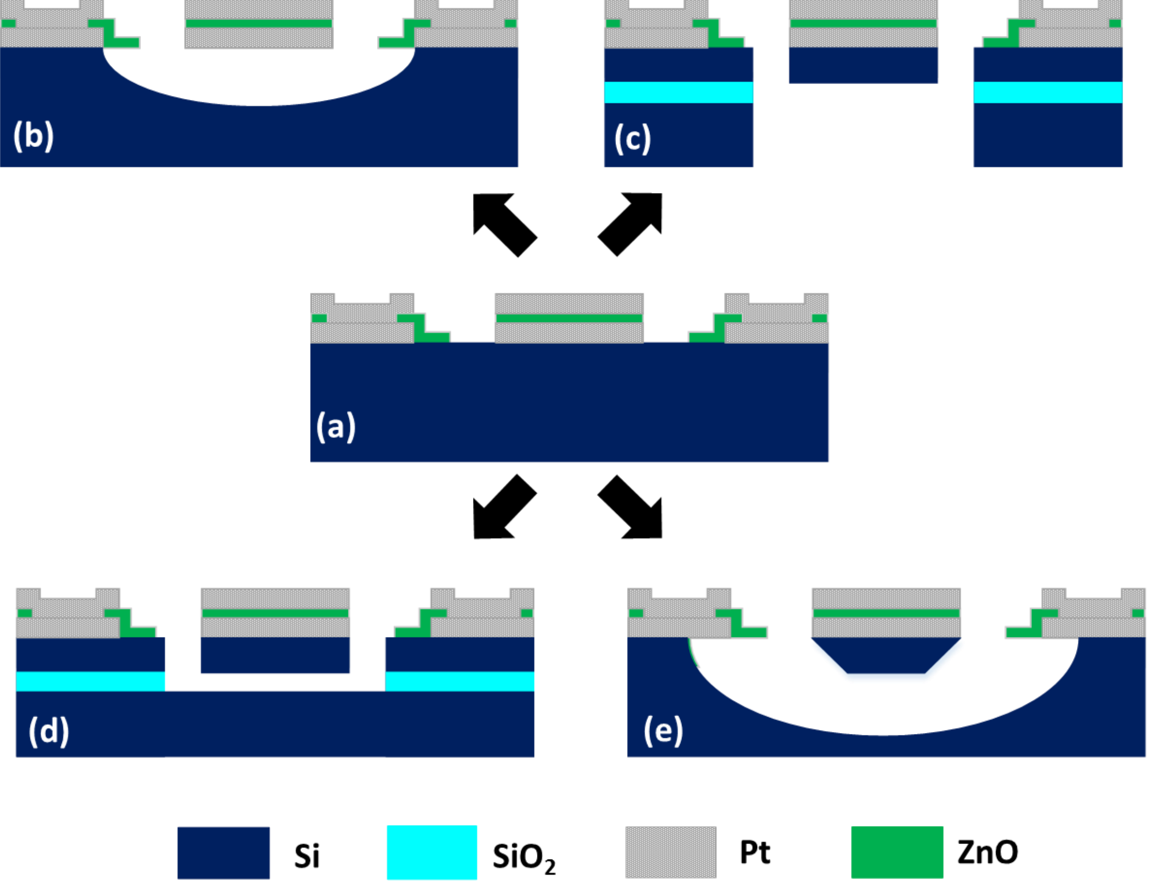

Figure 4.7 2D illustration of four different release techniques: (a) device perspective without release, (b) DRIE SF_6 isotropic dry release, (c) TSV HAR DRIE backside dry release, (s) 49% HF pre-release, (c) SRE dry release.

The advantage of this approach is that the release is simple and it can be done on a wafer level in just one hour. A more complex release is needed to fabricate ZnO-on-substrate resonators as shown in Figure 4.7(c)(d)(e). ZnO-on-Si resonators consist of a suspended piezoelectric layer sandwich by two electrodes and coupled with a single crystal Si layer. For this case, a SOI substrate is preferred because it allows to simplify and minimize the fabrication steps to have a high yield of working devices. However, one more photolithography step is needed as compared to thin-film ZnO resonators because it requires a localized release step by using either wet or dry etching to controllably release the resonant body.

www.manaraa.com

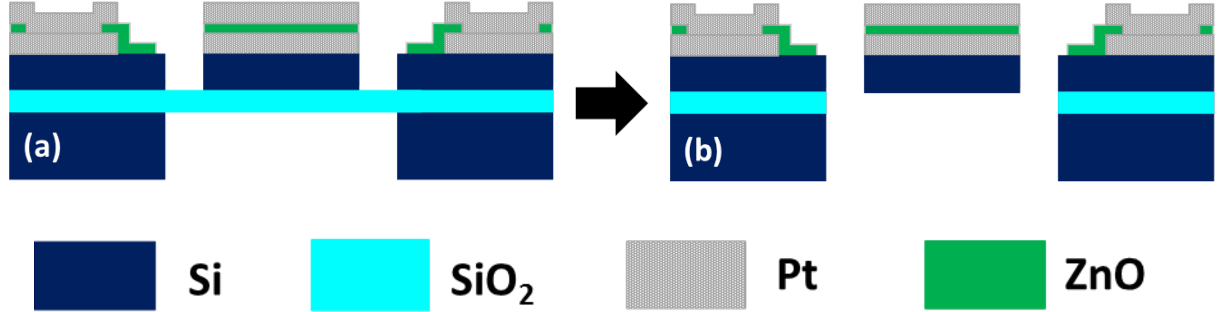

Figure 4.8 2D illustration of ZnO-on-Si backside release: (a) TSV HAR DRIE Si backside etch followed by (b) a SiO2 DRIE release etch.

Starting from Figure 4.8 (a), the device layer is protected by a 7 µm layer of AZ12XT photoresist. A photolithography step using a 7 µm layer of AZ12XT takes place followed by backside aligning to define the release window. Then, a through silicon via (TSV) etch step using the HAR DRIE Si etch is performed. It is worthwhile mentioning that ZnO can be easily etched by wet chemicals such as HF or BOE. Therefore, the next step is a SiO_2 DRIE dry etch to remove the BOX oxide, thus fully suspending the device. It is important to note that the wafer should be diced to avoid the plasma loading effects of the DRIE system [50].The die is left overnight in a petri dish with AZ400T photoresist stripper. Finally, the device is rinsed with D.I. water and isopropanol, then it is placed in an oven at 100°C for quick drying. Figure 4.7 (d) shows another release technique for ZnO-on-substrate resonators known as oxide pre-releasing. Referring to Figure 4.3 (a), using a SOI wafer as our starting substrates, the first step is to pattern the body of the resonator as shown in Figure 4.3 (e). A HAR Si DRIE dry etching using the BOX oxide layer as the etch stop layer is then conducted. This is done as the first fabrication step to be able to release the Si resonator body using a 49% HF release bath before any other fabrication steps as shown in Figure 4.9 (a). Then all the remaining fabrication steps as illustrated in Figure 4.3 follows

www.manaraa.com

until the device is completed as shown in Figure 4.9 (b). It's important to note that the first step is to release the devices, and then all sequential steps need to the performed with extreme care otherwise the suspended membranes tend to collapse. A useful tip is not to N_2 blow dry the devices after wet processes such as solvent clean and developing. In my experience, the oven drying the devices at 50°C follow by a 50 W 300 sccm O_2 plasma clean is the best approach.

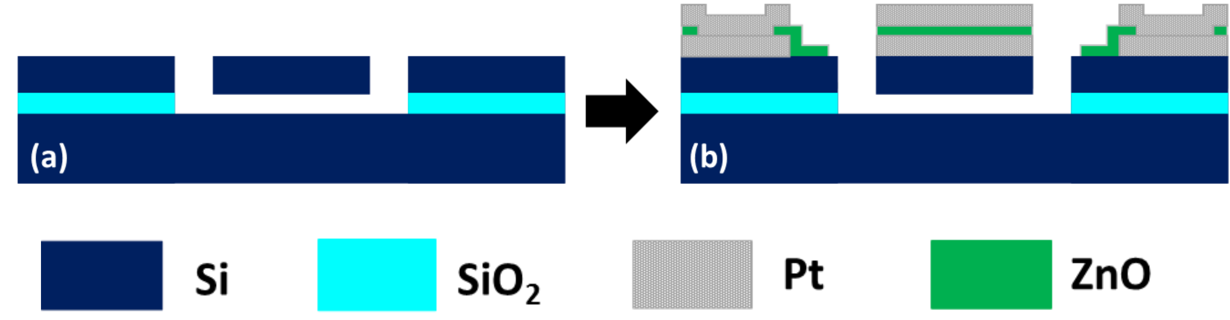

Figure 4.9 2D illustration of oxide pre-releasing: (a) pre-release profile after HAR DRIE and 1 hour of 49% HF, (b) device cross-sectional profile after all fabrication steps are done.

SOI wafer technology has revolutionized the way devices are designed, but it is still a very costly alternative with prices ranging from $150 to over $1,000 dollars per wafer depending on the needed properties. ZnO-on-Si devices take advantage of the high electromechanical coupling of the piezoelectric material and the low damping coefficient of the single crystal Si device layer. Therefore, as long as the wafer has a good quality single crystal Si, the following cost and time effective release technique can be used. Figure 4.10 (a), the thin-piezo on single-crystal reactive etched (TPoSCRE) technique begins with a HAR DRIE Si dry etch to define the resonant body of the desired Si coupled layer. Then, an ALD deposition of 30 nm Al_2O_3 follows to define the etch protection layer as shown in Figure 4.10 (b). This is followed by a SiO_2 DRIE dry etch to remove the 30 nm AL_2O_3 from the horizontal surfaces. It is important to note that the H_2 free radical that is used for etching oxides fairly directional at -20°C. Therefore, it only etches the horizontal Al_2O_3 layer as seen in Figure 4.10 (c). The final step is to perform a SF_6 isotropic dry

المنارة للاستشارات
www.manaraa.com

etch at room temperature to release the device as shown in Figure 4.10 (d). The final product is a suspended membrane with a Si coupling layer. The great advantage of this technique is that it can be customized to obtain any device layer thickness.

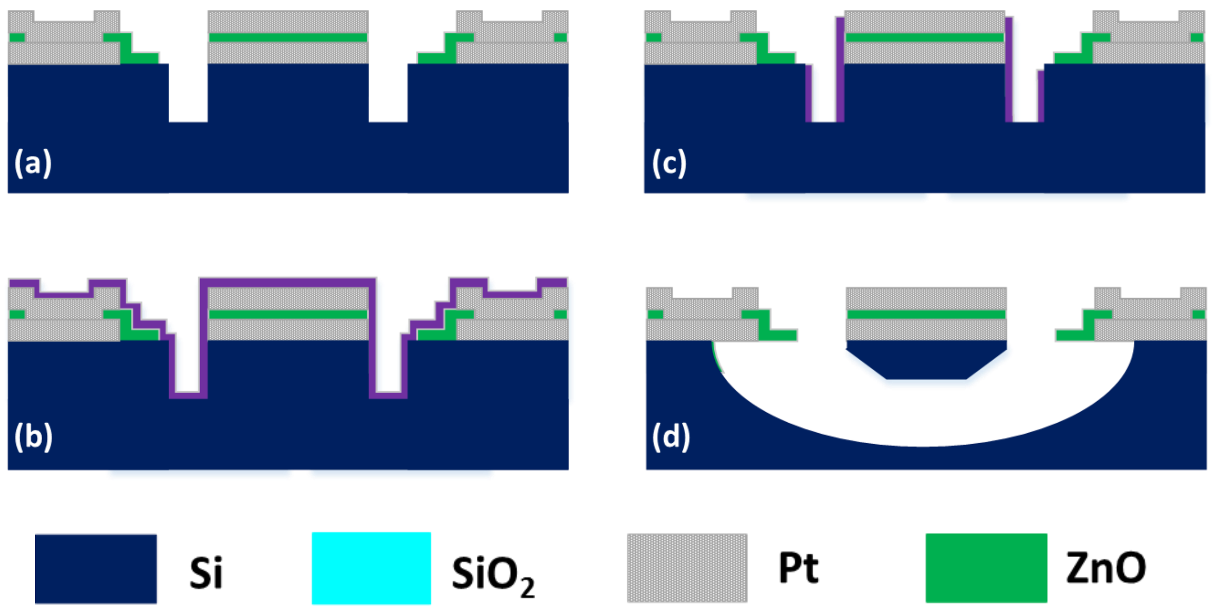

Figure 4.10 2D illustration of the TPoSCRE release technique: (a) HAR Si DRIE dry etch of Si; (b) ALD deposition of 30 nm Al_2O_3 layer; (c) SiO2 DRIE etch of horizontal Al_2O_3 layer; (d) Si DRIE isotropic release etch of Si.

4.6 On-wafer Probing 2-port Set-up

The devices were tested using a cascade RF probe station with on-chip probing capabilities after fabrication. The HP 8753E VNA was calibrated using a Short-Open-Load-Thru (SOLT) calibration procedure using a CS-5 calibration substrate provided by GGB industries Inc. This establishes the measurement reference planes at the probes by removing the effects of cables, connectors and the VNA electronics. The scattering parameters (S-parameters) were extracted after carefully landing a pair of GSG-150 microprobes on to the metal contact pads using a pair of cascade micromanipulators. The GSG-150 microprobes were connected directly to the VNA via coaxial cables as illustrated in Figure 4.11.

www.manaraa.com

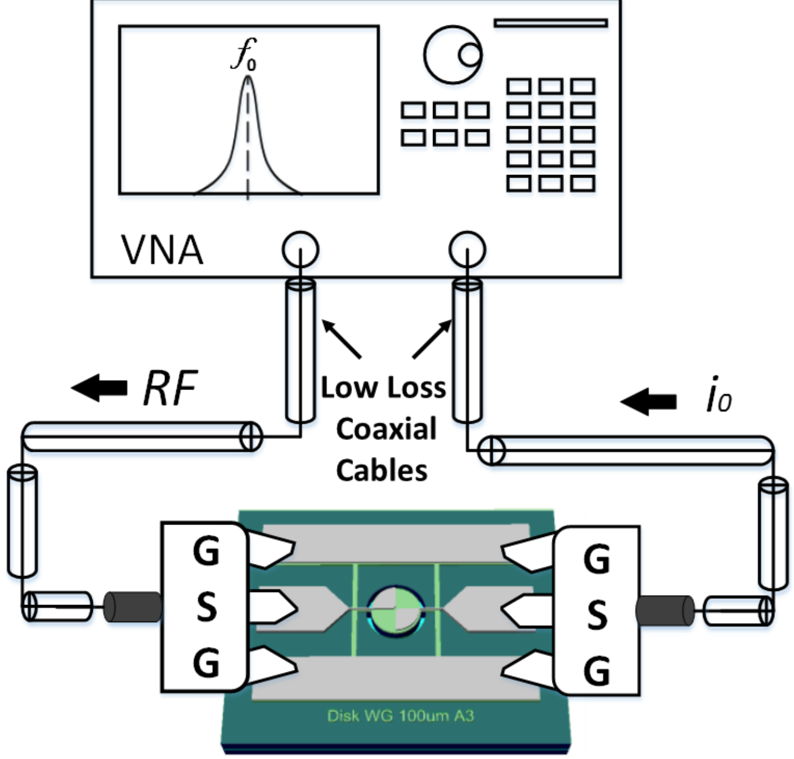

Figure 4.11 Illustration of RF test set-up for on-wafer probing characterization of piezoelectric actuated resonators.

Since the obtained s-parameters from this test set-up includes external circuit influences such as the parasitic resistances of components and VNA port termination resistance (R_L=50Ω), matched to the R_m of the device. Therefore, the Q factor is reduced because the mismatch between the R_m and R_L affect the electrical response of the device. The measure Q factor is known as the loaded Q factor (Q_L). The intrinsic Q factor or unloaded Q factor (Q_{UL}), can be calculated by knowing the relationship between Q_L, Q_{UL}, and measured insertion loss (IL) expressed as [51]

$$\frac{Q_{UL}}{Q_L} = \frac{10^{\frac{IL}{20}}}{10^{\frac{IL}{20}} - 1} \tag{4.2}$$

Once Q_L and Q_{UL} are found from Equation (4.2), then the R_m can be determined by:

$$Q_L = Q_{UL} \frac{R_m}{R_m + R_L} \tag{4.3}$$

www.manaraa.com

4.7 Thin-film ZnO Resonators

Thin-film ZnO contour-mode resonators were fabricated as illustrated in Figure 4.3 with a 750nm-thick ZnO layer. Then, they were released using a DRIE SF_6 isotropic dry release as illustrated in Figure 4.3(b). This is a high yield technique that allows almost 100% of the devices to be successfully released with minimum damage to the electrodes and ZnO device layer as seen in Figure 4.12.

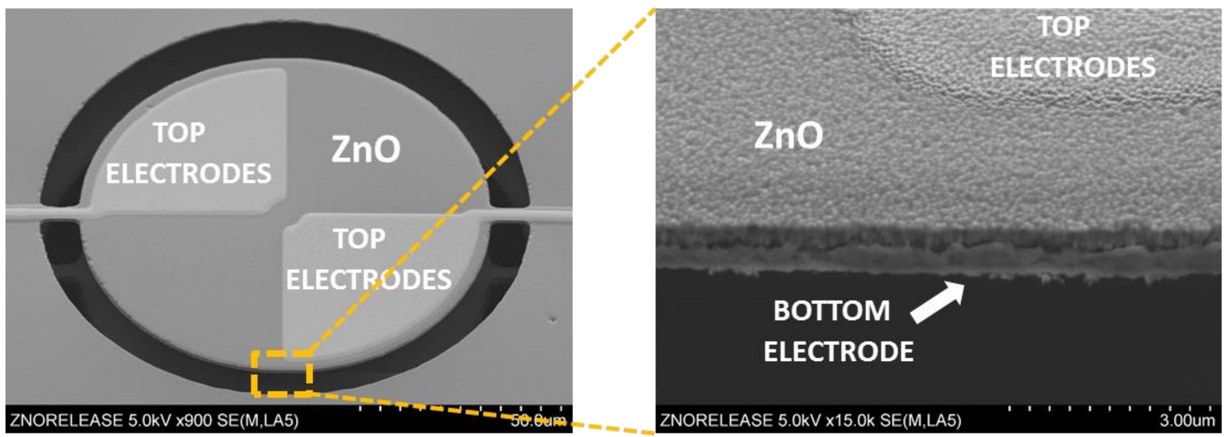

Figure 4.12 SEM photos of 1st contour mode thin-film ZnO resonator after the releasing step.

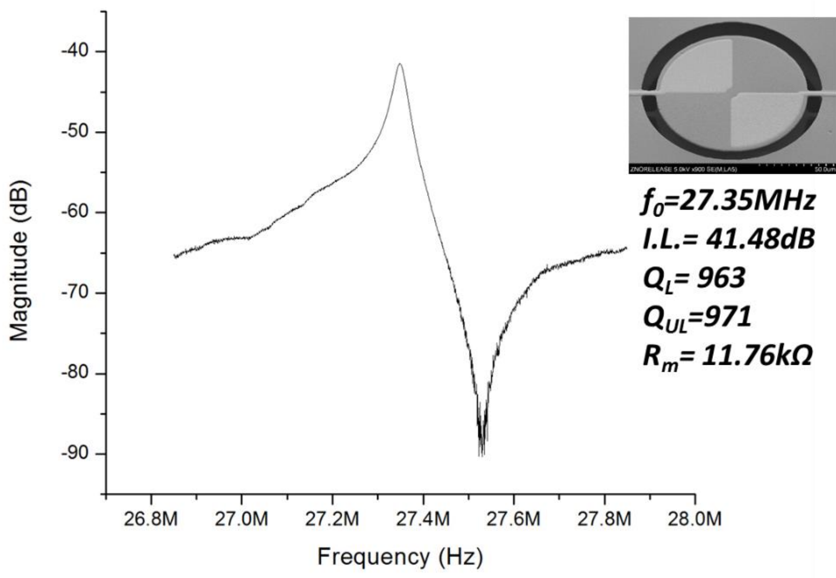

Figure 4.13 Measured forward transmission frequency response of a 38 μm-radius 1st contour mode thin-film ZnO disk resonator.

www.manaraa.com

As shown in Figure 4.13, the forward transmission response (S21) of a 38 µm-radius disk resonator operating at the 1st contour mode were obtained from a 2-port measurement using the test configuration described in section 4.6. This device exhibits a loaded Q factor of 963 and a R_m value 11.26 kΩ. As covered in chapter 2, such high R_m values are not ideal for device to circuitry integration but this resonator can still be used as a standalone sensor with proper amplification.

Larger devices such as the ones illustrated in Figure 4.14, suffer from surface deformation due to stress-induced buckling. This happens because the suspended membrane is so large that it cannot rigidity support itself causing an inward buckling effect due to residual stress. This affects the electrical characteristics of the device since its crystal structure is no longer completely aligned along its c-axis. As shown in Figure 4.15, the electrical characteristics of a square plate resonator operating at the N3 length-extensional mode were extracted using the test configuration discussed in section 4.6. It can be observed that the frequency response of this device has a spurious peak nearby its resonance frequency as compared to the responses of the smaller disk resonator in Figure 4.13 due to buckling. The N3 length-extensional mode square plate resonator exhibits a loaded Q factor of 401 and an R_m value 1.31 kΩ. The R_m value of this resonator is still too large to be able to integrate with CMOS compatible technology and its loaded Q factor is lower than smaller devices because of buckled ZnO device layer.

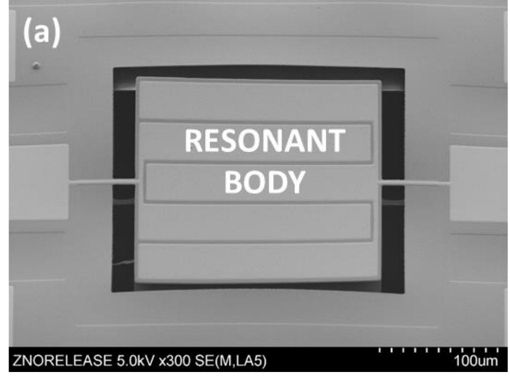

Figure 4.14 SEM images of 150 µm-length extensional ZnO square resonators: (a) n5 and (b) n9.

المنارة للاستشارات
www.manaraa.com

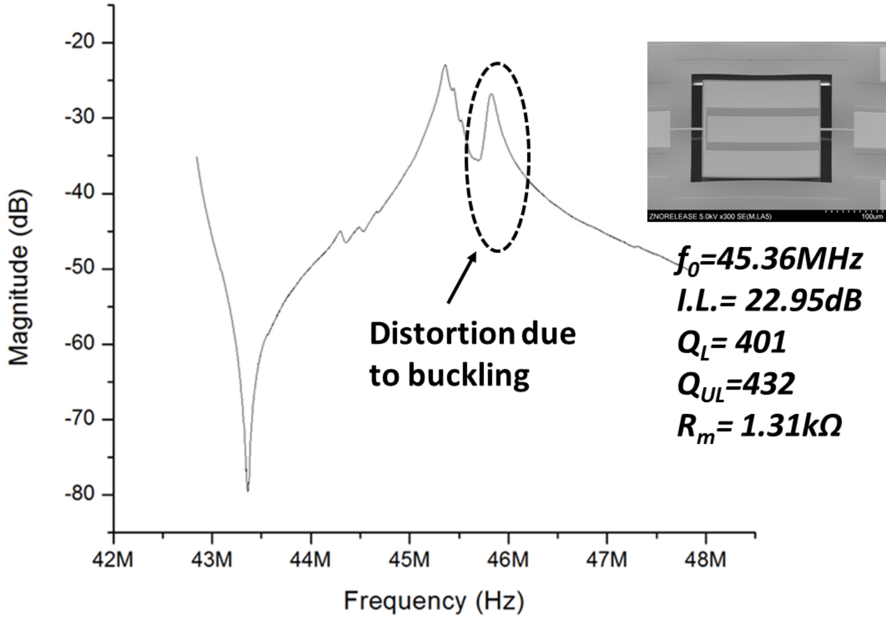

Figure 4.15 Captured forward transmission response demonstrating the effects of ZnO buckling in a N3 150μm-length extensional square resonator.

4.8 Thin-film ZnO-on-Si Resonators

TPoS resonators are a new emerging high Q factor and frequency-selective resonant technology that its overall device performance is comparable to those of capacitive resonators. This technology has demonstrated high frequency resonances (up to GHz) with high Q factors (>10,000). The biggest advantage of TPoS resonators over other existing resonant technologies is the low reported R_m values (As low as few hundred ohms) [52]. As described in section 2.5, this due to the high electromechanical coupling of ZnO with low mechanical loss substrates such as single crystal Si. This combination allows the acoustic energy to be mostly dissipated within single crystal Si. Thus, the electrical and mechanical performance of the device is mostly represented by the characteristics of the Si layer. In addition, they share the same microfabrication steps as thin-film ZnO contour mode resonators as illustrated in Figure 4.3 with just a different release technique as described in section 4.5. This allows a high yield and robust production of these devices, which

www.manaraa.com

are ideal for building reliable and reproducible mass sensor platforms. In this work, a broad range of designs have been fabricated, including disk resonators with radius ranging from 25µm to 150 µm, square resonators with lengths ranging from 50 µm to 300 µm, and rectangle resonators with widths and lengths ranging from 60 µm to 300 µm.

4.9 TSV Thin-film ZnO-on-Si Resonators

Through silicon via (TSV) thin-film ZnO contour mode resonators were fabricated as illustrated in Figure 4.3 with a 500 nm to 750 nm-thick ZnO films using SOI wafers as the starting substrate. As shown in Figure 4.16, the devices were successfully released using the TSV HAR DRIE backside dry release technique as illustrated in Figure 4.8. Three SOI substrates with 5 µm, 10 µm, and 20 µm-thick device layers and similar electrical characteristics were investigated:

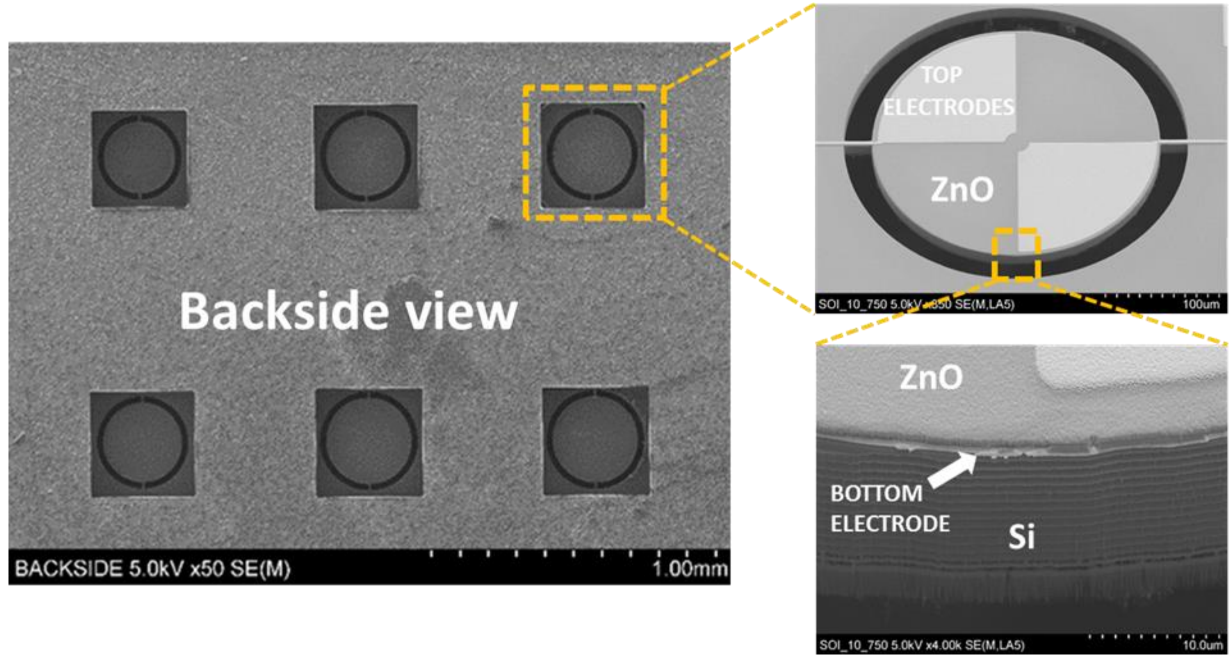

Figure 4.16 SEM images of TSV released ZnO-on-Si 1st contour mode disk resonator.

Even though, TSV HAR DRIE backside dry release is a high yield technique similar to DRIE SF6 isotropic dry release, it leaves a rough profile on backside of the Si device layer. This

www.manaraa.com

happens because the SiO_2 dry etching recipe that is used doesn't have a high selectivity to SiO_2 and its H_2 free radicals also attack Si. Therefore, a time controlled DRIE SiO_2 etch is needed in order to minimize the damage on the Si device layer that could affect the mechanical performance of the resonator. In general, this release technique was the most successful to fabricate ZnO-on-Si resonators in this dissertation because once the parameters of TSV HAR DRIE of Si and SiO_2 were characterized, which it became very reproducible. The only drawback is that the devices need to be diced before release, because the DRIE plasma loading effects across a silicon wafer are very unpredictable, especially with low etch selective recipes for etching SiO_2. In addition, high power of recipes such as SiO_2 DRIE dry etch, dissipates energy slower on larger Si substrates which leads to the tendency of burning photoresist layers.

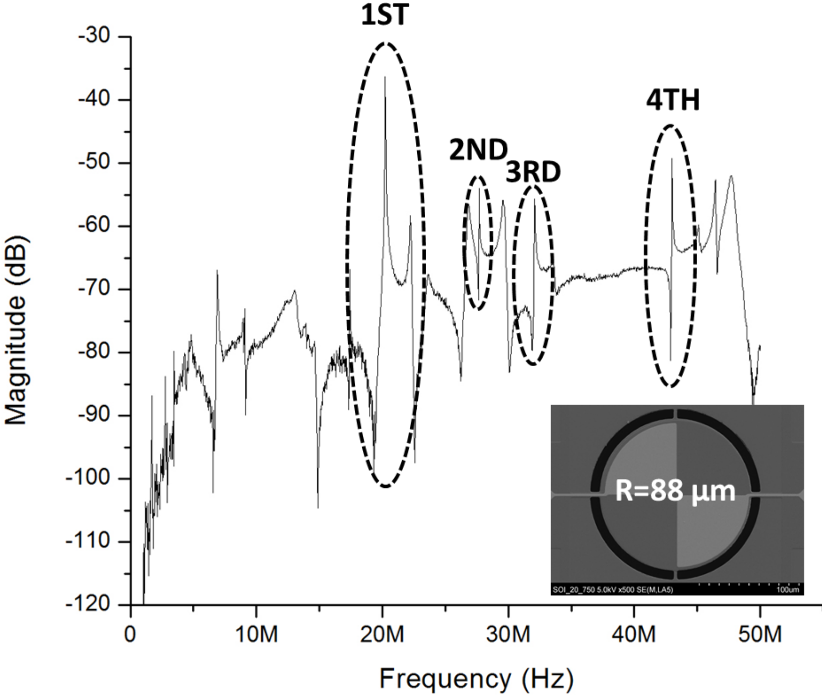

Figure 4.17 Measured forward transmission frequency response of a wide frequency span of 30 kHz to 50 MHz from a 1st contour mode 88 µm-radius disk resonator.

The fabricated devices were tested using the configuration illustrated in section 4.5. As seen in Figure 4.17, the designed frequency response of 20MHz from a 1st contour mode 88µm-

المنارة للاستشارات
www.manaraa.com

radius disk resonator was the strongest in the wide span between 30 kHz and 50 MHz. The other frequency responses are known as harmonic modes or spurious responses. The harmonic modes are the responses of other excited resonant modes. Four contour modes can be identified using the theoretical approached covered in chapter 2 as demonstrated in Figure 4.17. Also, the 1st contour mode has the lowest motional resistance (R_m) value compared to the other exited contour mode resonances as seen in Table 4.1.

Table 4.1 1st Contour Mode 88 μm-radius ZnO-on-Si Disk Design vs. Spurious Responses.

R=88μm				
Mode	**1ST**	**2ND**	**3RD**	**4TH**
f_o (MHz)	20.24	27.65	32.1	42.97
I.L. (dB)	30.54	52.94	55.62	48.35
Q_L	2,011	1,103	462	3,788
Q_{UL}	2,073	1,103	463	3,805
R_m (Ω)	3,270	44,261	60,295	26,052

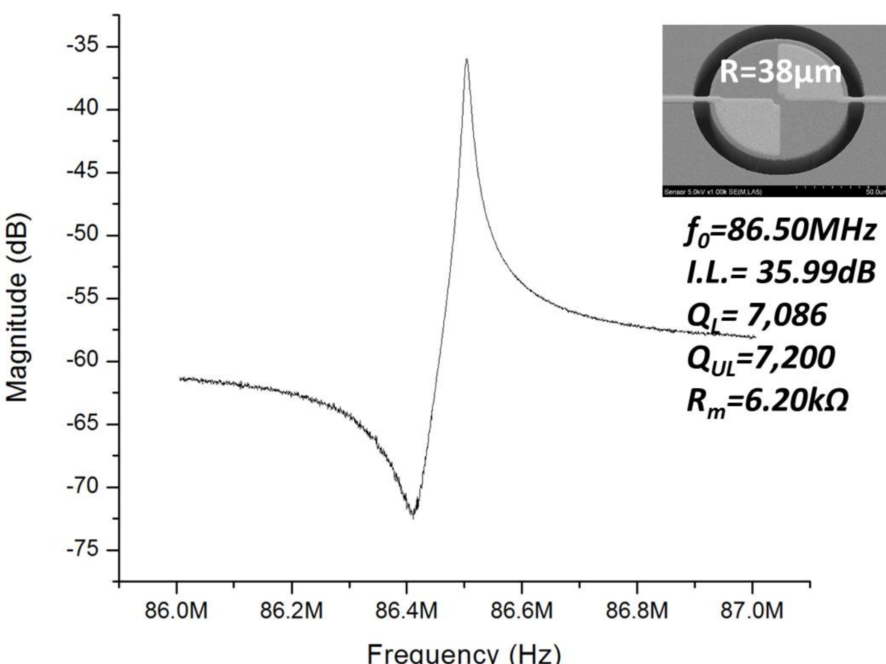

Figure 4.18 Measured forward transmission frequency response of a strong 4th order contour mode response from a 1st contour mode 38 μm-radius disk resonator.

www.manaraa.com

In order to design an ultrasensitive mass sensor, the harmonic modes can be taken into consideration depending upon the design parameters needed to be accomplished. As described section 2.10, the sensitivity depends on three parameter f_o, M_{re}, and Q factor. Therefore, the intended device needed to have the best sensitivity and resolution regardless of its R_m value then the 4th order contour harmonic disk response can be used. As shown in Figure 4.18, smaller disk resonators (<50 µm-disk radius) can have very strong harmonic frequency responses with great electrical characteristics.

In order to be able to correctly predict the frequency response of ZnO-on-Si disk contour mode resonators, a direct comparison between theory-predicted and measured responses needs to be done. The theoretical approach follows the equations covered in section chapter 2 and the measured data was obtained from a set of disk resonators with diameters ranging from 100 µm to 300 µm.

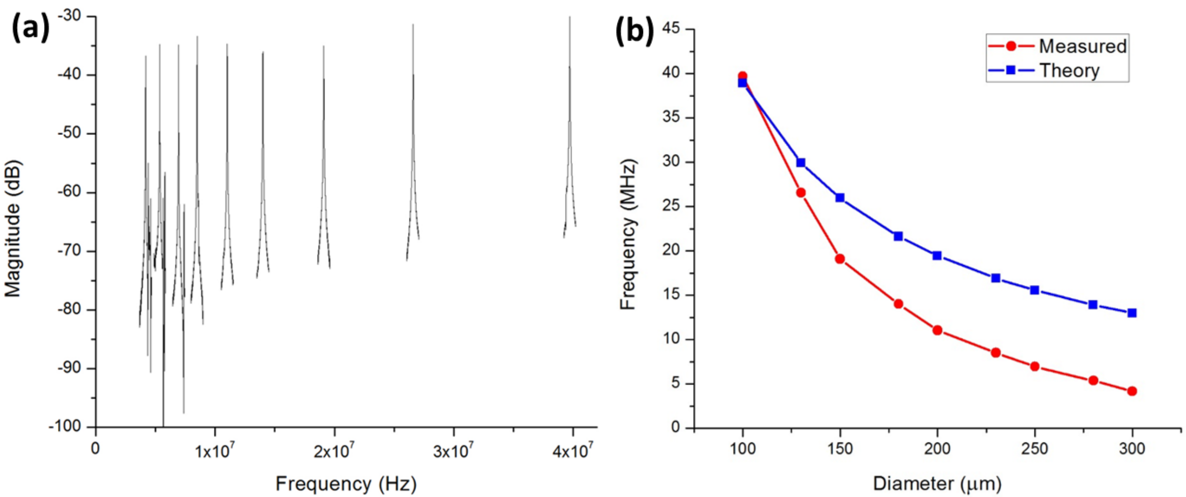

Figure 4.19 (a) Measured s-parameters from disk resonators diameters ranging from 100 µm to 300µm; (b) Line graph comparing measured data versus theoretical predictions.

As illustrated in Figure 4.19(b), the measured frequency responses of smaller disk resonators (>150 µm in diameter) follow calculated theoretical values closer. That is because larger

www.manaraa.com

disks have more imperfections due to the lossy piezoelectric and/or the device layer. Also, it can be observed in Figure 4.19(a) that the insertion loss from the devices becomes smaller as the diameter of the resonators gets larger which corresponds to larger R_m values. This happens because the larger electrodes and material imperfections introduce mass loading effects in the electrical characteristics of the device.

Plate lateral mode resonators were designed by matching the top electrodes to the FEM COMSOL Multiphysics ® rendered maximal displacement areas and strain fields renderings. Due the complexity of plate lateral extensional mode shapes (either width-extensional or length-extensional mode) obtained from the total displacement COMSOL® mode simulation, the strain field if often used instead.

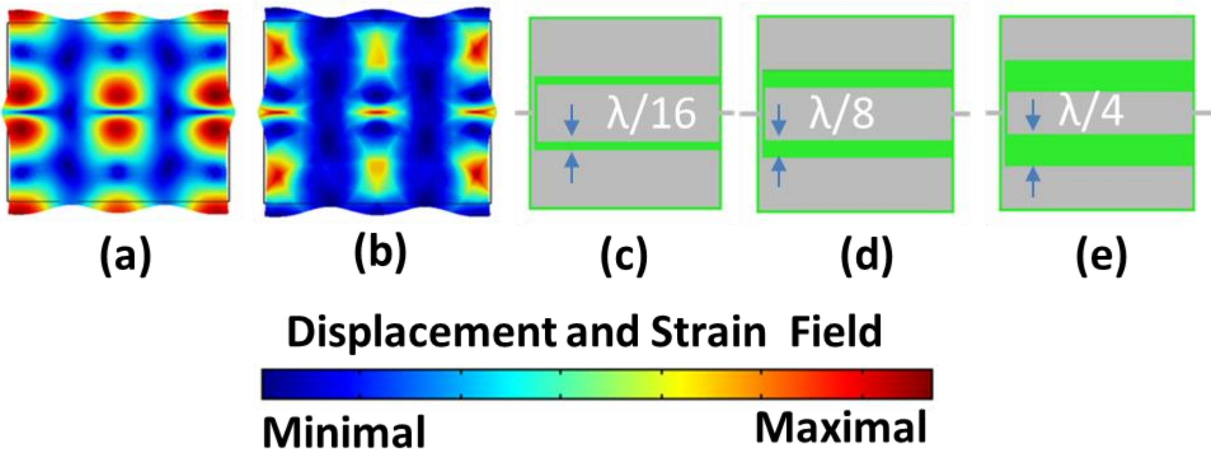

Figure 4.20 Top electrode design for a N3 length-extensional mode square plate resonator using (a) total displacement; (b) strain field rendering from COMSOL® FEM simulation; and top electrode spacing design with (c) λ/16, (d) λ/8, and (e) λ/4 of electrode-to-electrode spacing.

A novel electrode spacing design following surface acoustic resonator (SAW) interdigital transducer (IDT) design concept [53, 54] was performed to match the intended N3 contour resonant mode as shown in Figure 4.20. For this design, λ, is the wavelength obtained from the equivalent acoustic velocity (C_{ql}) at resonance as shown in equation (2.32). This technique

www.manaraa.com

accompanied with total displacement and/or strain field rendering from COMSOL® FEM, which is used to minimize the d_{31} of ZnO and obtain a stronger frequency response with low motional resistance values as demonstrated by equation (4.1).

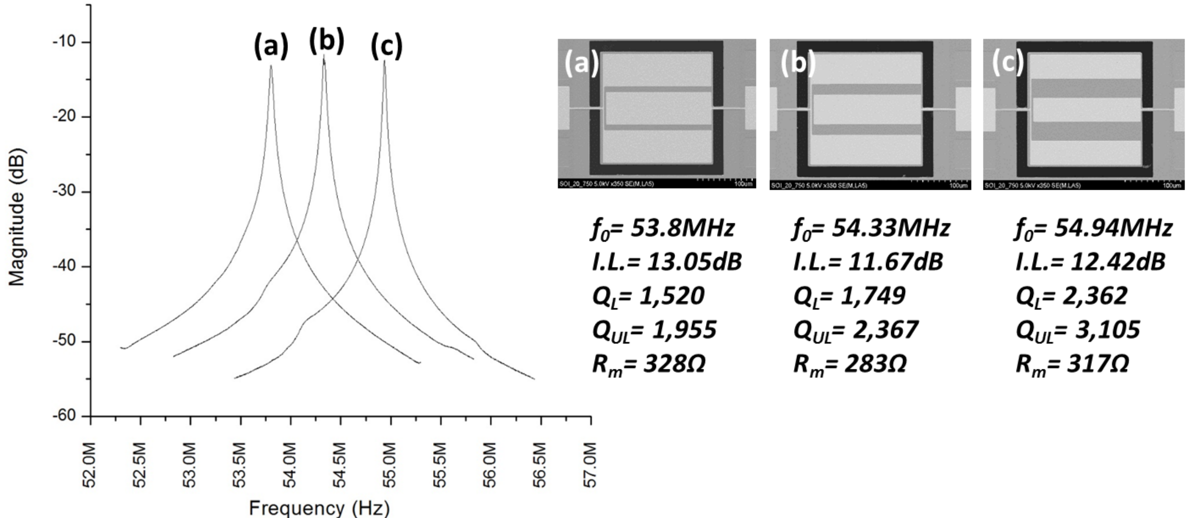

Figure 4.21 Measured transmission responses of a 200 µm square plate resonator in N3 length-extensional mode with top electrode spacing design of (a) λ/16; (b) λ/8; and (c) λ/4.

Figure 4.21 shows that the R_m is lower when the top electrode-to-strain field matching has an electrode spacing of λ/8. It can also be observed that in order to reduce the top electrode spacing for the three designs as shown in Figure 4.21, the electrode width was reduced thus creating an overall smaller electrode. Therefore, the captured s-parameters show that the smaller the electrode area is, the higher the resonant frequency. This happens because of the mass loading effects from the larger electrodes.

One more approach to maximize the transduction mechanism of the piezoelectric devices is described in Figure 4.22. Here, it can be observed that three designs of top and the bottom electrodes used to match the strain field were created. The first design shown in Figure 4.22(a) is the most common design used for TPoS resonators, and only the top electrode is designed to match the strain field. In Figure 4.22(b), novel design to maximize the surface area is presented while the

المنارة للاستشارات
www.manaraa.com

bottom electrode matches the strain field. This design is intended for devices where functionalization technology relies on a large surface metal area such as ELISA [55]. For the third design presented in Figure 4.22(c), both the top electrodes and the bottom electrodes were designed to match the strain field to maximize the transverse piezoelectric coefficient (d_{31}) of ZnO thin film.

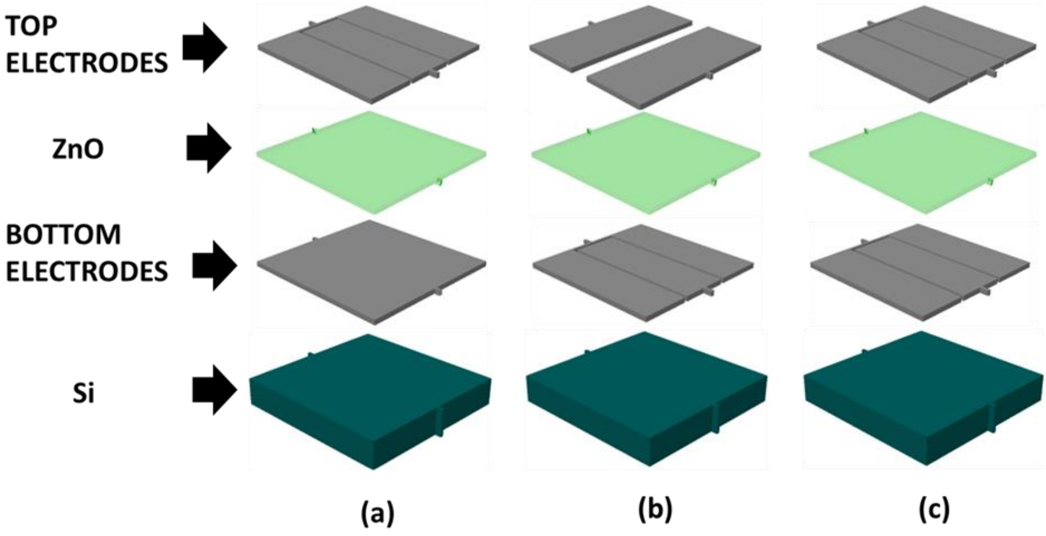

Figure 4.22 3D models of three different electrode design created to match the strain field: (a) Top-electrode matching; (b) bottom electrode matching; and (c) top-and-bottom electrode matching.

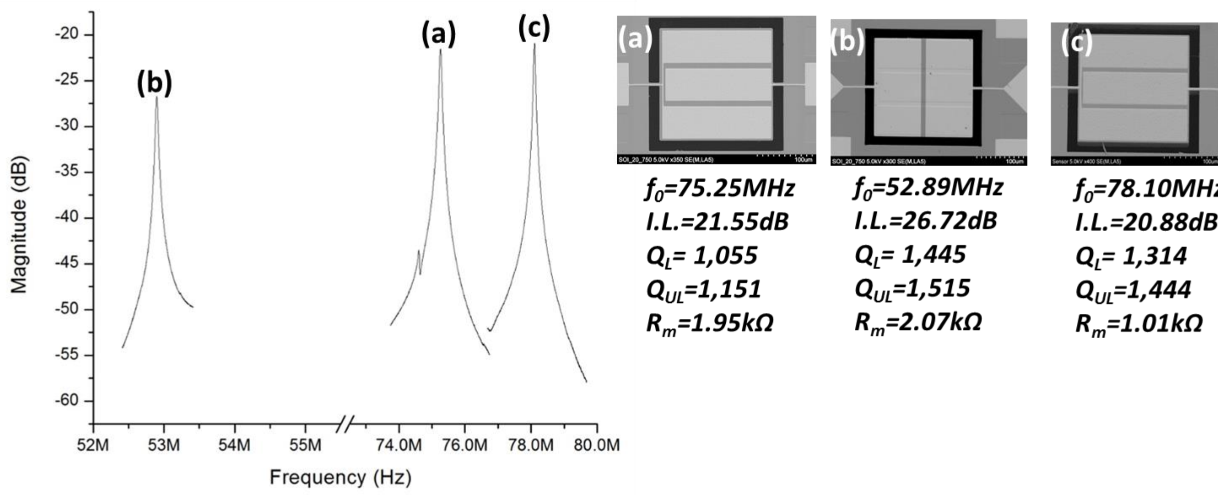

Figure 4.23 Measured S-parameters of a 150 μm square resonators in its N3 length-extensional mode with three different electrode design created to match the strain field: (a) Top-electrode matching; (b) bottom electrode matching; and (c) top-and-bottom electrode matching.

المنارة للاستشارات
www.manaraa.com

The electrode design that best matches the strain field and gives the strongest signal transduction is the top-and-bottom electrode matching configuration as seen in Figure 4.23 (c). As both the top and the bottom electrodes match the strain field, the lowest motional resistance value of 1.01 kΩ is obtained which is almost 1 kΩ lower than the other two designs. The resonant frequency is also slightly higher because the combined electrode area from the top and bottom electrodes is smaller than the other two designs. One important fact about electrode design as shown in Figure 4.23 (b), is that strongest frequency response is no longer happening at N3 width-extensional mode because the top electrode design is exciting a different resonant mode. However, the frequency and electrical characteristics of this mode are still very interesting, especially if the targeted mass sensing application needs a large capturing area.

As illustrated in equation (4.1), the electrode width/length ratio is a very important parameter that can be used to design devices with lower R_m values. For this work, a N3 width-extensional mode was used. Therefore, the width was kept constant at 96 µm, while different length values were investigated. According to equation (4.1), the mechanical coupling of a width-extensional resonator is increased by enlarging the length of the top electrodes.

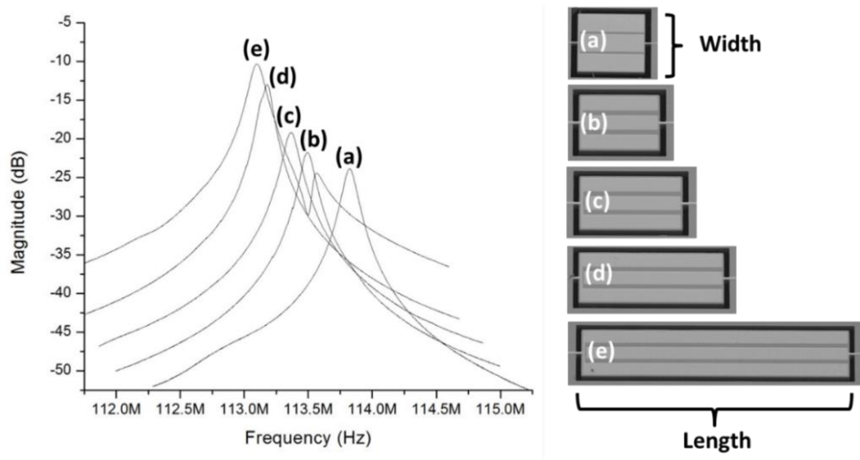

Figure 4.24 Measured forward transmission frequency responses of a N3 96µm-width extensional mode with five different W/L ratios: (a) W/L=1; (b) W/L=0.8; (c) W/L=0.6; (D) W/L=0.4; and (E) W/L=0.4.

المنارة للاستشارات
www.manaraa.com

In this work, designs (a)-(e) have been investigated as seen in Figure 4.24. As the length of the top electrodes is increased, the R_m value is significantly reduced as shown in Table 4.2. This happens because there is a stronger electromechanical coupling between the electrodes and the piezoelectric layer. The measured R_m value of 1.46 kΩ from a square plate resonator design with a W/L=1 ratio was decreased to 228 Ω using a rectangular plate design with a W/L= 0.2 ratio. The resonant frequency was kept around 113 MHz for all the devices because the top electrode design was meant for a N3 width-extensional mode response as described in section 4.1. Therefore, by increasing the length of the resonator plate body along with the length of the top electrodes only affects the electromechanical coupling of the device but not its resonant frequency. This is important since it that gives the designer the freedom of only changing the R_m value for impedance matching purposes without affecting the designed resonance frequency. However, as a mass sensor, this approach has its drawbacks. As shown in equation (2.34), the equivalent mass (M_{re}) of the sensor becomes larger as the area of the resonator is enlarged, which also lowers the sensitivity as illustrated in equation (2.42).

Table 4.2 Frequency Responses of a 96µm-wide Rectangular Plate Resonator Operating in N3 96 Extensional Mode with Different W/L Ratios.

W=96µm					
Ratio (W/L)	1 (A)	0.8 (B)	0.6 (C)	0.4 (D)	0.2 (E)
f_o (MHz)	113.8	113.5	113.4	113.2	113.1
I.L. (dB)	23.88	21.74	19.18	12.95	10.32
Q_L	1,010	1,024	1,001	1,100	990
Q_{UL}	1,079	1,115	1,125	1,420	1,424
R_m (Ω)	1,460	1,120	809	344	228

Another important technique is to reduce the motional resistance of a resonant device is by choosing a higher order contour mode design as illustrated in equations (4.1) and (4.4) [22],

www.manaraa.com

$$R_{1,N} \approx \frac{R_m}{n} \tag{4.4}$$

where n=N for even number of top electrodes N (i.e., mode N3 means that it has 3 split top electrodes matching a specific mode), and n = $(N^2\text{-}1)/N$ for odd N.

This implies that at higher modes, the motional impedance decreases by the number of top electrodes needed. In order to investigate this phenomenon, three high-order designs were created. The results for higher order-modes N3, N5 and N9 are shown in Figure 4.25. It can be observed that for every design, the matched resonant frequency exhibits the lowest R_m value. In addition, a 40 MHz to 170MHz frequency spectrum presented shows all the excited spurious and harmonic modes where width-extensional harmonic modes have been identified. The rest of frequency responses are length-extensional and off-plane resonant modes.

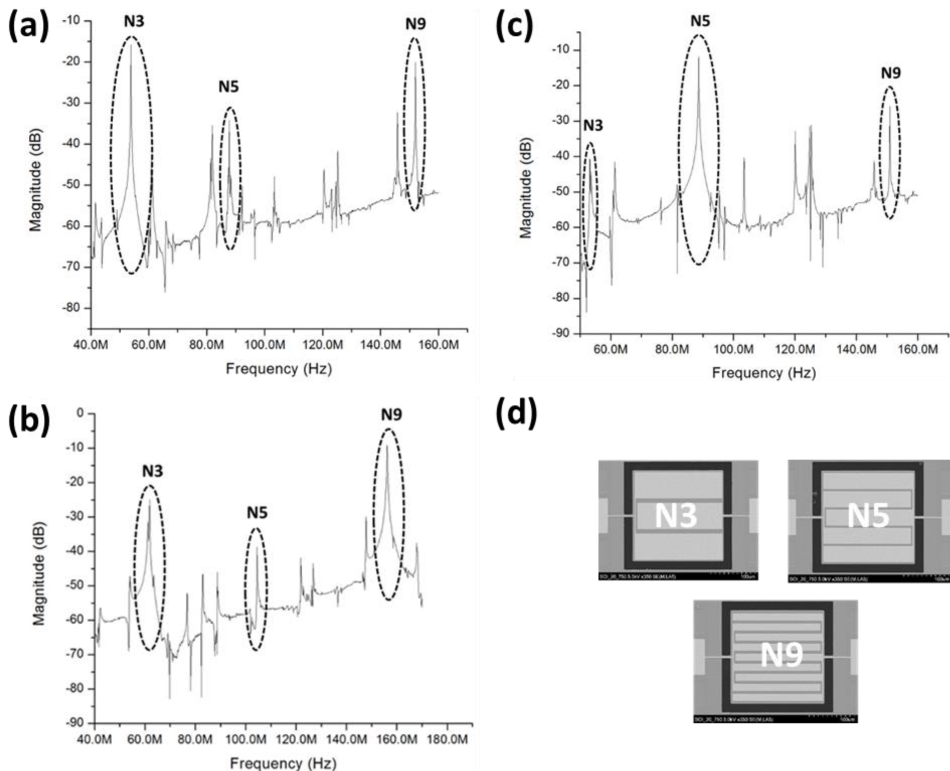

Figure 4.25 Measured forward transmission frequency responses for square plate higher order mode 150μm-length extensional resonator designs: (a) N3; (b) N5; (c) N9; and (d) SEM images of electrode configuration for N3, N5, and N9.

www.manaraa.com

As observed in Table 4.3, R_m values as low as 169 Ω can be obtained from the N9 length-extensional mode. The designs presented in Figure 4.25 did not exceed motional resistance values of 228 Ω with loaded Q factors as high 1,500, which makes this technology a strong candidate to be a very powerful mass sensor. In addition, great electrical and frequency responses can be obtained from harmonic modes such as design N3 with an N9 harmonic as shown in Figure 4.25 (a). The strong N9 harmonic lateral-extensional mode has a motional resistance value of 714 Ω and a loaded Q of 3,010 at 152.04 MHz. In Figure 4.25 (c), a N5 design with an N9 harmonic mode has an R_m value of 1.18kΩ and a loaded Q factor of 4,795 at 150.9 MHz. Also, a few harmonic modes have been measured with resonant frequencies as high as 776 MHz with loaded Q factors of 2,000 as shown in Figure 4.26. The amazing electrical and frequency characteristics of the harmonic modes mentioned above are very useful for the development of ultrasensitive resonators.

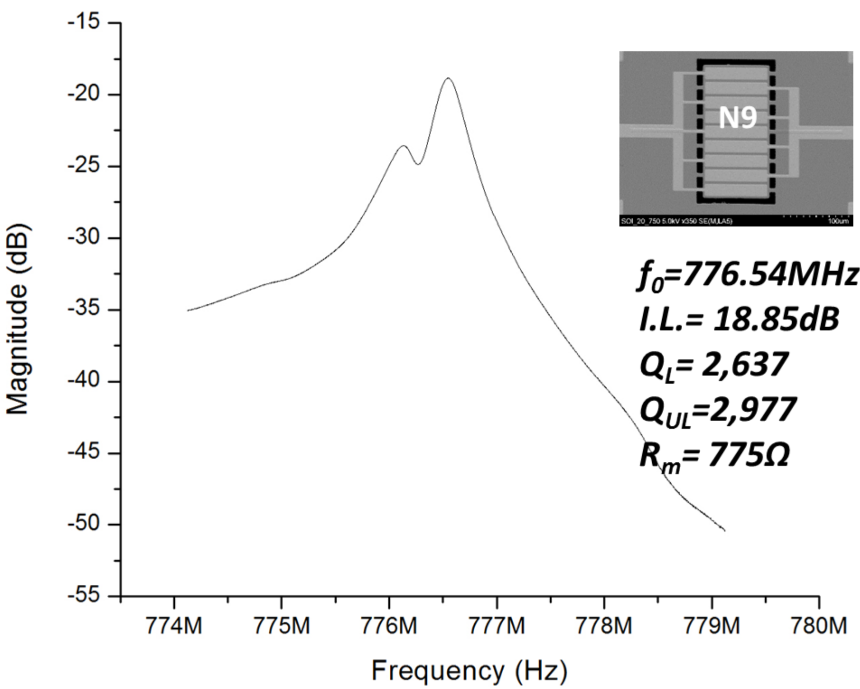

Figure 4.26 Measured transmission frequency response of a strong 29th 150 μm-width extensional harmonic response from a N9 design.

المنارة للاستشارات
www.manaraa.com

Table 4.3 Frequency Responses of a 150 µm-length Extensional Square Plate Resonator Designs.

Width (µm)	150								
Design	N3			N5			N9		
Mode	N3	N5	N9	N3	N5	N9	N3	N5	N9
f_o (MHz)	53.8	87.77	152.04	53.2	88.61	150.9	61.85	104.52	156.13
I.L. (dB)	13.05	33.14	18.22	37.21	9.46	22.21	24.54	37.23	8.62
Q_L	1,520	1,362	3,010	886	1,254	4,795	491	1,831	835
Q_{UL}	1,955	1,393	3,431	899	1,890	5,198	522	1,857	1,327
R_m (Ω)	228	4440	714	7,150	197	1180	1,590	7,170	169

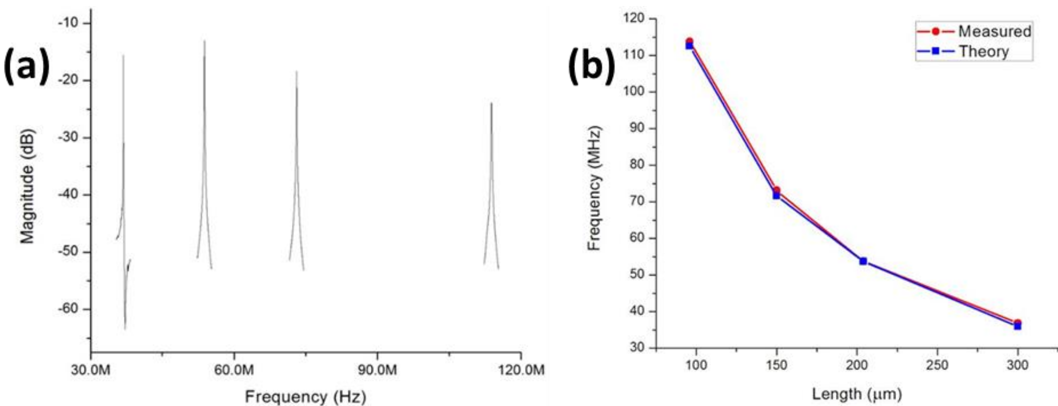

Figure 4.27 (a) Measured forward transmission frequency responses from ZnO-on-Si square plate resonators with lengths ranging from 96 µm to 300 µm; (b) Line graph comparing measured data versus theoretical approximations.

In order to be able to correctly predict the frequency response of ZnO-on-Si lateral-extensional mode resonators, a direct comparison between theory and measured data needs to be done. The theoretical approach follows the equations covered in section chapter 2 and the measured data was obtained from a set of N3 length-extensional square plate resonators with lengths ranging from 96 µm to 300 µm as shown in Figure 4.27 (a). The theoretical approach matches the measured values to perfection, making lateral-extensional modes the most reliable design, as shown in Figure 4.27 (b). Also, larger devices have smaller R_m values of as seen in Figure 4.27 (a), which also agrees with equation (4.1).

www.manaraa.com

4.10 Pre-released Thin-film ZnO-on-Polysilicon Resonators

The resonators reported in this section are based upon a 750 nm thin-film ZnO on a 6.5 μm Polysilicon device layer from a Polysilicon SOI wafer. The microfabrication steps are illustrated in Figure 4.3 and the devices were released with the oxide pre-releasing technique illustrated in Figure 4.9. The custom-made poly-SOI wafers were fabricated in the nanotechnology research and education center (NREC) cleanroom facility at USF. The starting substrate was a high resistivity Si wafer to minimize the device cross-talk, also known as the substrate feedthrough. Then, a 5 μm PECVD SiO_2 was deposited as the sacrificial layer. Finally, a 5 μm LPCVD stress-free polycrystalline silicon film is deposited at 580 °C by a LPCVD furnace.

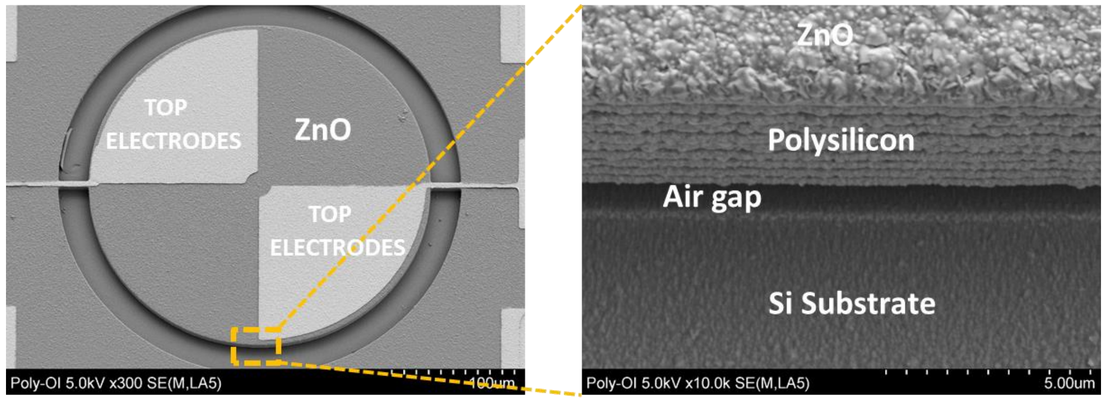

Figure 4.28 SEM top-view and cross-sectional views photos of a 1st contour mode thin-film ZnO-on-polysilicon contour mode disk resonator after fabrication.

The devices were successfully released as shown in Figure 4.28, and they were also tested using the test set-up configuration described in section 4.6. In Figure 4.30 (a), the results for a fundamental 30μm-radius disk contour mode resonator were obtained with R_m value of 12.4 kΩ and a loaded Q of 2,895 at 45.69 MHz. As covered in chapter 3, the R_m value is too high to be directly integrated with commercially available technology, but the loaded Q factors at resonance are comparable to those of ZnO-on-Si devices covered in section 4.9. The motional resistance can be decreased by optimizing the polysilicon device layer. As seen in Figure 4.29, the deposited

www.manaraa.com

polysilicon exhibits a non-ideal crystal structure according to the XRD and AFM results compared to other published work [56]. Also, the polysilicon layer used for these devices was not doped nor post-annealed ,and it exhibits s sheet resistance of 1.354-1.748 Ω/□ compared to 0.001 Ω/□ of the heavily boron doped SOI device layer. Therefore, it is possible to achieve similar electrical responses to ZnO-on-Si devices using home-made Poly-SOI substrates after the polysilicon has been properly characterized.

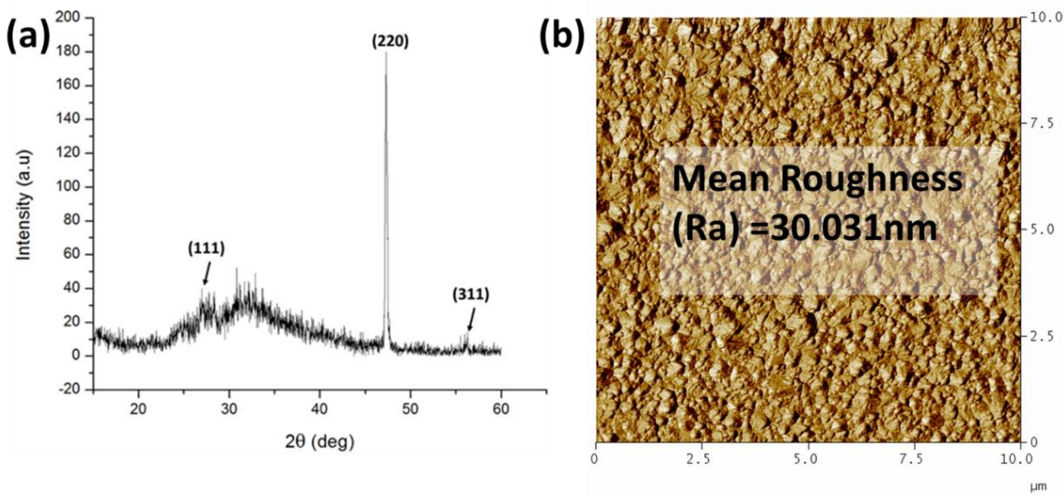

Figure 4.29 (a) XRD and (b) AFM results of the LPCVD polysilicon layer of the home-made poly-SOI substrate.

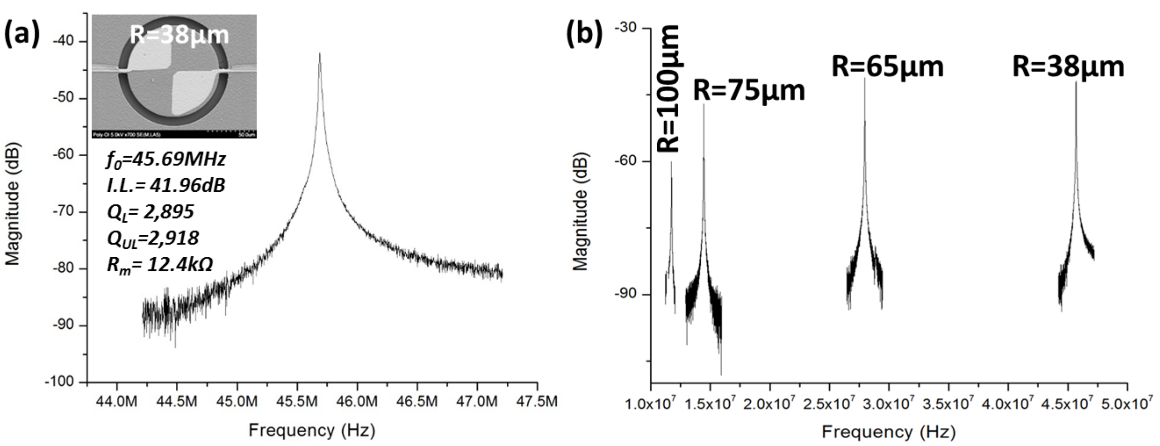

Figure 4.30 Measured forward transmission frequency responses for ZnO-on-PolySi 1st contour mode disk resonators with different radiuses for: (a) 38 µm-radius disk 1st contour mode; (b) frequency response of 1st contour mode disk resonators with different radiuses.

المنارة للاستشارات
www.manaraa.com

Similarly to ZnO-on-Si, ZnO-on-polysilicon length-extensional modes also exhibit smaller R_m values compared to disk contour mode resonators. As shown in Figure 4.31, a 60 µm-width extensional N3 rectangular shaped resonator exhibits an R_m value of 6.54 kΩ with an unloaded Q factor of 1,617 at 252.37 MHz. The temperature coefficient of frequency (TCF) of the devices was measured in a temperature range of 25°C to 105°C [57], as shown in Figure 4.32 (b).

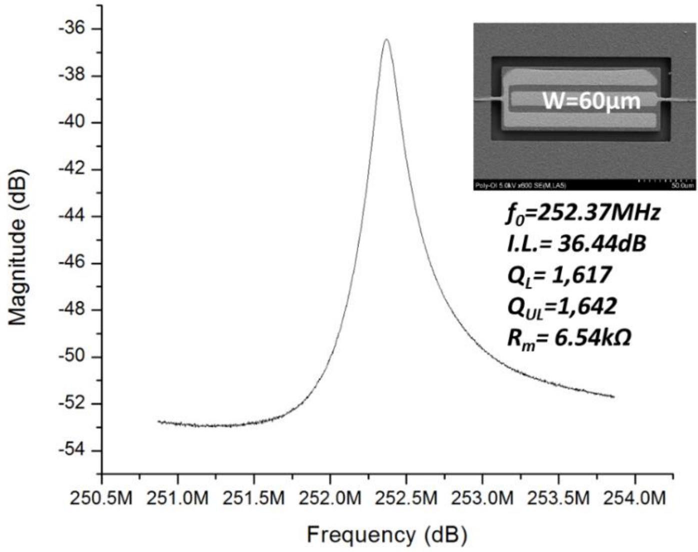

Figure 4.31 Measured forward transmission frequency response of a ZnO-on-PolySi 60 µm-width extensional N3 rectangular shaped resonator.

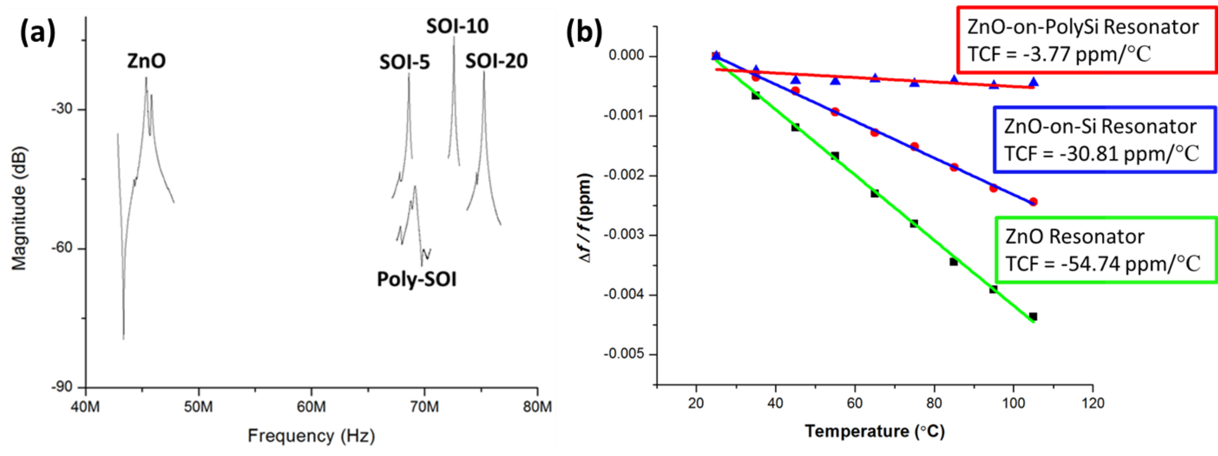

Figure 4.32 (a) Measured forward transmission frequency response; and (b) TCF comparison of structural layers fabricated in this work using 150 µm-length extensional mode square plate resonators.

المنارة للاستشارات
www.manaraa.com

Table 4.4 Device Structural Layer Comparison Using 150 μm-length Extensional Mode Square Plate Resonators.

Wafer I.D.	Coupling Device Layer	ZnO Thickness (nm)	Device Layer Thickness (μm)	Measured C_{ql} (ms^{-1})	Theoretical C_{ql} (ms^{-1})	Average Q_l Factor
Poly-SOI	LPCVD Poly	750	7	6,912	6,792	243
SOI-5	Single Crytal Si	500	5	6,855	6,417	1,055
SOI-10	Single Crytal Si	750	10	7,311	7,153	1,497
SOI-20	Single Crytal Si	750	20	7,524	7,707	1,512
ZnO	-	750	-	4,452	4,655	401

The measured TCF of -3.77 ppm/°C for ZnO-on-polysilicon resonator is the lowest reported value for uncompensated ZnO-on-Substrate resonators up to date. This is due to the high temperature needed to deposit this film, which helps its crystal structure and material properties to be more stable at temperatures ranging from 25°C to 105°C. Therefore, polysilicon is a good alternative to single crystal Si, because the devices' frequency response and electrical behavior is on par with the exception of the motional resistance that can be improved by characterizing the polysilicon layer.

4.11 TPoSCRE Released Thin-film ZnO-on-Si Resonators

The resonator reported in this section are based upon a 750 nm ZnO thick-film on a 3-10 μm single crystal Si device layer of a 4 kΩ Si wafer. The fabrication steps are illustrated in Figure 3.3 and the TPoSCRE release technique used for these devices is illustrated in Figure 4.10. First, a 20 μm HAR DRIE Si etch follow by a 30 nm Al_2O_3 ALD layer are done to define the device layer as shown in Figure 4.33 (c) and (d). The substrate was chosen to be a 4 kΩ-high resistivity Si wafer in order to minimize the device cross-talk. The devices were successfully fabricated and released as shown in Figure 4.33. This is the first time TPoS resonators are fabricated without using SOI wafers. However, still a few parameters need to be addressed to have a higher yield such as new releasing process parameters [58]. The fabricated devices exhibit loaded Q factors as

www.manaraa.com

high as 919 and R_m values as low as 9.3 kΩ. Figures 4.30 (a) and (b) show that different size resonators will have different device layer thicknesses due to the inconsistency of the dry releasing process used.

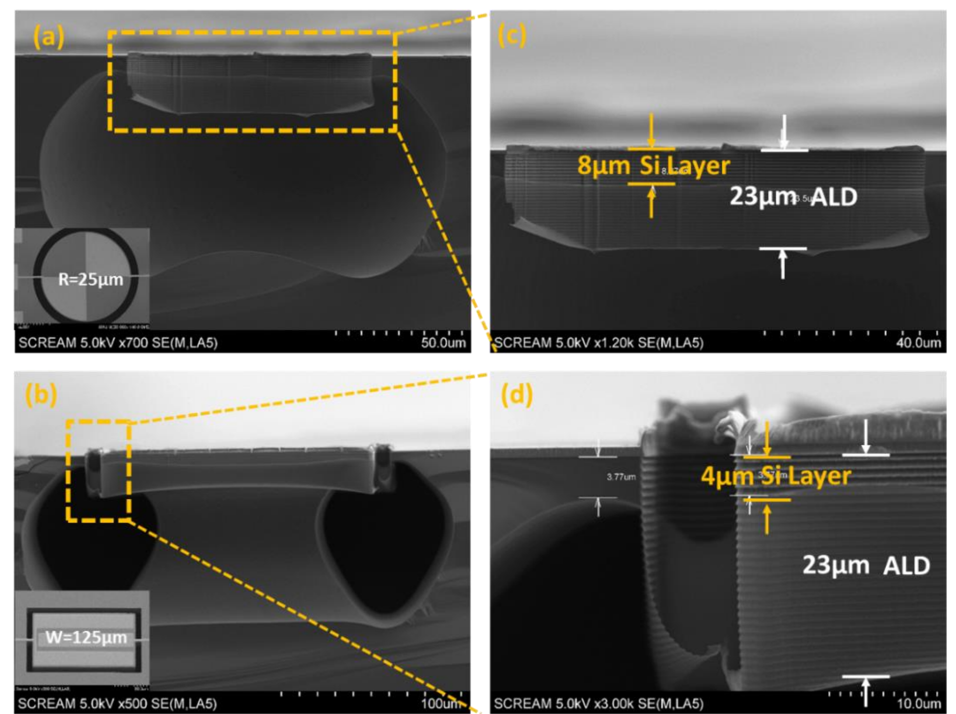

Figure 4.33 SEM cross-sectional view photos of released devices using the TPoSCRE technique: (a) 25 µm-radius disk resonator with a (b) device layer of 8 µm and (c) a unreleased rectangle resonator with a device layer of 4 µm using the 2 hours of anisotropic DRIE SF_6 release dry etch.

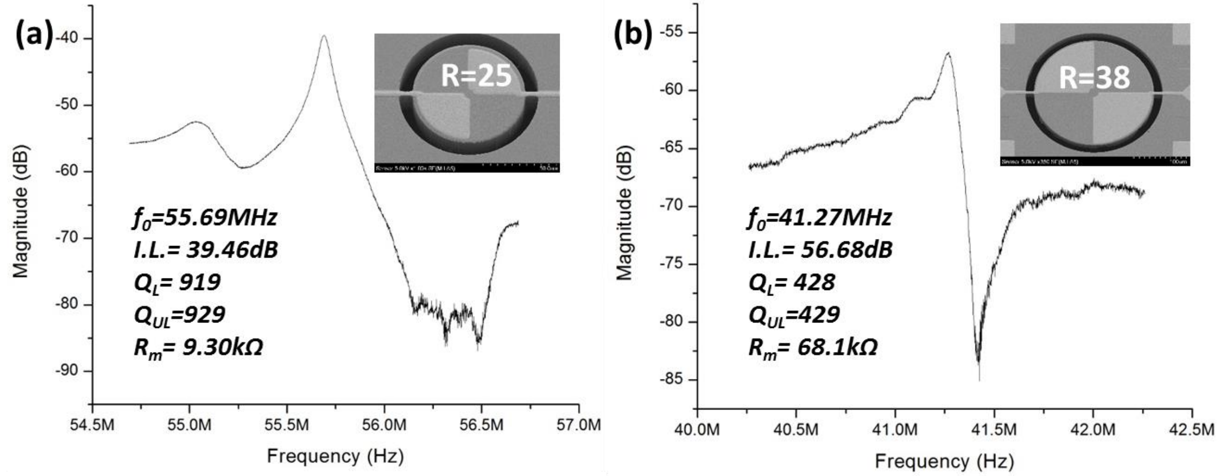

Figure 4.34 Measured forward transmission frequency responses TPoSCRE released 1st contour disk resonators with a radius of (a) 25 µm and (b) 38 µm.

www.manaraa.com

CHAPTER 5 MASS SENSOR DEVELOPMENT

After the devices were fabricated and tested as described in chapters 1-4, the electrical and frequency characteristics were thereafter extracted. To be able to compete with the most sensitive devices ever reported up to date as shown in Table 1.2, a small yet powerful device was selected as shown in Figure 5.1. The device was designed using a 1st extensional contour mode ,but as described in section 4.9, one of its harmonic modes, the 4th extensional contour mode, exhibited remarkable electrical and frequency characteristics as shown in Table 5.1. Using such characteristics allows the best possible sensitivity and resolution of TPoS resonators. The device selected is composed of a 20 µm low resistivity single crystal structural layer and a 600 nm-thick ZnO piezoelectric layer. The top and bottom electrodes are made of platinum and it was pre-released with the oxide pre-released technique illustrated in Figure 4.9. The device was tested in both vacuum and air environments, where the mass sensing characteristics of the maximal and minimal displacement areas were extracted and analyzed.

5.1 Wire-bonding of ZnO-on-Si Resonator for Vacuum Testing

To test the device in a vacuum environment, a chip carrier was fabricated and the device was wire-bonded to it. The chip carrier was designed by using Advance Design Systems (ADS) 2012 and the board was milled using a LPKF ProtoMat S62 milling machine. The chip carrier was created by using a FR-4 substrate, then SMA connectors were soldered to the terminals to connect it to the VNA. Thereafter, the device was wire-bonded to the chip carrier with the use of K&S 4524 gold ball bonder. Then, it was tested in air using chip-carrier configuration seen in the indented picture in Figure 5.1. Both the GSG (on-chip probing) and the wire-bonded (on-carrier

للاستشارات المنارة
www.manaraa.com

chip) frequency and electrical parameters were extracted. As observed in Figure 5.1, the chip-carrier introduces parasitic to the overall performance of the device compared to direct GSG on-wafer probing. For this particular case, the introduced parasitics did not significantly affected the overall performance. As seen in Table 5.1, the R_m decreased from 6.5 kΩ to 4.4 kΩ and loaded Q factor increased from 5,891 to 6,967 after wire-bonding. As demonstrated in Table 5.2, the chip-carrier introduced a C_f of 7 *f*F, but the other electrical parameters were barely affected by this change, as the resonant frequency remained the same.

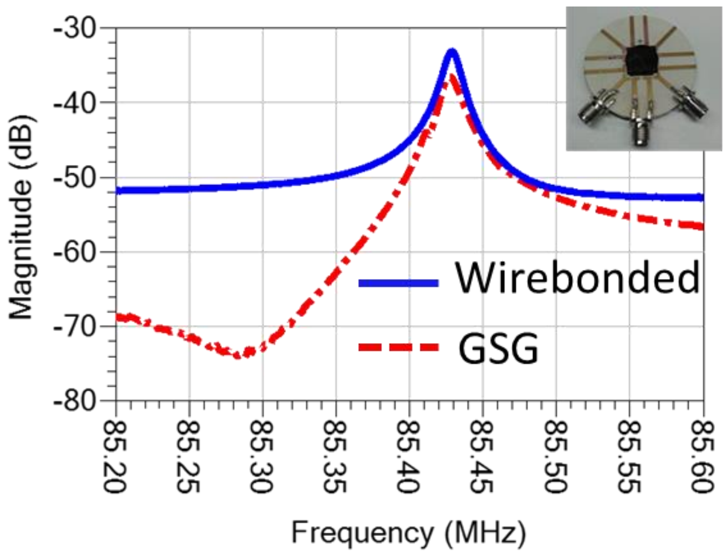

Figure 5.1 Measured frequency responses from GSG on-wafer probing and wire-bonded measurements in air.

Table 5.1 Frequency and Electrical Characteristics in Air of GSG and Wire-bonded Measurements.

R=40μm, 4th Mode		
Measurement	**GSG**	**Wirebonded**
***f_o* (MHz)**	85.43	85.43
I.L. (dB)	36.49	33.08
Q_L	5,891	6,967
Q_{UL}	5,980	7,125
R_m (Ω)	6,576	4,411

www.manaraa.com

Table 5.2 Electrical Parameters Extracted from the Measured Devices Through GSG on-Wafer Probing and Wire-bonded Approaches.

R=40µm, 4th Mode		
Measurement	GSG	Wirebonded
$R_m (\Omega)$	6,576	4,411
$C_m (fF)$	0.028	0.042
$L_m (H)$	0.122	0.082
$C_f (fF)$	7.9	15
C_{od} & $C_{od} (fF)$	10	10

5.2 Theoretical Sensitivity and LOD Determination

The device was then tested in vacuum using a test set-up illustrated in Figure 5.2 (a), where the frequency and electrical characteristics were measured as shown in Figure 5.2 (b). It can be observed that the R_m decreased form 4.4 kΩ to 3 kΩ and the loaded Q factor increased from 6,967 to 10,638 by operating in vacuum instead of atmospheric environment.

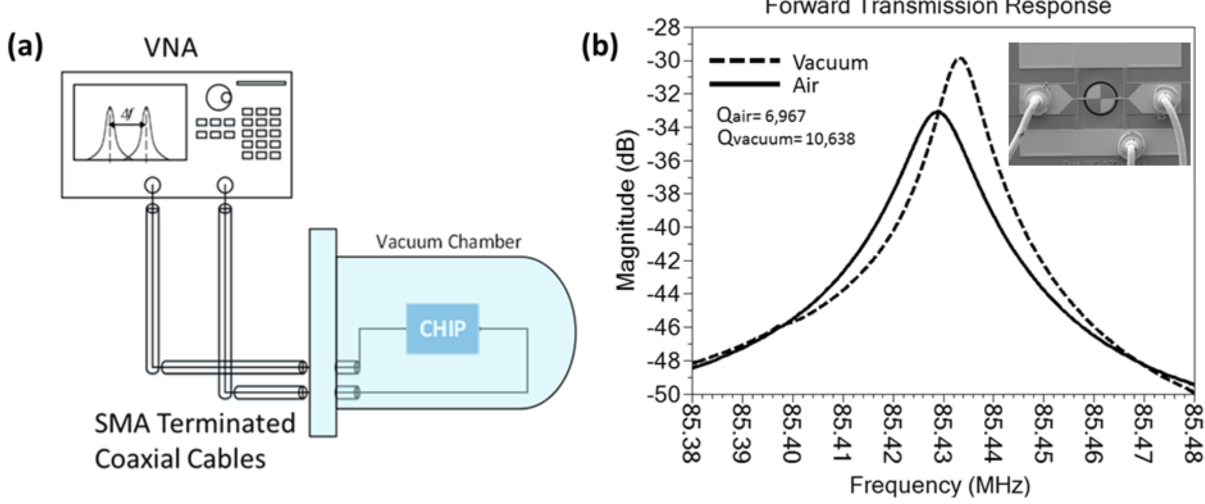

Figure 5.2 Illustration of (a) the vacuum test-set up and the measured forward transmission frequency responses (b) the measured resonant frequency and Q factors in air and vacuum.

Here it can be safely said that the electrical characteristics of this particular device are at the very best. As shown in Table 5.3, a theoretical sensitivity of 1.379 Hz fg^{-1} (1 fg = 10^{-15}g) can

www.manaraa.com

be achieved. Also an LOD of 312 ag (1 ag = 10^{-18}g) can be found by equation (2.41) using the short term noise and phase angle at resonance as shown in Figure 5.3. This dissertation proves that ZnO-on-Si devices are very strong candidates to go for commercialization.

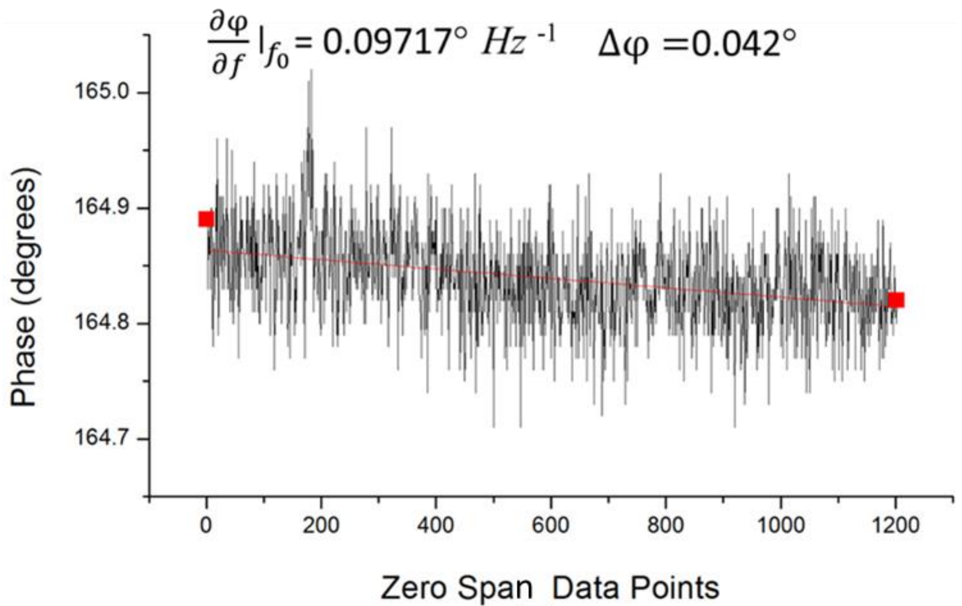

Figure 5.3 Measured zero span spectrum phase noise at the resonance frequency.

Table 5.3 Theoretical Sensitivity Analysis, and Resonator Performance Parameters in Air and Vacuum.

R=40µm, 4th Mode		
Environment	**Air**	**Vacuum**
f_o (MHz)	85.43	85.43
I.L. (dB)	33.08	29.82
Q_L	6,967	10,638
Q_{UL}	7,125	10,993
R_m (Ω)	4,411	3,000
Theoretical Sensitivity		
M_{re} (g)	3.11E-08	
Sensitivity (Hz fg^{-1})	1.379	
Δf_{noise}	0.43 Hz	
LOD (g)	3.12E-16	

www.manaraa.com

5.3 FIB Platinum Deposition Characterization

A Quanta 200 3D Dual Beam Focus Ion Beam (FIB) equipped with a Gas Injection System (GIS) was used to test the sensitivity of the device. As covered in section 2.10, the deposited mass needs to be smaller than the estimated equivalent mass (M_{re}) of 31.1 ng to precisely measure the sensitivity of the device. Multiple Platinum/Gallium/Carbon composite micro-pellet depositions were performed on gold coated substrates. The FIB was calibrated until repeatable results were obtained using a beam current of 10pA to reduce the amount of gallium contamination as shown in Figure 5.4 with the parameters listed in Table 5.3. It is important to note that even after a thorough calibration, the FIB micro-pellet deposition sizes and shapes tend to vary due to the conditions of the FIB chamber. The micro-pellet depositions were characterized by Atomic Force Microscope (AFM) where the mean volume per micro-pellet deposition was found to be 0.665 μm^3 as seen in Figure 5(a). Also, in Table 5.4 an estimated weight per deposition of 7pg is found assuming an estimated density of 10.2 g cm^{-3}. By using $C_5H_5Pt(CH_3)_3$ as an organometallic precursor, the typical FIB deposition leads to a micro-pellet that consists of C (45%–55%), O (5%), Pt (40%–50%), and Ga (5%–7%) [59].

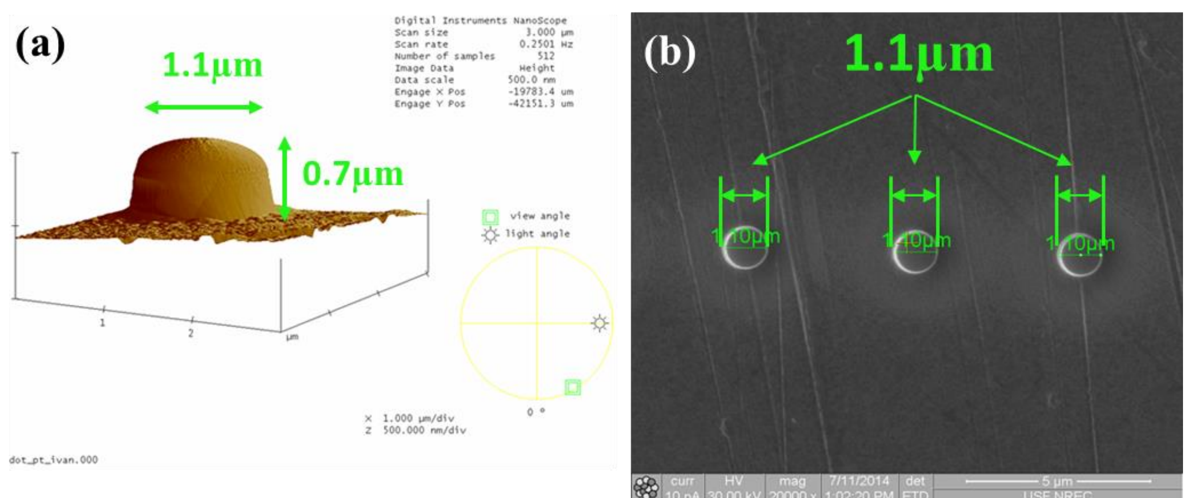

Figure 5.4 (a) AFM analysis of FIB deposited micro-pellet and (b) SEM image of multiple Pt depositions on a gold coated substrate.

www.manaraa.com

Table 5.4 FIB Settings for Platinum Deposition.

FIB Settings for Platinum Deposition	
Bean Current (mA)	10
Working Distance (mm)	15
Beam Acceleration Voltage (kV)	30
Magnification	20,000
Deposition Thickness (µm)	1
Diameter(µm)	1

Table 5.5 Analytic Results for FIB Platinum Deposition.

Analytical Resuts for FIB Platinum Deposition	
True Diameter (µm)	1.1
True Height (µm)	0.7
Average Volume (μm^{-3})	0.667
Density of Composite (g cm^{-3})	10.2
Average Weight per Deposition (pg)	7

5.4 Maximal and Minimal Displacement Area Versus Sensitivity Analysis

To test the sensitivity of the device two requirements need to be met: First, the added mass needs to be smaller than the M_{re} of the resonator. This was accomplished in section 5.3 when the FIB micro-pellet deposition was measured to be 7 pg, which is substantially smaller than the calculated M_{re} of 31.1 ng as seen in Table 5.2. The second requirement is to precisely deposit the micro-pellet on the maximal displacement areas of the resonant mode shape. As illustrated in Figure 5.4(b), the maximal displacement areas of a disk device resonating at the 4th order contour mode are found near on perimeter of the disk. The depositions need to be placed in this area to obtain the best possible sensitivity of the device. As Illustrated in Figure 5.4 (a), four different micro-pellet depositions were done on the maximal displacement areas of the device surface.

المنارة للاستشارات
www.manaraa.com

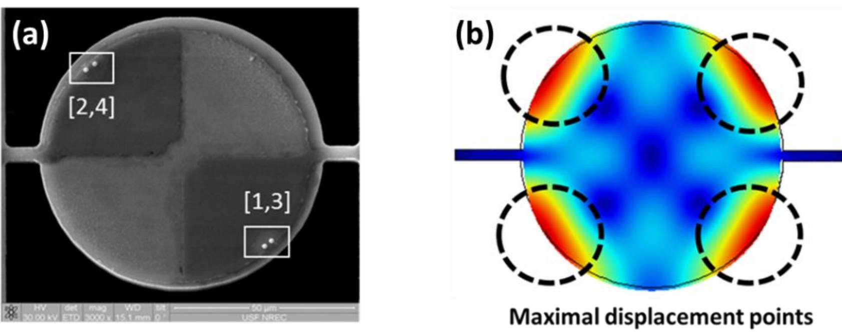

Figure 5.5 (a) SEM photo of Pt FIB deposition on the maximal displacement points; (b) COMSOL® FEM simulation of a 4th contour mode response demonstrating the placement of added mass at the maximal displacement points.

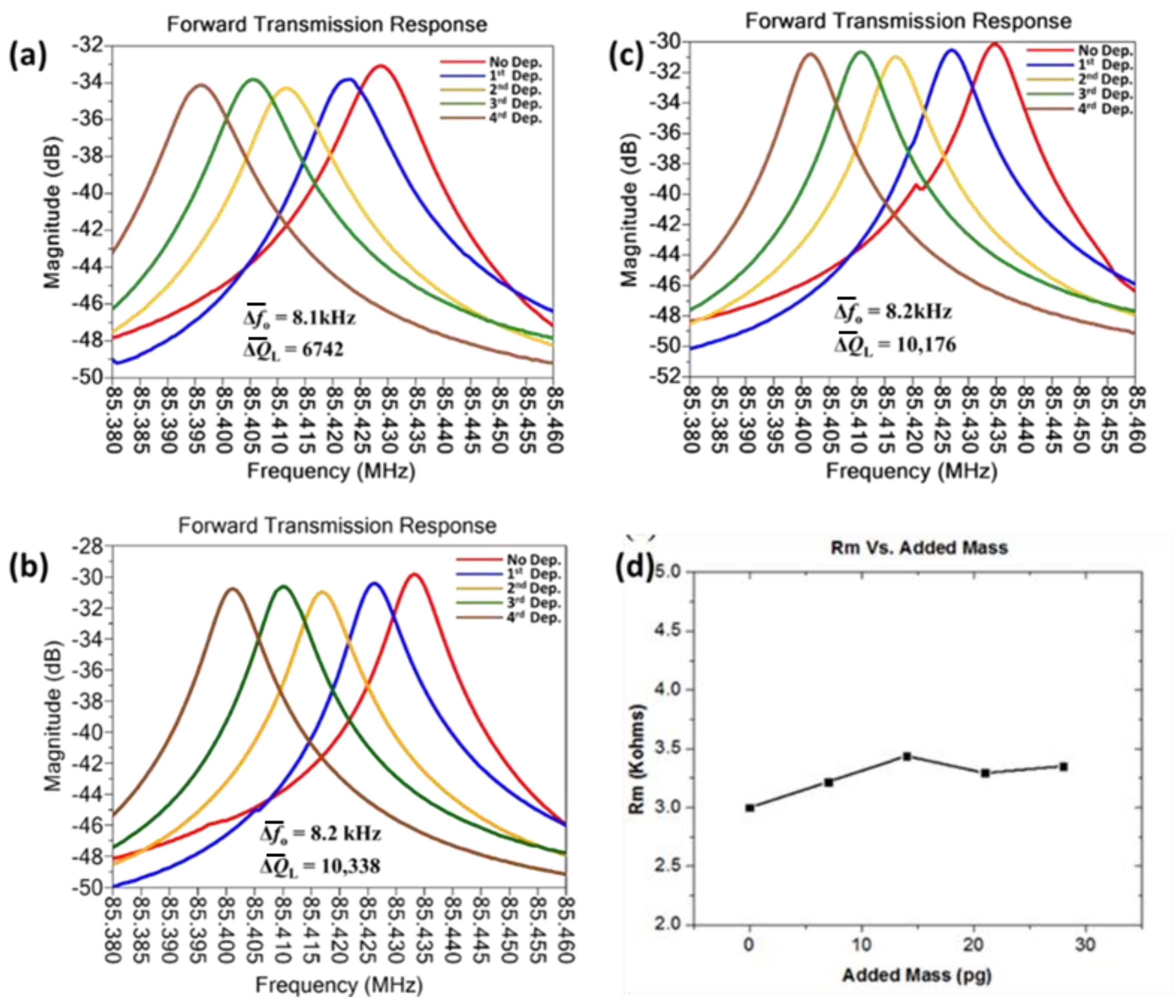

Figure 5.6 Measured forward transmission frequency responses demonstrating the frequency shift after four FIB Pt deposition on the maximal displacement points in (a) air; (b) high vacuum (>10^{-5} Torr); (c) vacuum (~10^{-3} Torr); (d) plot of R_m versus added mass in high vacuum.

المنارة للاستشارات
www.manaraa.com

The sensitivity of the device was tested in two different environments, including vacuum and air using the test-set up illustrated in Figure 5.2(a). Also, two different levels of vacuum were investigated as they presented important information needed for packaging. If the device is utilized for special sensing application under vacuum where special packaging is required, then a reference level of vacuum is needed.

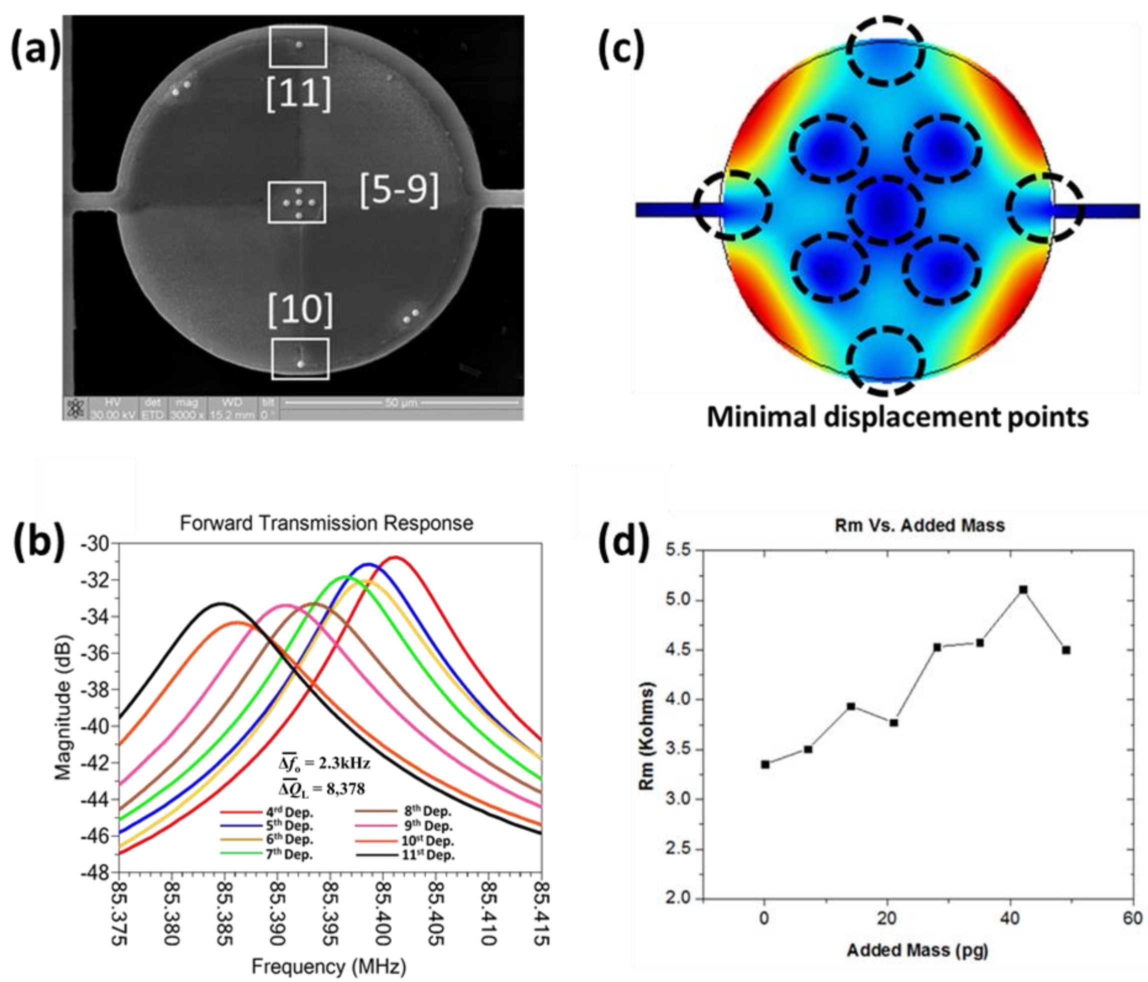

Figure 5.7 (a) SEM photo and (b) modal analysis of Pt FIB deposition micro-pellets at the minimal displacement points; (c) measured forward transmission responses demonstrating the frequency shift after FIB Pt depositions on the minimal displacement points in high vacuum (>10^{-5} Torr); (d) R_m versus added mass in high vacuum.

An important factor about these devices is the linearity of the frequency shift and the motional resistance in the maximal displacement points. Even though, a small counter balance

المنارة للاستشارات
www.manaraa.com

nonlinear effect can be observed that affects the motional resistance, but the change is very small and it tends to stay mostly linear as seen in Figure 5.6(d). A nonlinear behavior of R_m can lead to loaded Q-degradation minimizing its sensing capabilities and shorting the life of the sensor. Figure 5.6(a) shows the mass sensing behavior of the resonator in air with a sensitivity of 1.15 Hz fg^{-1}. Figures 5.6(b) and (c) demonstrate the mass sensing behavior of the resonator in two vacuum levels yielding the same sensitivity of 1.17 Hz fg^{-1} and a calculated LOD of 367ag. These values put this technology in second place just falling short to the 130ag reported value from a disk capacitive disk resonator device as seen in Table 1.2. On the nodal points of the device, it can be observed that mass loading is a large contributing factor to loaded Q factor degradation with minimum resonance frequency shift. As a consequence, a measured sensitivity of 0.334 Hz fg^{-1} and a LOD of 1,290 ag is obtained in this region. The added mass in this region affects the R_m of the vibrating disk reducing significantly the loaded Q factor of the device, thus affecting the sensor's resolution.

The nonlinear behavior of $R_{m,}$ as observed in Figure 5.7 (d), is a direct cause to Q degradation minimizing the sensing capabilities and shorting the life of the sensor. Also, the use of the entire area indiscriminately can lead to nonlinear results. In Figure 5.7, the effect of mass loading on the nodal points are shown. As it can be noticed in Figure 5.7 (c), the frequency shift and the insertion loss of the device are nonlinear. Even though, the same micro-pellet deposition parameters were used as the maximal points, the R_m sporadically increases. Also, with less than 35 pg of added mass, the loaded Q factor drops from ~10,000 to merely 6,000 causing R_m to increase 1 kΩ for depositions of 5-11 as shown.

5.5 MOF Functionalized Mass Sensors

Metal Organic Frameworks (MOFs) are highly porous crystalline materials known for their sponge like ability to capture gas molecules. Their high-surface areas make them ideal

www.manaraa.com

functionalizing layers for mass sensors because they have the ability for high gas uptake. Several research groups have investigated MOFs as sensor materials for impedimetric gas sensors with great results [60]. MOFs can also be engineered to discriminately select specific gas species depending on the composition and size of the pores. Also, the design and synthesis, structure characterization and porosity, of MOFs have been well documented [61].

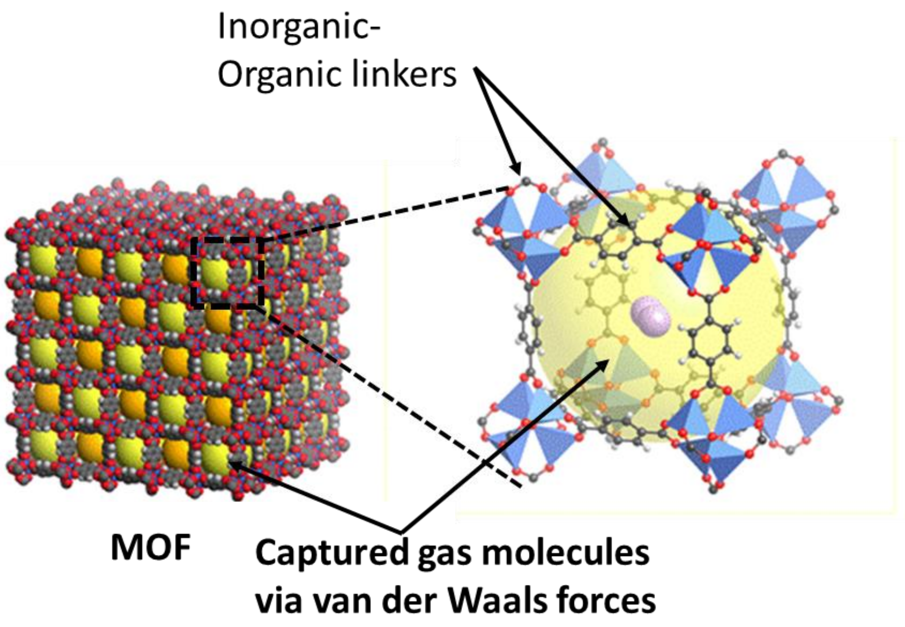

Figure 5.8 3D schematic showing the general characteristics of MOF layers delineating their gas absorption mechanisms.

For this work, in collaboration with Dr. Shengqian Ma's research group, four porous MOFs groups were synthesized as shown in Figure 5.8. Since the fabricated devices are very small (>300 μm) and the M_{re} of them is in the range of nano-grams, a small MOF crystal or a very thin layer needs to be selected. To the best of our knowledge, this is the first work where MOFs are used on a ZnO-on-Si resonator as a functionalizing element. Combining MOFs crystals and layers with the great sensitivity of ZnO-on-Si resonators, ultrasensitive sensors for gas and biological detection can be developed. Taking the advantage of the great absorption and discrimination qualities of

www.manaraa.com

MOF crystals and layers, and combining them with the unparalleled sensitivity of ZnO-on-Si resonators makes a one of the kind ultrasensitive mass sensor.

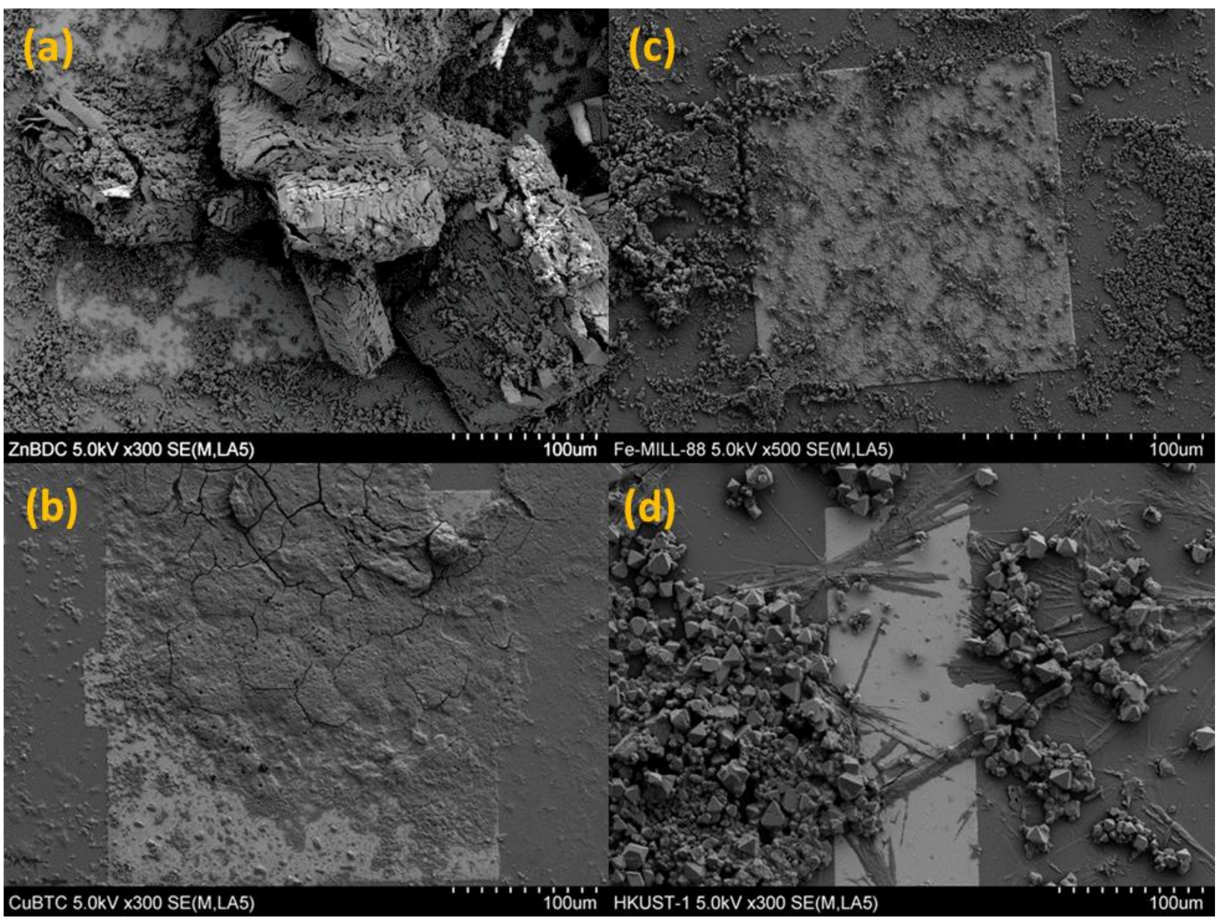

Figure 5.9 SEM images of four different MOF crystals synthetized on top to a silicon substrate with gold patterns: (a) Zn(BDC); (b) Cu-BTC; (c) Fe-MIL-88b; (d) HKUST-1.

For this work, HKUST-1 crystals were selected for our preliminary testing because, as shown in Figure 5.10 (a) and (b), they have a well-defined crystal structure and no visible size variation. The crystals were synthetized on top of Si substrates with gold pads to observe any particular growth patterns. As shown in Figure 5.9, all four synthetized MOF layer-crystals do not shown any preference to the gold pads. As delineated in section 5.4, a controllable deposition is required to be able to achieve the most accurate sensitivity reading of the mass sensor. For this

www.manaraa.com

case, a deposition of HKUST-1 crystals on the resonator, in particular on the top electrodes, is preferred.

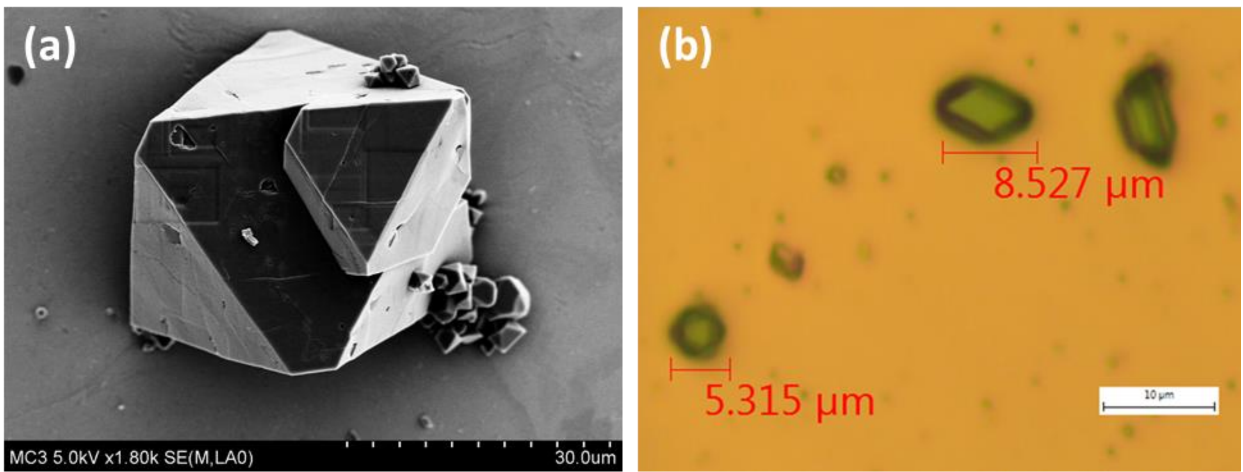

Figure 5.10 (a) SEM and (b) optical images of HKUST-1 crystals showing a well-defined crystal structure and visible size variation.

For this experiment, a N5 square plate length-extensional resonator was selected due to its unparalleled frequency and electrical characteristics as shown in Table 5.5.

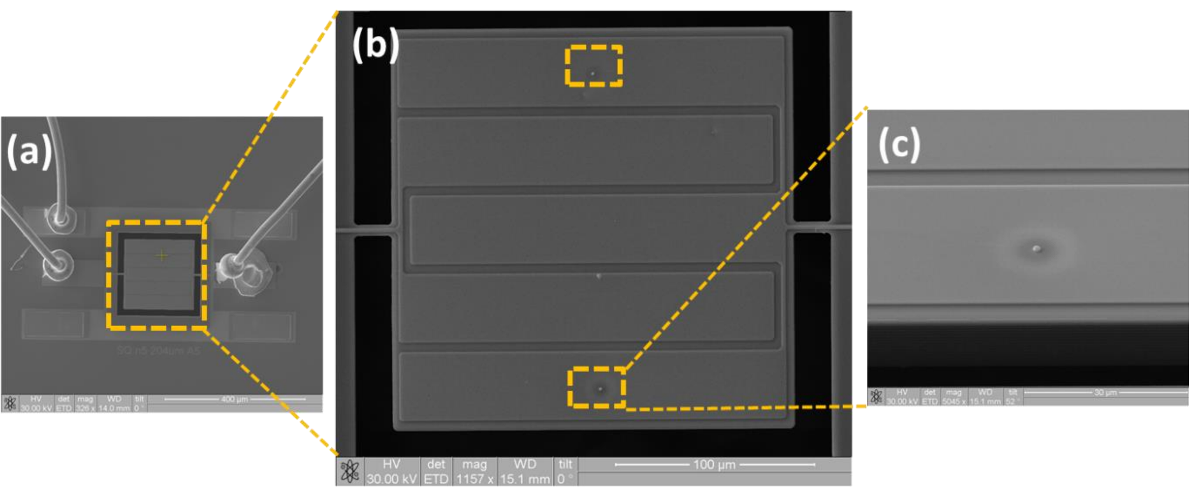

Figure 5.11 SEM images of (a) wire-bonded device, (b) the same sensor device with FIB micro-pellets for calibration; and (c) zoom view of it.

www.manaraa.com

The sensitivity of this device was obtained by measuring its frequency and electrical characteristics under vacuum using the test set-up illustrated in Figure 5.2(a). The sensitivity was estimated to be 142 Hz pg^{-1} and 242 Hz pg^{-1} for N5 and N9 frequency responses, respectively, as seen in Table 5.6. This approximation assumes that the added mass will land exactly on top of the maximal displacement area. To know the exact sensitivity of the fabricated device, two FIB micro-pellet depositions were positioned on the top electrodes of the device. Measuring the change of frequency based on the added mass of per deposition, we can extract the sensitivity of the device. As shown in Figure 5.13, the average frequency change for the two micro-pellet depositions was measured to be 726 Hz and 1,342 Hz for N5 and N9, respectively. Since the same FIB micro-pellet deposition parameters were used as shown in Table 5.2, a 7 pg of added mass per deposited micro-pellet is expected. Therefore, the measured sensitivity of the device is 103 Hz pg^{-1} and 191 Hz pg^{-1} for N5 and N9, respectively.

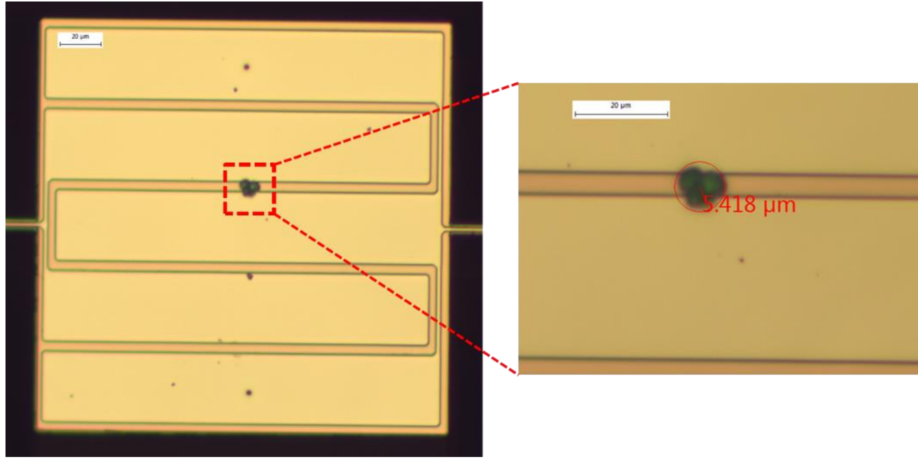

Figure 5.12 Optical images of the localized placement of HKUST-1 MOF crystals on top of a N5 width-extensional mode resonator.

The next step is to physically land HKUST-1 crystals precisely on top of the device. For this work, the crystals were selectively pick and placed on the tip of a micro-manipulator needle. Then, the needle was carefully moved towards the device (~20 µm) and then the needle was shake

www.manaraa.com

until the MOF crystal got off and landed on the resonator. As shown in Figure 5.12, a crystal cluster was successfully landed on top of the resonator.

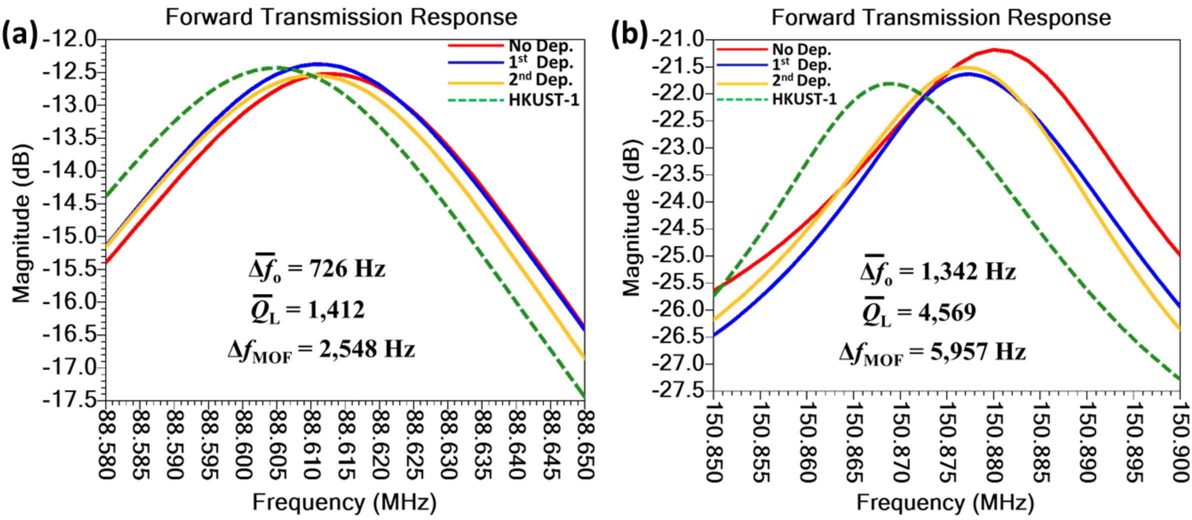

Figure 5.13 Measured forward transmission frequency responses of (a) N5 mode and (b) N9 mode demonstrating the mass sensing capabilities of a N5 width-extensional mode square plate resonator.

Ultimately, the device was tested using the set-up illustrated in Figure 4.11 under high vacuum (<10^{-5} torr). HKUST-1 crystals are known to absorb water molecules in air, but they are released out of the HKUST-1 crystals under vacuum. This allows a pure weight measurement of the deposited MOF crystals. Using the sensitivity values found for this device, the weight for a cluster of three HKUST-1 crystals (5.5 µm by 5 µm combined diameter and height, accordingly, as shown in Figure 5.12) was measured to be 24.75 pg and 31.19 pg for N5 and N9 mode resonance frequency responses, accordingly. We attribute the two different weight values to the position of the HKUST-1 crystals on the device. As observed in Figure 5.12, the HKUST-1 crystals landed between two top electrode fingers which is also adjacent to one of the nodal points for N5 mode design. Therefore, the sensitivity of the N5 mode resonance response is not optimal and the measured weight of the crystal was less than the one obtained from the N9 mode resonant response. We believe if MOF crystals would have landed on top of the electrodes the calculated weight for

www.manaraa.com

the N5 frequency response would have been closer or equal to that of the N9 mode. However, the sensitivity and resolution of the N9 will always be greater because of the higher resonate frequency and Q factor. Therefore, it is a better choice to fabricate an ultrasensitive mass sensor.

Table 5.6 150 µm-width Extensional Mode Mass Sensing Parameters.

W=150µm, N5				
Mode	N5		N9	
Enviroment	Air	Vacuum	Air	Vacuum
f_o (MHz)	88.61	88.61	150.87	150.87
I.L. (dB)	·12.98	12.52	20.41	·20.22
Q_L	1,322	1,362	3,124	4,287
Q_{UL}	1,704	1,784	3,453	4,750
R_m(Ω)	345	322	948	926
Sensitivity				
Mode	N5		N9	
Approach	Theory	Measured	Theory	Measured
M_{re} (g)	3.10E-07	4.30E-07	3.10E-07	3.93E-07
Sensitivity (Hz pg^{-1})	142	103	242	191
Δf_{noise} (Hz)	7.2	7.2	2.1	2.1
LOD (g)	5.08E-14	7.00E-14	8.67E-15	1.09E-14

www.manaraa.com

CHAPTER 6 CONCLUSION AND FUTURE WORK

MEMS electrostatic and piezoelectric mass sensors are on the brink of a mass sensing technology renaissance. As demonstrated in this dissertation, the resonators' outstanding sensitivity is attributed to their unrivaled frequency and electrical responses that can be tailored for any mass sensing applications. Also, they are fabricated using standard CMOS compatible microfabrication processes and their measured motional resistances could be designed within the 50-377 Ω range of RF front end devices. Therefore, direct integration with other existing CMOS devices is within reach using post-CMOS integration techniques. The unique attributes of these devices, as mentioned above, allows the use of technology in numerous of mass sensing applications in all fields of science and technology.

In addition, the economical aspect of this emerging technology is a key to keep further investigation. According to Yole, a market research, technology evaluation and strategy consulting company, "MEMS will continue to see steady, sustainable double digit growth for the next six years: 13 percent CAGR in revenues and 20 per cent CAGR in units. MEMS will grow to $21 billion market by 2017 [62]." It is very possible for devices such as the ones investigated in this dissertation to be part of a $21 billion dollar growing industry.

6.1 Contributions of this Work

This dissertation has covered all the design, simulation, micro-fabrication, testing, and implementation aspects of RF MEMS resonators as mass sensors. The devices developed through this work have the potential to function as front-end and/or back-end detectors for diagnostic/analytical systems. In addition, the microfabrication implemented to create

www.manaraa.com

electrostatically and piezoelectrically actuated devices by following standard CMOS foundry processes. This unique attributes allows the freedom to design resonators with a large variety of sizes and shapes which are very important parameters to determine the sensitivity of the devices. Also, size and shape variation allows a good control of the device motional impedance needed to directly integrate them to high-level systems using post-CMOS integration techniques.

The fabrication of electrostatically actuated devices using novel techniques to reduce the motional resistance is implemented, as described in chapter 3. Capacitively-transduced resonators use electrostatic actuation via capacitive air-gaps to achieve targeted resonance. The size of those gaps determine the motional resistance of the device. Standard contact photolithography techniques have resolution limitations which only allows a minimum feature of 1 μm. Therefore, to reduce the impedance of the device, capacitive gap reduction techniques need to be implemented. In order to do that, two novel techniques were implemented: air-gap reduction via oxidation and thin sacrificial layer air-gap reduction fabrication processes. Air-gap reduction via oxidation yield an air-gap size of ~300 nm on a deposited hard mask. In order to transfer that pattern to the resonator, a customized DRIE technique was developed and used. Thin sacrificial layer air-gap reduction fabrication processes yield air-gap sizes ranging from 250 nm down to 100 nm.

In chapter 4, piezoelectrically actuated devices using novel fabrication techniques that allows the integration of low-loss coupling substrates with and without SOI wafer technology is covered. Thin-film piezoelectric resonators use piezoelectric actuation via coupled electrodes to achieve the designed resonance. The size and number of electrodes needed to match the desired resonant mode shape determines the motional resistance of the device. To maximize the electrical and resonant frequency parameters of these resonators, a low-loss single crystalline Si and polysilicon layers are implemented. The Si coupling layer implementation is performed using a

www.manaraa.com

high yield Si DRIE TSV release technique while the polysilicon layer is done through an oxide pre-releasing technique. Both release techniques are high yield and CMOS compatible. The ZnO-on-Si resonators demonstrated loaded Q factors and resonant frequencies as high as 7,086 and 776.54 MHz, and motional resistance values as low as 169Ω in air. These values were achieved through an implementation of novel electrode design. Poly-SOI were implemented as a cheaper alternative to traditional SOI technology. The Poly-SOI wafers were fabricated in-house and the devices demonstrated loaded Q factors as high as ~3,000 and R_m values as low as 6 kΩ with an equivalent acoustic velocity of 6,912 ms^{-1} for a 7 µm thick layer. For this devices, the temperature coefficient of frequency of -3.77 ppm/°C was also measured which is the lowest among uncompensated TPOS resonators. This is the first time polysilicon has been implemented as a structural layer for TPoS resonators and the results are very promising despite that the polysilicon layer used was not fully optimized. Finally, TPoSCRE, a novel release technique developed in this work to fabricate ZnO-on-Si without the need of expensive SOI technology was implemented. A 4 kΩ resistive Si substrate was used to fabricate the resonators. Devices demonstrated loaded Q factor as high as ~1,000 and motional resistance values as low as 9 kΩ.

In addition to the innovation in design and microfabrication, the sensitivity of ZnO-on-Si was investigated in chapter 5. This is done to explore the possibilities for TPoS resonant technology to be used for mass sensing applications. In order to study the sensitivity of the device, both theoretical prediction and measurement methods were taken into account. In this work, to test the sensitivity of a 4th contour mode disk resonator, multiple PT micro-pellet depositions using a FIB system were made on chosen locations. We demonstrated that the sensitivity of the device for added masses at the maximal and minimal displacement points was of 1.17 Hz fg^{-1} and 0.334 Hz fg^{-1}, respectively. Also, the estimated LOD of the resonator was demonstrated to be 367 ag. This

www.manaraa.com

is the first time the sensitivity for ZnO-on-Si resonators of this kind has been reported. The LOD represents the second lowest measured value up to date from contour mode resonator technology as shown in Table 1.2. Also, a N5 lateral-extensional mode resonator was used to measure the weight of HKUST-1 MOF cluster of crystal measuring 5.5μm in diameter by 5 μm in height. The weight was found to be 24.75 pg and 31.19 pg for N5 mode and N9 mode frequency responses accordingly. This opens the possibilities of creating an ultrasensitive functionalized sensor with MOF crystals as the highly-selective recognition element.

6.2 Future Work

The demonstrated ultrasensitive ZnO-on-substrate resonators have almost endless number of applications in the fields of science and technology. Combining both MOF crystal and ZnO-on-substrate technology, as demonstrated in this dissertation, opens the possibilities for creating the most sensitive gas sensor ever reported. A few steps towards the development of this state-of-the art sensors already have been taken as shown in sections 6.2.1 and 6.2.2.

6.2.1 Ultra-Sensitive Gas Sensor Concept

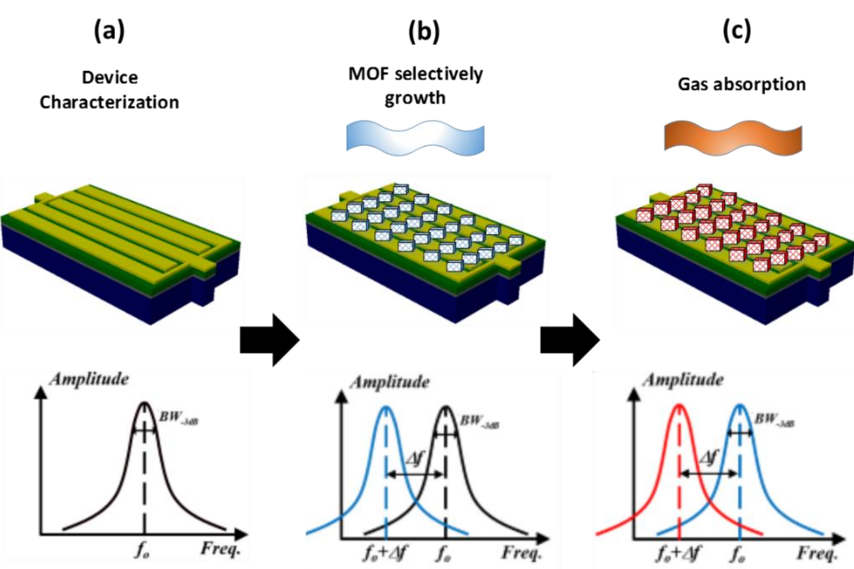

Figure 6.1 Illustration of ultra-sensitive gas sensor concept: (a) ZnO-on-Si device characterization, (b) selective MOF crystal growth on top electrodes and (c) gas absorption test.

www.manaraa.com

Figure 6.1 illustrates the steps needed to successfully fabricate an ultrasensitive gas sensor by integrating MOF crystals with ZnO-on-Si technology. It can also be observed that steps illustrated in Figure 6.1(a) and (b) have already been demonstrated in this dissertation. The only step left to be done is to test the devices in a custom-build gas testing chamber to extrapolate the sensitivity of the sensor based on the absorption characteristics of MOF layers towards different gasses.

6.2.2 Ultra-Sensitive Gas Sensor Test-set up Concept

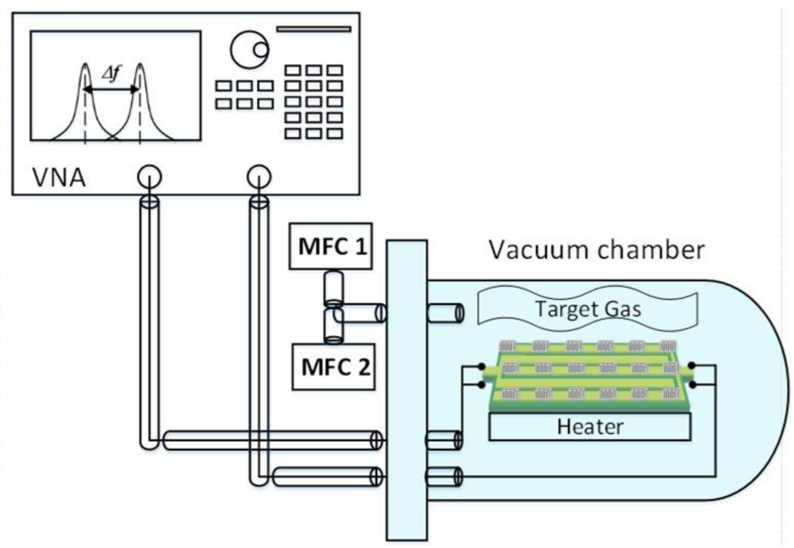

Figure 6.2 Illustration of ultra-sensitive gas sensor concept and test-set up.

After the MOF crystals have been properly grown on top of the electrodes of the ZnO-on-Si resonator, the gas sensitivity can be extracted using the test set-up illustrated in Figure 6.2. The two mass flow controllers (MCF 1 and MFC 2) need to have a gas ratio that allows a ppm-ppb target gas environment in order to test the limit of gas detection (LOGD) of the sensors. To remove the gas molecules form the MOF layer sensor regeneration, both vacuum and heat can be applied [63]. This is a great quality of MOFs because that allows the reuse of this sensors (illustrated in Figure 6.2). By taking advantage of these two ousting technologies, a one-of the-kind ultrasensitive gas sensors can be developed with endless future applications.

المنارة للاستشارات
www.manaraa.com

REFERENCES

[1] L. C. J. Qlark, "Monitor and Control of Blood and Tissue Oxygen Tensions," *ASAIO Journal,* vol. 2, pp. 41-48, 1956.

[2] L. C. Clark and C. Lyons, "ELECTRODE SYSTEMS FOR CONTINUOUS MONITORING IN CARDIOVASCULAR SURGERY," *Annals of the New York Academy of Sciences,* vol. 102, pp. 29-45, 1962.

[3] N. V. Lavrik, M. J. Sepaniak, and P. G. Datskos, "Cantilever transducers as a platform for chemical and biological sensors," *Review of Scientific Instruments,* vol. 75, pp. 2229-2253, 2004.

[4] J. Lee, W. Shen, K. Payer, T. P. Burg, and S. R. Manalis, "Toward Attogram Mass Measurements in Solution with Suspended Nanochannel Resonators," *Nano Letters,* vol. 10, pp. 2537-2542, 2010/07/14 2010.

[5] O. Brand, *Advanced Micro and Nanosystems* vol. 2: WILEY-VCH Verlag GmbH & Co. KGaA, Weinheim, 2005.

[6] K. Länge, B. Rapp, and M. Rapp, "Surface acoustic wave biosensors: a review," *Analytical and Bioanalytical Chemistry,* vol. 391, pp. 1509-1519, 2008/07/01 2008.

[7] G. Sauerbrey, "Verwendung von Schwingquarzen zur Wägung dünner Schichten und zur Mikrowägung," *Zeitschrift für Physik,* vol. 155, pp. 206-222, 1959/04/01 1959.

[8] "Recent Advances in Quartz Crystal Microbalance-Based Sensors," *Journal of Sensors,* vol. 2011, 2011.

[9] B. Drafts, "Acoustic wave technology sensors," *Microwave Theory and Techniques, IEEE Transactions on,* vol. 49, pp. 795-802, 2001.

[10] J. L. Arlett, E. B. Myers, and M. L. Roukes, "Comparative advantages of mechanical biosensors," *Nat Nano,* vol. 6, pp. 203-215, 04//print 2011.

[11] G. Wingqvist, "AlN-based sputter-deposited shear mode thin film bulk acoustic resonator (FBAR) for biosensor applications — A review," *Surface and Coatings Technology,* vol. 205, pp. 1279-1286, 11/25/ 2010.

www.manaraa.com

[12] H. C. Hao and D. J. Yao, "Highly sensitive and rapid detection of shigella flexneri in liquid sample by an immunomagnetic assay with shear horizontal surface acoustic wave sensors," in *Solid-State Sensors, Actuators and Microsystems (TRANSDUCERS & EUROSENSORS XXVII), 2013 Transducers & Eurosensors XXVII: The 17th International Conference on*, 2013, pp. 2114-2117.

[13] K. Länge, F. Gruhl, and M. Rapp, "Surface Acoustic Wave (SAW) Biosensors: Coupling of Sensing Layers and Measurement," in *Microfluidic Diagnostics*. vol. 949, G. Jenkins and C. D. Mansfield, Eds., ed: Humana Press, 2013, pp. 491-505.

[14] G. Binnig, C. F. Quate, and C. Gerber, "Atomic Force Microscope," *Physical Review Letters,* vol. 56, pp. 930-933, 03/03/ 1986.

[15] ChasteJ, EichlerA, MoserJ, CeballosG, RuraliR, and BachtoldA, "A nanomechanical mass sensor with yoctogram resolution," *Nat Nano,* vol. 7, pp. 301-304, 05//print 2012.

[16] J. Fritz, "Cantilever biosensors," *Analyst,* vol. 133, pp. 855-863, 2008.

[17] G. Blanco-Gomez and V. Agache, "Experimental Study of Energy Dissipation in High Quality Factor Hollow Square Plate MEMS Resonators for Liquid Mass Sensing," *Microelectromechanical Systems, Journal of,* vol. 21, pp. 224-234, 2012.

[18] J. E. Y. Lee, B. Bahreyni, Y. Zhu, and A. A. Seshia, "Ultrasensitive mass balance based on a bulk acoustic mode single-crystal silicon resonator," *Applied Physics Letters,* vol. 91, pp. 234103-234103-3, 2007.

[19] W. Jing, R. Zeying, and C. T. C. Nguyen, "1.156-GHz self-aligned vibrating micromechanical disk resonator," *Ultrasonics, Ferroelectrics and Frequency Control, IEEE Transactions on,* vol. 51, pp. 1607-1628, 2004.

[20] V. Agache, M. Cochet, R. Blanc, F. Baleras, and P. Caillat, "High Q factor plate resonators for ultrasensitive mass sensing applications," in *Solid-State Sensors, Actuators and Microsystems Conference, 2009. TRANSDUCERS 2009. International*, 2009, pp. 1630-1633.

[21] G. Blanco-Gomez, E. Trioux, and V. Agache, "Hollow Square- and Ring-Plate MEMS Oscillators Embedded in a Phase-Locked Loop for Low Limit of Detection in Liquid," *Electron Device Letters, IEEE,* vol. 33, pp. 609-611, 2012.

[22] R. Abdolvand, H. M. Lavasani, G. K. Ho, and F. Ayazi, "Thin-film piezoelectric-on-silicon resonators for high-frequency reference oscillator applications," *Ultrasonics, Ferroelectrics, and Frequency Control, IEEE Transactions on,* vol. 55, pp. 2596-2606, 2008.

www.manaraa.com

[23] K. Ping, S. Doerner, T. Schneider, D. Allara, P. Hauptmann, and S. Tadigadapa, "A Micromachined Quartz Resonator Array for Biosensing Applications," *Microelectromechanical Systems, Journal of,* vol. 18, pp. 522-530, 2009.

[24] V. M. Mecea, "Is quartz crystal microbalance really a mass sensor?," *Sensors and Actuators A: Physical,* vol. 128, pp. 270-277, 4/19/ 2006.

[25] H. Campanella, J. Esteve, J. Montserrat, A. Uranga, G. Abadal, N. Barniol*, et al.*, "Localized and distributed mass detectors with high sensitivity based on thin-film bulk acoustic resonators," *Applied Physics Letters,* vol. 89, pp. 033507-033507-3, 2006.

[26] W. D. Bowers, R. L. Chuan, and T. M. Duong, "A 200 MHz surface acoustic wave resonator mass microbalance," *Review of Scientific Instruments,* vol. 62, pp. 1624-1629, 1991.

[27] Z. Chen and F. Zhao, "Single crystalline 4H-polytype silicon carbide microresonator sensor for mass detection," *Materials Letters,* vol. 128, pp. 64-67, 8/1/ 2014.

[28] C. Zuniga, M. Rinaldi, S. M. Khamis, A. T. Johnson, and G. Piazza, "Nanoenabled microelectromechanical sensor for volatile organic chemical detection," *Applied Physics Letters,* vol. 94, pp. -, 2009.

[29] A. Cagliani and Z. J. Davis, "Ultrasensitive bulk disk microresonator-based sensor for distributed mass sensing," *Journal of Micromechanics and Microengineering,* vol. 21, p. 045016, 2011.

[30] J. H. Hales, J. Teva, A. Boisen, and Z. J. Davis, "Longitudinal bulk a coustic mass sensor," in *Solid-State Sensors, Actuators and Microsystems Conference, 2009. TRANSDUCERS 2009. International*, 2009, pp. 311-314.

[31] J. Tichý, *Fundamentals of Piezoelectric Sensorics: Mechanical, Dielectric, and Thermodynamical Properties of Piezoelectric Materials*. Verlag Berlin Heidelberg: Springer, 2010.

[32] L. Piezoelectric Ceramics from APC International, *Piezoelectric Ceramics: Principles and Applications*, 2011.

[33] M.-A. Dubois and P. Muralt, "Properties of aluminum nitride thin films for piezoelectric transducers and microwave filter applications," *Applied Physics Letters,* vol. 74, pp. 3032-3034, 1999.

[34] S. Humad, R. Abdolvand, G. K. Ho, G. Piazza, and F. Ayazi, "High frequency micromechanical piezo-on-silicon block resonators," in *Electron Devices Meeting, 2003. IEDM'03 Technical Digest. IEEE International*, 2003, pp. 39.3. 1-39.3. 4.

www.manaraa.com

[35] U. o. Cambridge. *Derivation of the rule of mixtures and inverse rule of mixtures*. Available: http://www.doitpoms.ac.uk/tlplib/bones/derivation_mixture_rules.php.

[36] K. M. Lakin and J. S. Wang, "UHF Composite Bulk Wave Resonators," in *1980 Ultrasonics Symposium*, 1980, pp. 834-837.

[37] H. J. McSkimin, "Chapter VII: Theoretical Analysis of Modes of Vibration for Isotropic Rectangular Plates Having All Surfaces Free," *Bell System Technical Journal,* vol. 23, pp. 151-177, 1944.

[38] R. A. Johnson, *Mechanical filters in electronics*, 1983.

[39] H. Zhili, S. Pourkamali, and F. Ayazi, "VHF single-crystal silicon elliptic bulk-mode capacitive disk resonators-part I: design and modeling," *Microelectromechanical Systems, Journal of,* vol. 13, pp. 1043-1053, 2004.

[40] M. Onoe, "Contour Vibrations of Isotropic Circular Plates," *The Journal of the Acoustical Society of America,* vol. 28, pp. 1158-1162, 1956.

[41] J. Wang, "Self-aligned radial contour mode micromechanical disk resonators for wireless communications," Ph.D, University of Michigan, 2006.

[42] J. E. Y. Lee and A. A. Seshia, "5.4-MHz single-crystal silicon wine glass mode disk resonator with quality factor of 2 million," *Sensors and Actuators A: Physical,* vol. 156, pp. 28-35, 11// 2009.

[43] J. R. Clark, H. Wan-Thai, M. A. Abdelmoneum, and C. T. C. Nguyen, "High-Q UHF micromechanical radial-contour mode disk resonators," *Microelectromechanical Systems, Journal of,* vol. 14, pp. 1298-1310, 2005.

[44] J. Wang, J. E. Butler, T. Feygelson, and C. T. C. Nguyen, "1.51-GHz nanocrystalline diamond micromechanical disk resonator with material-mismatched isolating support," in *Micro Electro Mechanical Systems, 2004. 17th IEEE International Conference on. (MEMS)*, 2004, pp. 641-644.

[45] D. R. Sherman, *An investigation of MEMS anchor design for optimal stiffness and damping*, 1996.

[46] M. J. de Boer, J. G. E. Gardeniers, H. V. Jansen, E. Smulders, M. J. Gilde, G. Roelofs, *et al.*, "Guidelines for etching silicon MEMS structures using fluorine high-density plasmas at cryogenic temperatures," *Microelectromechanical Systems, Journal of,* vol. 11, pp. 385-401, 2002.

[47] C. H. Mastrangelo and C. H. Hsu, "Mechanical stability and adhesion of microstructures under capillary forces. I. Basic theory," *Microelectromechanical Systems, Journal of,* vol. 2, pp. 33-43, 1993.

www.manaraa.com

[48] G. Piazza, P. J. Stephanou, and A. P. Pisano, "One and two port piezoelectric higher order contour-mode MEMS resonators for mechanical signal processing," *Solid-State Electronics,* vol. 51, pp. 1596-1608, 11// 2007.

[49] J. Molarius, J. Kaitila, T. Pensala, and M. Ylilammi, "Piezoelectric ZnO films by r.f. sputtering," *Journal of Materials Science: Materials in Electronics,* vol. 14, pp. 431-435, 2003/05/01 2003.

[50] C. Kuo-Shen, A. A. Ayon, X. Zhang, and S. M. Spearing, "Effect of process parameters on the surface morphology and mechanical performance of silicon structures after deep reactive ion etching (DRIE)," *Microelectromechanical Systems, Journal of,* vol. 11, pp. 264-275, 2002.

[51] J. Audet. (2012). *Q Factor Measurements on L-C Circuits*. Available: http://hb9abx.no-ip.biz/VE2AZX-Q-factor.pdf

[52] R. Abdolvand, "THIN-FILM PIEZOELECTRIC-ON-SUBSTRATE RESONATORS AND NARROWBAND FILTERS," PhD, Electrical and Computer Engineering, Georgia Institute of Technology, 2008.

[53] O. Tigli and M. E. Zaghloul, "A Novel Saw Device in CMOS: Design, Modeling, and Fabrication," *Sensors Journal, IEEE,* vol. 7, pp. 219-227, 2007.

[54] C. K. Campbell and C. B. Saw, "Analysis and Design of Low-Loss SAW Filters Using Single-Phase Unidirectional Transducers," *Ultrasonics, Ferroelectrics, and Frequency Control, IEEE Transactions on,* vol. 34, pp. 357-367, 1987.

[55] J. Rickert, T. Weiss, W. Kraas, G. Jung, and W. Göpel, "A new affinity biosensor: self-assembled thiols as selective monolayer coatings of quartz crystal microbalances," *Biosensors and Bioelectronics,* vol. 11, pp. 591-598, // 1996.

[56] E. Lee and S. Rha, "A study of the morphology and microstructure of LPCVD polysilicon," *Journal of Materials Science,* vol. 28, pp. 6279-6284, 1993/12/01 1993.

[57] P. Wanling and F. Ayazi, "Thin-film piezoelectric-on-substrate resonators with Q enhancement and TCF reduction," in *Micro Electro Mechanical Systems (MEMS), 2010 IEEE 23rd International Conference on*, 2010, pp. 727-730.

[58] K. A. Shaw, Z. L. Zhang, and N. C. MacDonald, "SCREAM I: A single mask, single-factorcrystal silicon, reactive ion etching process for microelectromechanical structures," *Sensors and Actuators A: Physical,* vol. 40, pp. 63-70, 1// 1994.

[59] R. M. Langford, T. X. Wang, and D. Ozkaya, "Reducing the resistivity of electron and ion beam assisted deposited Pt," *Microelectronic Engineering,* vol. 84, pp. 784-788, 5// 2007.

www.manaraa.com

[60] L. E. Kreno, K. Leong, O. K. Farha, M. Allendorf, R. P. Van Duyne, and J. T. Hupp, "Metal–organic framework materials as chemical sensors," *Chemical reviews,* vol. 112, pp. 1105-1125, 2011.

[61] N. Stock and S. Biswas, "Synthesis of metal-organic frameworks (MOFs): routes to various MOF topologies, morphologies, and composites," *Chemical reviews,* vol. 112, pp. 933-969, 2011.

[62] YOLE, "Yole Développement releases 2012 MEMS industry report," MEMS market forecast 2011-2017 in value2012.

[63] D. Farrusseng, *Metal-organic frameworks: applications from catalysis to gas storage*: John Wiley & Sons, 2011.

www.manaraa.com

APPENDIX A

A.1 Key Fabrication Process Steps

1) Wafer labeling

2) Wafer cleaning
   1.1) RCA cleaning
      RCA 1: 5 H_2O:NH_4OH:H_2O_2 @ 60°C
      RCA 2: 5 H_2O: HCL:H_2O_2 @ 60°C
   1.2) Solvent clean
      Acetone, Methanol, and DI water

3) Photolithography
   1.1) AZ1512
      Dehydration bake for 5min @ 110°C
      Spin HDMS for 30 sec @ 3000 RPM
      Spin photoresist for 30 sec @ 3000 RPM
      Softbake for 1 min @ 110°C
      UV expose for 3.5 sec @ 22mW/cm^2
      Develop for 30 secs in AZ 726 @ 25°C
   1.2) AZ12XT
      Dehydration bake for 5min @ 110°C
      Spin HDMS for 30 sec @ 3000 RPM
      Spin photoresist for 40 sec @ 3500 RPM
      Softbake for 5 min @ 110°C
      UV expose for 15 sec @ 22mW/cm2
      Postbake for 2 min@ 90°C
      Develop for 60 secs in AZ 300 @ 25°C

4) Deep reactive ion etch (DRIE)
   1.1) High aspect ratio standard silicon (HAR Si)
      300 sccm SF_6 for 3sec, 200 sccm C_4H_8 for 1.4sec/20 sccm O_2 1.4sec @2400W
      -15°C substrate holder temperature
      10µm/min Si etch rate
   1.2) Modified high aspect ratio standard silicon (M-HAR Si)
      300 sccm SF6 for 2sec, 200 sccm C4H8 /20 sccm O2 for 1.4sec @2400W
      -20°C substrate holder temperature
      8µm/min Si etch rate

www.manaraa.com

1.3) Standard silicon dioxide (SiO_2) @2800W
13 sccm CH_4 /17 sccm C_4H_8 /150 sccm He
-20°C substrate holder temperature
200nm/min Si etch rate

1.4) ZnO@1800W
32 sccm CH_4/16 sccm
-20°C substrate holder temperature
~0.5µm/min ZnO etch rate

5) Etchback
Spin HDMS for 30 sec @ 3000 RPM
Spin AZ12XT for 30 sec @ 1000 RPM and repeat until the devices are planar
DRIE O_2 at 2500W until the top of devices is visible

6) Oxygen descum
Equipment: PT700 by Plasma Therm, Inc.
75 watts of RF power
50 sccm of O_2 @ 300mTorr

7) Wet etch

1.1) 6:1 buffer oxide etch (6:1 BOE)
2nm/sec thermal oxide etch rate @ 25°C
49% Hydrofluoric Acid (HF)
~10µm/min thermal oxide etch rate @ 25°C

1.2) ZnO
100 HCL: H2O
10 nm/sec etch rate @ 25°C

1.3) Au/Cr
Gold Etchant TFA solution
Chrome Etchant by Aldrich
168 nm/min Au etch rate @ 25°C
240 nm/min Cr etch rate @ 25°C

8) Gold electroplating
Sulfite Gold Plating Solution TSG-250
60°C Deposition temperature
20mA/cm2 of applied current density
0.5µm/min deposition rate

9) Thin-film deposition

1.1) ZnO
Equipment: AJA 300 Sputter system
100 watts of RF power
6 sccm O_2: 6 sccm Ar
5 mTorr deposition pressure

www.manaraa.com

2.2µm/hr deposition rate
300°C substrate deposition temperature
Annealing treatment for 1 hr at 400°C

1.2) Platinum/ Chrome (Pt/Cr)
Equipment: AJA 300 Sputter system
100 watts of DC power
Ar 12 sccm
5 mTorr deposition pressure
600nm/hr deposition rate for Pt
300nm/hr deposition rate for Cr

1.3) Gold/Chrome (Au/Cr)
Equipment AJA ebeam evaporator using 8kV and 2mA beam current
5 µTorr deposition pressure
400 nm/hr deposition rate for Au
1µm/Hr deposition rate for Cr

1.4) ALD Al_2O_3
Equipment: Savannah 100 by Cambridge NanoTech Inc.
250°C substrate temperature
Flow rate: 20 sccm
Recipe: pulse H_2O, 0.015 sec
wait 20 sec
pulse TMA, 0.1 sec
wait 20 sec
0.9 Å/cycle deposition rate

www.manaraa.com

ABOUT THE AUTHOR

Ivan Fernando Rivera received dual M.S. degrees in Electrical and Biomedical/ Chemical Engineering in May 2012 from the University of South Florida where he is currently working towards a Ph.D. degree in Electrical Engineering under the supervision of Dr. Jing Wang. He is part of the RF MEMS Transducers Group (a division of the WAMI Center), Electrical Engineering Department, and University of South Florida. His areas of research are RF and MEMS devices. His dissertation work focuses mainly on the fabrication and characterization of RF MEMS resonators for mass sensing applications.

www.manaraa.com